AN ABSTRACT OF THE THESIS OF

Timothy L. Weber for the degree of Doctor of Philosophy in Mechanical Engineering presented on April 26,1991.

Title: Turbulence Induced Loads on a Teetered Rotor

Redacted for privacy

Abstract approved: _____

Robert E. Wilson

Development of variable speed horizontal axis wind turbines has resulted in a need for an analysis code with a rotor speed degree-of-freedom. This study develops a five degree-of-freedom time domain computer code that evaluates blade and rotor, mean and cyclic loads with nonlinear aerodynamics together with atmospheric turbulence as a forcing function.

Verification of the model is made by comparison of loads predictions between ESI-80 wind turbine data and analytical solutions. Results show good agreement for mean and cyclic loads and teeter angle excursions.

A single-blade point turbulence simulation model is optimized using a three-blade point turbulence simulation model. The optimum point is the 80% radius location, although a multiplying factor is needed to make conservative fatigue cycle predictions of blade bending.

ESI-80 start-up and shutdown scenarios are examined, prediction trends matched ESI-80 data. Three generator

models are investigated. Results show that generator torque cycles are reduced and yearly energy capture increased by 24% when a variable speed generator is implemented.

Turbulence Induced Loads on a Teetered Rotor

by

Timothy L. Weber

A THESIS

submitted to

Oregon State University

in partial fulfillment of
the requirements for the
degree of

Doctor of Philosophy

Completed April 26, 1991

Commencement June 1991

APPROVED

Redacted for privacy

Professor of Mechanical Engineering
in charge of major

Redacted for privacy

Head of Department Mechanical Engineering

Redacted for privacy

Dean of Graduate School

Date thesis presented: April 26, 1991

Typed by Timothy L. Weber for Timothy L. Weber

TABLE OF CONTENTS

LIST OF FIGURES

LIST OF TABLES

APPENDIX LIST OF FIGURES

APPENDIX LIST OF TABLES

NOMENCLATURE

SYMBOL	DEFINITION
a	axial induction factor, decay coefficient
A	rotor area
A_1, A_2, A_3	equal areas
a_i	acceleration magnitude in ith direction
a_c	axial induction constant
$\mathbf{a}_i$	tilt and generator coordinates
$\mathbf{a}_i'$	yaw coordinates
$\mathbf{a}_i''$	inertial coordinates
${}^N\mathbf{a}^Q$	acceleration of point Q in reference frame N
b	constant
B	number of blades
$\mathbf{b}_i$	rotating rotor coordinates
c	chord length, Weibell constant
c_e	constant
c_D	drag coefficient
c_L	lift coefficient
c_P	power coefficient
c_T	thrust coefficient
c_{TOR}	drive train torsional damper
$\mathbf{c}_i$	rotating teeter coordinates
d	distance from tower centerline to teeter point
D	drag
$\mathbf{d}_i$	delta-3 coordinates
EI	blade stiffness

$\mathbf{e}_i$	precone coordinates
f	generator fixed loss factor
f_n, f_t	aerodynamic forces
F_r, F_r^*	generalized active and inertia forces
F_{rHUB}, F_{rHUB}^*	generalized active and inertia hub forces
$\mathbf{f}_i$	elastic axis rotation coordinates
g	gravity
g_r	generalized inertia term
$\mathbf{g}_i$	deflected blade coordinates
H_{HUB}	hub height
$I_{generator}$	generator inertia
I_{HUB}	hub inertia
$\mathbf{I}$	inertia dyadic
k	constant
k_{TOR}	drive train torsional spring
L	lift
M	number of turbulence time series values
M_{HUB}	hub mass
n	wind shear exponent
N	gearbox step up ratio, generator reference frame, number of turbulence grid points
N_{ri}	partial velocity magnitude in ith direction
P_{ij}	magnitude of distance on ith blade in jth direction
P_{rated}	generator rated power
${}^N\mathbf{p}^Q_i$	position vector on ith blade of point

	Q in reference frame N
q_1	blade one deflection
q_2	blade two deflection
q_3	teeter angle
q_4	rotor angle
q_5	generator angle
q_{static}	static tip deflection
Q	point on blade
Q^{ij}	transformation from ith generator coordinate to jth blade coordinate
r	distance to blade element
R	total blade length
R_1, R_2, R_3	three-point turbulence simulation points
R_i	resultant force magnitude in ith direction
R_H	hub length
R_u	undersling length
R	resultant of external forces
S_{ij}	csd between points i and j
S_{ii}	psd at point i
T	rotor torque
$T_{electrical}$	generator electrical restraining torque
T_{fixed}	generator fixed loss
T_{losses}	generator torque losses
$T_{variable}$	generator variable loss
T	resultant of external torques
u	axial velocity component

u_1	wake velocity
u_{ij}	jth blade displacement in ith direction
u_r	generalized speed
V	blade element potential energy, mean wind speed
V_{HUB}	hub velocity
V_i	velocity magnitude in ith direction
V_∞	free stream velocity
$^N\mathbf{V}^Q$	velocity of point Q in reference frame N
$\mathbf{V}_{Qr}$	holonomic partial velocity
w	frequency, weighing factor
W	relative air velocity, Weibell wind speed
w_i	angular velocity magnitude in ith direction
w_n	natural frequency
W_p	Weibell wind speed
$^N\mathbf{w}^Q$	angular velocity of point Q in reference N
y	distance from tower centerline
z	dimensionless blade radius

Greek

α	angle of attack
α_i	angular acceleration magnitude in ith direction
$^N\boldsymbol{\alpha}^Q$	angular acceleration of point Q in reference frame N
β	precone angle

γ_{ij}	coherence function between points i and j
Γ	tip speed ratio
ΔP	pressure difference across the rotor
Δr	distance between points
δ_3	delta-3 angle
ϵ	tower shadow velocity deficit
ζ	blade element rotation
η_{GB}	gearbox efficiency
η_{Gen}	generator efficiency
θ	blade twist
θ_p	elastic axis angle
λ	optimum tip speed ratio
μ	blade mass per unit length
ρ	air density
ϕ_i	assumed mode shape in ith direction
ϕ_a	mode shape for uniform loading
ϕ_b	mode shape for tip force
ϕ_α	induction angle
χ	tilt angle
ω^q_r	holonomic partial angular velocity
Ω	rotor angular velocity
Ω_0	rated rotor angular velocity
Ω_R	nominal rotor angular velocity

Mathematical

∂	partial
$(\dot{})$	time derivative
$\mathcal{F}^{-1}$	inverse Fourier transform
$P(W \geq W_p)$	probability that W is greater then W_p

Turbulence Induced Loads on a Teetered Rotor

CHAPTER 1

Introduction

The determination of inertial and aerodynamic loads is necessary for the design of horizontal axis wind turbines (HAWT). Extensive work has been done predicting steady-state and cyclic blade and rotor loads [1-6] for constant speed HAWT. Currently, variable speed generators are being examined for use with HAWT [7]. The effect of variable speed operation on blade and rotor loads is not well known. Understanding variable speed operation of HAWTS is critical because the rotor speed can coincide with many system natural frequencies. Instabilities and excitations near system natural frequencies can reduce working lifetimes of components and, in extreme cases, cause catastrophic failure. The wind turbine designer needs tools to predict potential trouble spots. This thesis develops techniques for analyzing the loads associated with variable speed operation of HAWT.

The objective of this thesis was to develop a five degree-of-freedom time-domain computer model of a two-bladed, teetered HAWT with a variable speed rotor. The specific geometry was chosen to parallel projected development of HAWT which will have this configuration [8]. The computer code determines loads and response by

combining a mathematical model having four degrees-of-freedom with aerodynamic loading. The aerodynamic loading consists of deterministic effects, such as wind shear, tower shadow, and yaw, with stochastic effects from wind turbulence.

1.1 Variable Speed

In order for variable speed to be economically viable, the additional cost of variable speed equipment must be offset. These offsets are a combination of increased power capture from the wind and decreased loads, which results in longer turbine component lifetimes. In the past, this has not been the case, consequently most HAWT run at fixed speed. Recently, the capital cost of the power transmission components used in variable speed generators has decreased [7]. With this decrease, variable speed implementation has become a candidate for use on the next generation of wind turbines. The advantages of variable speed operation are numerous and have been extensively discussed, although their individual reduction of the cost of energy is widely varied and often cannot be assigned a dollar value.

A typical HAWT rotor power coefficient (Cp) versus tip speed ratio Γ is shown in Figure 1.1. A fixed speed wind turbine can be designed to have an optimum power coefficient at only one wind speed. When the wind speed is

either higher or lower than this optimum wind speed, the aerodynamic efficiency is reduced. A variable speed turbine can operate with a optimum power coefficient by varying the rotor speed proportionally to the wind speed. This results in increased power capture over fixed speed operation. Predictions of increased power have been widely varied, from 3% to 6% [9] up to 10% to 20% [10].

A variable speed machine can reduce the power and load fluctuations caused by rapid changes in the wind. When a fixed speed machine experiences a gust, the effects are translated directly to the machine as a change in torque and consequently changes the power sent to the utility [11]. This has a disadvantage for wind farms with large numbers of turbines, subject to wind gusts, could send large, potentially damaging voltage spikes through the utility distribution system. The direct variation of torque with wind tends to decrease the fatigue life of the drive train components. Variable speed machines can use the rotor as a flywheel storage system to reduce these effects. When a wind gust is experienced the rotor can accelerate, transferring the increase in wind energy to the rotor as kinetic energy instead of passing it down the drive train as a sudden increase in torque. During a wind deficit the opposite occurs. The generator extracts energy from the rotor, which will decelerate the rotor. This process also significantly dampens torque variations due to turbulence, tower shadow, and wind shear.

The variable speed configuration can be used as a turbine control system. Many fixed pitch machines use blade pitching to keep thrust and torque below some nominal value dictated by machine limitations. Instead, the rotor speed can be varied to achieve the same result without the complicated pitch actuators. Control schemes using both variable speed generators and mechanical blade pitching were developed for HAWT [12-13]. Blade pitching reduces torque variations while maintaining rated power.

Variable speed generators can be used to regulate start and stop conditions. Turbines can be motored to a start-up rotation speed and braking can be achieved by setting the generator electrical torque higher than the mechanical rotor torque. Braking ability would still be needed for emergency loss-of-load. Some fixed speed machines freewheel up to their normal operating speed and the generator is then turned on. This causes an impulse torque to be transmitted through the drive train increasing wear and fatigue. Fixed speed machines need a braking device to stop the turbine. Brakes are aerodynamic, such as blade feathering, or mechanical, such as friction brakes. Anderson et al [10] were able to use motored start up to 67% of rated rotor speed for a 500 horsepower variable speed demonstration. The start-up took approximately 100 seconds.

Variable speed generators can be used to dampen out torsional modes that exist in the drive train. This

phenomenon is often referred to as ringing. The quick response of generator torque allows damping of very high modes. A simulated 0.1 Hertz drive train resonance was successfully damped out on a 500 horsepower variable speed demonstration [10].

The problem of synchronizing wind turbine output power with the utility is eliminated with variable speed operation. This reduces the amount of time the generator is off-line during start up conditions. This can be significant when the wind is oscillating around the minimum operating speed.

Variable speed operation can also reduce acoustic noise. Noise reduction is important when the turbines are sited near residential areas. At high wind speeds the rotor is operating slower to limit torque. The slower rotor speed reduces the noise emitted by the blade.

The preceding paragraphs have outlined the many advantages of operating HAWT with variable speed generators. A number of variable speed test machines have been built to date.

The MOD-0A, a two-bladed HAWT, was equipped with a variable speed generator and tested in a number of configurations [14]. Drive train loads variations were reduced and the power quality was improved with the variable speed operation.

A three-bladed 40 kiloWatt HAWT was tested Sweden [15] with a constant tip speed ratio below rated torque and held

to the rated torque above. Significant torque variations were reduced with the variable speed generator.

Other test variable speed HAWT have been studied in Japan [16], Germany [17], and Italy [18]. At the German site, noise reduction was reported for the variable speed operation.

1.2 Blade Dynamics

The blades of a HAWT are long cantilever beams. The blades are frequently rigidly attached to the hub. The hub can either be rigidly attached to the low-speed shaft or allowed to teeter. Teeter mechanisms can include the displacement of the teeter axis from the blades principal bending axes, which is referred to as undersling, and the teeter axis may be rotated from a perpendicular alignment from the blades, referred to as a delta-3 angle. Each blade has three degrees-of-freedom: motion in the flapping direction, motion in the edgewise direction, and torsional motion. A teetered rotor would have seven degrees-of-freedom, three for each blade and one for the teeter motion. This geometry is similar to that of many helicopter rotors. One major difference is that helicopter blades are kept as light as possible to reduce power required for flight. Helicopter blades are also replaced frequently, as often as every 1000 hours of flight time, resulting in less required structural support to resist

fatigue. Consequently, most HAWT blades are much heavier and stiffer than helicopter blades. Most of the governing equations for blade motions are similar. The large difference in stiffness results in some of the terms governing HAWT blade motion to be small. The torsional stiffness can be more than an order of magnitude greater than the edgewise stiffness which in turn may be an order of magnitude greater than the flapwise stiffness. Often, degrees-of-freedom in these directions can be ignored. A thorough description of governing equations for blade motion can be found in Johnson [19], Bramwell [20], and Gessow & Meyers [21]. A discussion of current blade modeling techniques is made by Hodges [22]. Solutions to the blade equations can be found depending on their complexity. Aeroelastic solutions can be obtained by linearizing the dynamics and the aerodynamics. This technique is more suitable for helicopters, where the geometry lends itself to linearization. In the literature, a number of researchers have examined aeroelastic solutions for helicopter rotors [23-25]. Kottapalli and Friedman [26] examined the aeroelastic stability of a wind turbine blade by computing an equilibrium position for the nonlinear equations and then examining the behavior of perturbations about the equlibrium position. Linearized dynamics has been used to examine system natural frequencies and stability regions [27-28]. Including the nonlinearities in the dynamics and the aerodynamics requires a solution in

the time domain. Recently, Hartin [4] combined tower motion and elastic blade flapping with an unsteady aerodynamic model for a HAWT. The response was obtained by using a time domain predictor-corrector method.

1.3 Rotary Wing Aerodynamics

Aerodynamic loads on a HAWT rotor are determined using the axial momentum theory for an actuator disk first examined by Rankine [29] and Froude [30]. This theory balances the thrust from the momentum change of the flow passing through rotor with the blade element thrust. This theory is often referred to as strip theory as the flow through the rotor can be divided up into individual streamtubes or "strips." This theory was modified by Prandtl [31] and Goldstein [32] to account for tip-loss effects. A modified strip theory was developed by Wilson and Walker [33] to account for wake expansion. Using the assumption of linear aerodynamics, closed form solutions can be achieved. Most HAWT operate with large portions of their blades in deep stall, so use of linear aerodynamics is not generally a valid assumption. When nonlinear aerodynamics is used a solution can be found through an iterative procedure. The inclusion of nonlinear aerodynamics has been shown to be an improvement [34].

A wind model to drive the aerodynamic model consists

of two distinct parts, a deterministic part and a stochastic part. The deterministic wind consists of effects that are constant for each rotor revolution. These are the mean wind, wind shear, tower interference, and yaw. The stochastic portion is due to atmospheric turbulence. Turbulence consists of lateral, vertical, and longitudinal components. Only the longitudinal component is important in HAWT load analysis. Many turbulence models have been developed using simple autoregression for a single point in space. Connell [35] developed a model that decomposes a Fourier Transform of a autocorrelation for a rotating point in turbulent wind which can be used for analysis of small HAWT with a rigid rotor. Veers [36] developed a full field model that has many applications in wind engineering but requires mainframe memory to run. Walker et al [37] summarized turbulence models for HAWT use. A number of analysists have implemented turbulence models into loads prediction codes [38-40].

1.4 References

1. Wilson, R.E., Walker, S.N., Weber, T.L., Hartin, J.R., "A Comparison of Mean Loads and Performance Predictions with Experimental Measurements for Horizontal Axis Wind Turbines," Eighth ASME Wind Energy Symposium, Houston, Texas, Jan. 22-29, 1989.

2. Wright, A.D., Buhl, M.L., Thresher, R.W., "FLAP Code Development and Validation," SERI/TR-217-3125, January 1988.

3. Hansen, A.C., Butterfield, C.P., Cui, X., "Yaw Loads and Motions of a Horizontal Axis Wind Turbine," European Wind Energy Conference (EWEC), Glasgow, Scotland, July 10-13, 1989.

4. Hartin, J.R., "Evaluation of Prediction Methodology for blade loads on a Horizontal Axis Wind Turbine," Ninth ASME Wind Energy Conference, New Orleans, Louisiana, January 14-18, 1990.

5. Morgan, C.A., Garrad, A.D., Hassan, U., "Measured and Predicted Wind Turbine Loading and Fatigue," EWEC, Glasgow, Scotland, July 10-13, 1989.

6. Derdelinckx, R., Hirsh, Ch., "Dynamic Load Calculations of Horizontal Axis Wind Turbines", EWEC, Glasgow, Scotland, July 10-13, 1989.

7. McNerny, G., "The Effect of Variable Speed Operation on the Cost Projections for Advanced Wind Turbines," Ninth ASME Wind Energy Symposium, New Orleans, Louisiana, January 14-18, 1990.

8. Hock, S.M., Thresher, R.W., Cohen, J.M., "Performance and Cost Projections for Advanced Wind Turbines," Ninth ASME Wind Energy Symposium, New Orleans, Louisiana, January 14-18, 1990.

9. Husse, G., Perpeintner, R., "The Effect of Variable Rotor Speed on the Design and Operation of a WEC," EWEC, Hamberg, West Germany, Oct. 22-26, 1984.

10. Anderson, T.S., Hughes, P.S., Klein, F.F., Mutone, G.A., "Double-fed Variable Speed Generating System Testing," Fourth ASME Wind Energy Symposium, Dallas, Texas, February 17-21, 1985.

11. Nordquist, P., "Investigation of Electrical Power Pulsations from a 2 megaWatt Wind Turbine Generator," EWEC, Glasgow, Scotland, July 10-13, 1989.

12. Ernst, J., "Control of a Variable Speed WEC with a Syncronous Generator and a DC Link Convertor," EWEC, Hamberg, West Germany, Oct. 22-26, 1984.

13. Bongers, P., Engelen, T., Dijkstra, Kock, Z., "Optimal Control of a Wind Turbine in Full Load," EWEC, Glasgow, Scotland, July 10-13, 1989.

14. Schmidt, W.C., Birchenough, A.G., "Evaluating Variable Speed Generating Systems on the DOE/NASA MOD-0A Wind Turbine," Wind Power, San Francisco, California, August 27-30, 1985.

15. Carlson, O., Tsiolis, S., and Johansson, G., "Variable Speed AC-Drive System with Pitch or Yaw Control," Wind Power, San Francisco, California, October 5-8, 1987.

16. Matsuzaka, T., Tsuchiya, K., Yamada, S., and Kitahara, H., "A Variable Speed Wind Generating System and Its Test Results," EWEC, Glasgow, Scotland, July 10-13, 1989.

17. Husse, G., Einmann, R., "Wind Power Plant WKA-60 for Helgaland - Status of the Project," EWEC, Glasgow, Scotland, July 10-13, 1989.

18. Coriante, D., Foli, U., Sesto, E., Taschini, A., Aviola, S., and Zappala, F., "GAMMA 60 1.5 MW WTG," EWEC, Glasgow, Scotland, July 10-13, 1989.

19. Johnson, W., Helicopter Theory, Princeton University Press, 1983.

20. Bramwell, A.R.S., Helicopter Dynamics, Edward Arnold Ltd., London, 1976.

21 Gessow, A., Meyers, G.C., Aerodynamics of the Helicopter, Fredrick Ungar Publishing Co., New York, 1952.

22. Hodges, D.H., "Review of Composite Rotor Blade Modeling," AIAA J. Vol. 28, No. 3, 1990.

23. Ormiston, R.A., Peters, D.A., "Hingeless Helicopter Rotor Response with Non-Uniform Inflow and Elastic Bending," J. Aircraft, Vol. 9, No. 10, 1972.

24. Miller, R.H., "Methods for Rotor Aerodynamic and Dynamic Analysis," Prog. Aero. Sci., Vol. 22, 1985.

25. Piziali, R.A., "Method for Solution of the Aeroelastic Response Problem for Rotating Wings," J. Sound Vib., Vol. 4, No. 3, 1966.

26. Kottapalli, S.B.R., Friedman, P.P., "Coupled Rotor/ Tower Aeroelastic Analysis of HAWT Blades," AIAA J., Vol. 18, No. 9, 1980.

27. Feitsom E.A.N., Meadm D.J., "Parametric Resonance in HAWTS," EWEC, Glasgow, Scotland, July 10-13, 1989.

28. Weyh, B., Ackva, J., "Parameter-Excited Instabilities of 1- and 2-Bladed HAWTS," EWEC, Glasgow, Scotland, July 10-13, 1989.

29. Rankine, W.J.M., Transactions, Institute of Naval Architects, Vol. 6, p. 13, 1865.

30. Froude, R.E., Transactions, Institute of Naval Architects, Vol. 30, p. 390, 1889.

31. Prandtl, L., "Appendix to Scraubenpropellor mit Gerngstein Energieverlust," by Betz, A., Guttinger Nachr, 1919.

32. Goldstein, S., "On the Vortex Theory of Screw Propellors," Proc. Royal Soc. A123, p. 440, 1929.

33. Wilson, R.E., Walker, S.N., "Performance Analysis of HAWTS," NASA-NAG-3-278, 1984.

34. Weber, T.L., "Inclusion of Nonlinear Aerodynamics in the FLAP Code," Ninth ASME Wind Energy Symposium, New Orleans, Louisiana, January 14-18, 1990.

35. Connell, J.R., "The Spectrum of Wind Speed Fluctuations Encountered by a Rotating Blade of a WEC," PNL 4083, Pacific Northwest Laboratories, Richland, Washington, 1981.

36. Veers, P.S., "Modeling Stochastic Wind Loads on a Vertical Axis Wind Turbine," SAND83-1909, Sandia National Laboratories, 1984.

37. Walker, S.N., Weber, T.L., Wilson, R.E., "A Comparison of Wind Turbulence Simulation Models for Stochastic Loads Analysis for HAWT," SERI/STR-217-3463, June 1989.

38. Wright, A.D., Weber, T.L., Thresher, R.W., Butterfield, C.P., "Prediction of Stochastic Blade for Three-Bladed, Rigid-Hub Rotors," Ninth ASME Wind Energy Symposium, New Orleans, Louisiana, January 14-18, 1990.

39. Powles, S.J.R., Anderson, M.B., "The Effect of Stochastic and Deterministic Loading on Fatigue Damage in Large HAWT," Sir Robert McAlpine & Sons, Ltd., London, U.K., 1984.

40. Garrad, A.P., Hassan, U., "The Dynamic Response of Wind Turbines for Fatigue Life and Extreme Load Prediction," EWEC, Rome, Italy, Oct. 7-9. 1986.

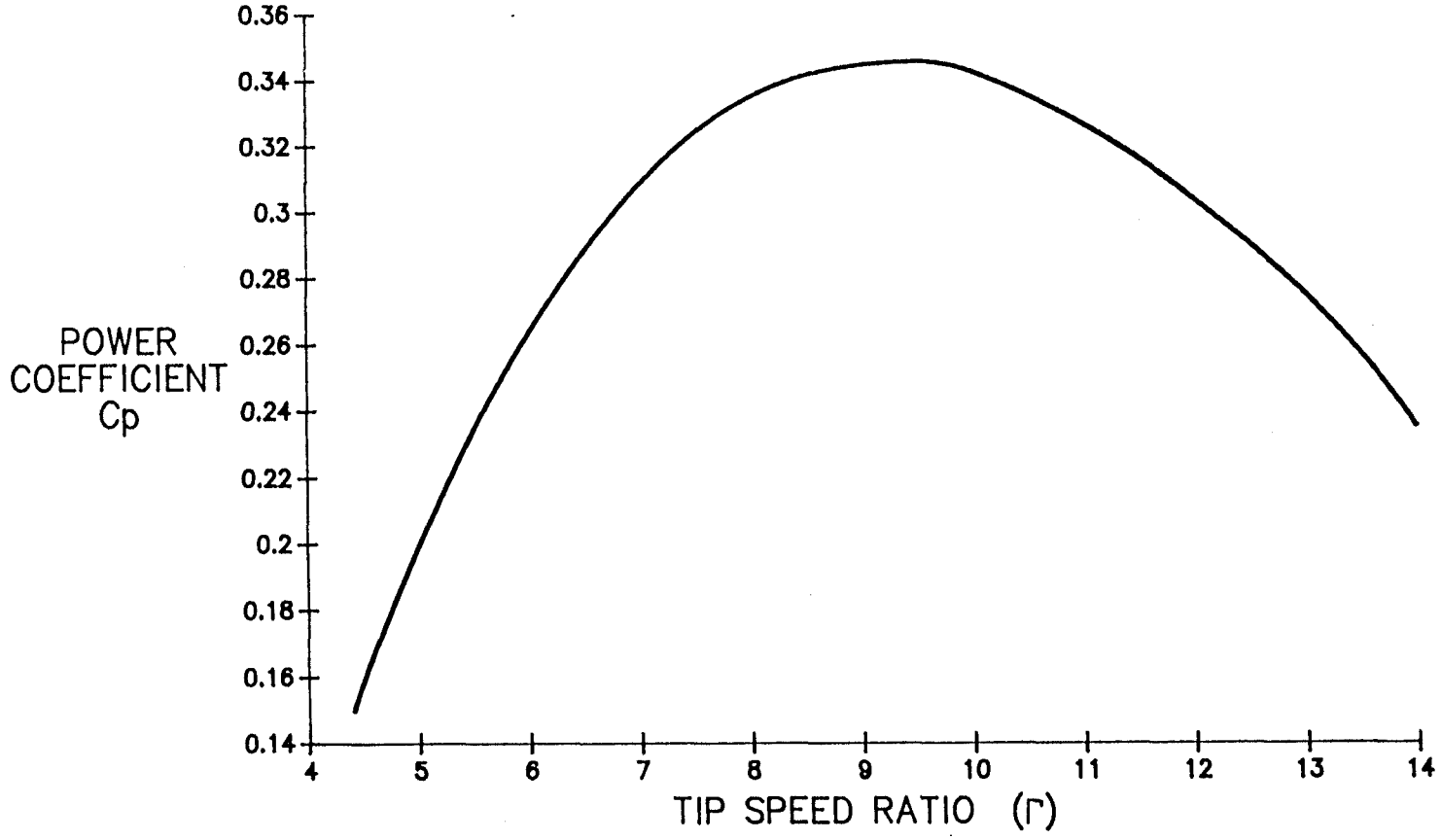

Figure 1.1 Typical HAWT Power Curve

Chapter 2

Development of Equations of Motion

Four degrees-of-freedom are necessary to model a HAWT with a two-bladed, teetered hub connected to a variable speed generator. One degree-of-freedom arises from flapwise motion of each of the two blades. Motion of the blade is confined to the flapwise direction. Edgewise and torsional blade motion are not considered in this study. The direction of the blade flapping is a function of the twist and pitch of the blade, so that the motion is in the direction perpendicular to the axis of the blades smallest moment of inertia. The model allows for blade precone and delta-3. The model also allows for the teetering hub center to be offset from the teeter axis. This length is referred to as undersling. The model has provisions for fixed rotor tilt and yaw. Time varying yaw is not considered. The variable speed generator is driven by the aerodynamic torque, drive train losses, and an arbitrary generator load. The aerodynamic loading is determined using the modified strip theory with nonlinear lift and drag characteristics. The aerodynamics is driven by a wind model that consists of a deterministic portion made up of mean wind, shear, and yaw, and a stochastic portion, consisting of an atmospheric turbulence model. The aerodynamic loads are calculated in the blade deformed

position. The resulting nonlinear equations are solved in the time domain using a predictor-corrector method. The bending moments, shear, and tension forces are integrated along the deformed blade. The derivation of the governing equations of motion is presented in this chapter.

2.1 Geometry and Coordinate Transformations

Figure 2.1 shows the orientation of one turbine blade with all the coordinate systems required for determination of the system equations of motion. These coordinates are defined as

$\mathbf{a}''_i$ = inertial coordinates

$\mathbf{a}'_i$ = yaw coordinates

$\mathbf{a}_i$ = tilt and generator coordinates

$\mathbf{b}_i$ = rotating rotor coordinates

$\mathbf{c}_i$ = rotating teeter coordinates

$\mathbf{d}_i$ = delta-3 rotation coordinates

$\mathbf{e}_i$ = precone rotation coordinates

$\mathbf{f}_i$ = elastic axis rotation coordinates

$\mathbf{g}_i$ = deflected blade coordinates

(i=1,2,3)

The first two coordinate transformations, $\mathbf{a}''$ to $\mathbf{a}'$ and $\mathbf{a}'$ to $\mathbf{a}$, are yaw and tilt rotations respectively, and are used for determination of wind input. The tilt rotation also effects the gravity load on the rotor. The rotor generator and main shaft spin about the $\mathbf{a}_1$ axis. The

rotation about this axis is the variable speed degree-of-freedom, q_4. The rotor assembly teeters about the $\mathbf{b}_2$ axis, with the teeter axis being displaced from the yaw and tilt axes' center by a distance, d. The rotation about the teeter axis is the teeter degree-of- freedom, q_3. The hub is displaced from the teeter axis by the undersling distance, R_u . The axes $\mathbf{c}_1$, $\mathbf{d}_2$, and $\mathbf{e}_3$ define rotations at the hub center for delta-3 (δ_3), precone (β) and the elastic bending axis (θ_p), respectively. The resulting coordinate transformation from the generator coordinate system to the rigid blade coordinate system is given by

$$\begin{Bmatrix} \mathbf{a}_1 \\ \mathbf{a}_2 \\ \mathbf{a}_3 \end{Bmatrix} = \begin{bmatrix} Q^{11} & Q^{12} & Q^{13} \\ Q^{21} & Q^{22} & Q^{23} \\ Q^{31} & Q^{32} & Q^{33} \end{bmatrix} \begin{Bmatrix} \mathbf{f}_1 \\ \mathbf{f}_2 \\ \mathbf{f}_3 \end{Bmatrix} \qquad (2.1.1)$$

where,

$$\begin{aligned}
Q^{11} &= c\theta_p c\beta c q_3 + s\theta_p s\delta_3 s q_3 - c\theta_p s\beta c\delta_3 s q_3 \\
Q^{12} &= -s\theta_p c\beta c q_3 + c\theta_p s\delta_3 s q_3 + s\theta_p s\beta c\delta_3 s q_3 \\
Q^{13} &= s\beta c q_3 + c\beta c\delta_3 s q_3 \\
Q^{21} &= c\theta_p c\beta s q_3 s q_4 + s\theta_p Q^A + c\theta_p s\beta Q^B \\
Q^{22} &= -s\theta_p c\beta s q_3 s q_4 + c\theta_p Q^A - s\theta_p s\beta Q^B \\
Q^{23} &= s\beta s q_3 s q_4 - c\beta (s\delta_3 c q_4 + c\delta_3 c q_3 s q_4) \\
Q^{31} &= -c\theta_p c\beta s q_3 c q_4 + s\theta_p Q^C - c\theta_p s\beta Q^D \qquad (2.1.2) \\
Q^{32} &= s\theta_p c\beta s q_3 c q_4 + c\theta_p Q^C + s\theta_p s\beta Q^D \\
Q^{33} &= -s\beta s q_3 c q_4 + c\beta (-s\delta_3 s q_4 + c\delta_3 c q_3 c q_4) \\
Q^A &= c\delta_3 c q_4 - s\delta_3 c q_3 s q_4 \\
Q^B &= s\delta_3 c q_4 + c\delta_3 c q_3 s q_4 \\
Q^C &= c\delta_3 s q_4 + s\delta_3 c q_3 s q_4 \\
Q^D &= -s\delta_3 s q_4 + c\delta_3 c q_3 c q_4
\end{aligned}$$

($\cos(q_4)$ is written as cq_4, $\sin(q_4)$ as sq_4, and so on

for brevity)

For determination of aerodynamic loads, the transformation from rigid blade coordinates to the deformed blade coordinates can be taken as a local rotation about the f_2 axis. This must be done for each blade element with a rotation ζ. The transformation between the rigid and deformed blade coordinates is given by

$$\begin{Bmatrix} f_1 \\ f_2 \\ f_3 \end{Bmatrix} = \begin{bmatrix} \cos(\zeta) & 0 & -\sin(\zeta) \\ 0 & 1 & 0 \\ \sin(\zeta) & 0 & \cos(\zeta) \end{bmatrix} \begin{Bmatrix} g_1 \\ g_2 \\ g_3 \end{Bmatrix} \qquad (2.1.3)$$

2.2 Blade Deflection

The displacement of each blade is modeled as a single degree-of-freedom in a direction perpendicular to the axis of the blades smallest moment of inertia. This is not necessarily perpendicular to the swept rotor plane due to twist and pitch. Blade deflection tangential to the axis of the smallest moment of inertia is zero, although provisions have been left in the code for future development. Deflection in the radial direction can be expressed as a function of the flapwise displacement. Displacement of the blade is given by a product of an assumed mode shape and a function of time. This relation for displacement in the flapwise or f_1 blade coordinate direction can be expressed as

$$u_{1i} = \varphi_1(r)q_i(t) \qquad (i = 1,2) \qquad (2.2.1)$$

where,

q(t) = the blade displacement, a function of time

$\phi_i(r)$ = the assumed mode shape, a function of the blade coordinate r. (i=1,2 blade number)

The displacement in the tangential or f_2 blade coordinate can be expressed in the same manner as

$$u_{2i} = \varphi_2(r)q_i(t) \qquad (i=1,2) \qquad (2.2.2)$$

For this model the assumed mode shape $\phi_2(r)$ is zero for all values of r.

For a small blade deflection as shown in Figure 2.2, the radial deflection can be expressed as

$$u_{3i} = \int_0^r \cos\left(\frac{\partial u_{1i}}{\partial r}\right) dr \qquad i=1,2 \qquad (2.2.3)$$

taking the first two terms from a Taylor series of the cosine function and linearizing gives

$$\cos\left(\frac{\partial u_i}{\partial r}\right) = 1 - 2\sin^2\frac{\partial u_i}{\partial r} \approx 1 - \frac{1}{2}\left(\frac{\partial u_i}{\partial r}\right)^2 \qquad (2.2.4)$$

so that

$$u_{3i} = r - \frac{1}{2}q_i^2\int_0^r \left(\frac{\partial \varphi_i}{\partial r}\right)^2 dr \qquad (i=1,2) \qquad (2.2.5)$$

The local blade element rotation used for equation 2.1.3 can be approximated as the slope of the displacement function given as

$$\zeta_i(r) = q_i(t)\frac{\partial \varphi_1}{\partial r} \qquad (i=1,2) \qquad (2.2.6)$$

The choice for the shape function was determined using the following relation developed by Wilson et al [1], for an Euler beam that has stiffness that varies as

$$EI = kr^{-b} \qquad (2.2.7)$$

where k is a constant, r is the distance from the fixed hub, and $b \geq 0$. For a uniformly loaded cantilevered beam with stiffness variation as given in equation 2.2.6 the static deflection (normalized to unity at the blade tip) is given by

$$\varphi_a(z) = \frac{z^{b+2}}{6}[(1+b)(2+b)z^2 - 2(1+b)(4+b)z + (3+b)(4+b)] \qquad (2.2.8)$$

where $z=(r-R_H)/(R-R_H)$, R is the length of the blade, and R_H is the hub length. For a cantilevered beam with a force acting at the tip and the stiffness given in equation 2.2.6 the static deflection (normalized to unity at the tip) is given by

$$\varphi_b(z) = \frac{z^{b+2}}{2}[(3+b) - (1+b)z] \qquad (2.2.9)$$

For a cantilevered beam with a uniform load and a force acting at the tip (ie. a tip mass) the relation for the static deflection is a weighted superposition of equations 2.2.8 and 2.2.9, written as

$$\varphi(z) = w\varphi_a(z) + (1-w)\varphi_b(z) \qquad (2.2.10)$$

where w is a weighting factor between one and zero. Wilson and Hartin [1] found that the parameter b could be found by calculating the bending natural frequency for a range of values of b and selecting the value of b that minimizes the flapwise bending frequency. This procedure can be extended to find a combination of values w and b that minimizes the bending natural frequency. For the ESI-80, the turbine used for comparison in this thesis and described in Appendix A, minimizing values were found to be 1.3 for b and 0 for w. These values were used for the rest of the analysis.

2.3 Blade Kinematics

Expressions for the velocity and acceleration of an arbitrary point on the blade is required for determining blade equations of motion and blade forces. A position vector of an arbitrary point Q on the i^{th} deformed blade can be written as

$$({}^N\mathbf{p}^Q)_i = p_{1i}\mathbf{f}_1 + p_{2i}\mathbf{f}_2 + p_{3i}\mathbf{f}_3 \qquad (i=1,2) \qquad (2.3.1)$$

where,

$$\begin{aligned} p_{1i} &= u_{1i} - R_U\cos(\beta) \\ p_{2i} &= u_{2i} \\ p_{3i} &= u_{3i} - R_U\sin(\beta) \qquad (i=1,2) \end{aligned} \qquad (2.3.2)$$

where $({}^N\mathbf{p}^Q)_i$ is the position vector of a point Q in the

inertial reference frame N. The displacements u_{1i}, u_{2i}, and u_{3i} are given in the relations 2.2.1, 2.2.2, and 2.2.5, respectively. The velocity of the point Q is the time derivative of the position vector in 2.3.1 given by

$$({}^N\mathbf{v}^Q) = \left(\frac{({}^N d\,{}^N\mathbf{p}^Q)}{dt}\right) \tag{2.3.3}$$

this can be expressed in the rigid blade coordinate as

$$({}^N\mathbf{v}^Q)_i = v_{1i}\mathbf{f}_1 + v_{2i}\mathbf{f}_2 + v_{3i}\mathbf{f}_3 \tag{2.3.4}$$

where,

$$\begin{aligned} v_{1i} &= \dot{u}_{1i} + (w_2 p_{3i} - w_3 p_{2i}) \\ v_{2i} &= \dot{u}_{2i} + (w_3 p_{1i} - w_1 p_{3i}) \\ v_{3i} &= \dot{u}_{3i} + (w_1 p_{2i} - w_2 p_{1i}) \end{aligned} \tag{2.3.5}$$

where,

$$\begin{aligned} \dot{u}_{1i} &= \dot{q}_i \varphi_1 \\ \dot{u}_{2i} &= \dot{q}_i \varphi_2 = 0 \\ \dot{u}_{3i} &= -\dot{q}_i q_i \int_0^r \left(\frac{\partial \varphi}{\partial r}\right)^2 dr \qquad (1=1,2) \end{aligned} \tag{2.3.6}$$

and,

$$\begin{aligned} w_1 &= \dot{q}_4 Q^{11} + \dot{q}_3(\cos(q_4) Q^{21} + \sin(q_4) Q^{31}) \\ w_2 &= \dot{q}_4 Q^{12} + \dot{q}_3(\cos(q_4) Q^{22} + \sin(q_4) Q^{32}) \\ w_3 &= \dot{q}_4 Q^{13} + \dot{q}_3(\cos(q_4) Q^{23} + \sin(q_4) Q^{33}) \end{aligned} \tag{2.3.7}$$

where q_3 and q_4 are the teeter and variable speed degrees-of-freedom, respectively, and $\dot{q}_3$ and $\dot{q}_4$ are their time derivatives. Q^{11} through Q^{33} are transformations given in equation 2.1.1.

The acceleration of point Q is the time derivative of

the velocity vector given in equation 2.3.4 given by

$$({}^N\mathbf{a}^Q) = \left(\frac{({}^N d^N \mathbf{v}^Q)}{dt}\right) \tag{2.3.8}$$

this can be expressed in the rigid blade coordinates as

$$({}^N\mathbf{a}^Q)_i = a_{1i}\mathbf{f}_1 + a_{2i}\mathbf{f}_2 + a_{3i}\mathbf{f}_3 \tag{2.3.9}$$

where (without the indice i),

$$\begin{aligned} a_1 &= \ddot{u}_1 + 2(w_2\dot{u}_3 - w_3\dot{u}_2) + (w_2v_3 - w_3v_2) + (\alpha_2p_3 - \alpha_3p_2) \\ a_2 &= \ddot{u}_2 + 2(w_3\dot{u}_1 - w_1\dot{u}_3) + (w_3v_1 - w_1v_3) + (\alpha_3p_1 - \alpha_1p_3) \\ a_3 &= \ddot{u}_3 + 2(w_1\dot{u}_2 - w_2\dot{u}_1) + (w_1v_2 - w_2v_1) + (\alpha_1p_2 - \alpha_2p_1) \end{aligned} \tag{2.3.10}$$

where, w_1, w_2, and w_3 are given in Eq. 2.3.7, v_1, v_2, and v_3 are given in Eq. 2.3.5, and u_1, u_2, and u_3 are given in Eq. 2.3.6, and,

$$\begin{aligned} \ddot{u}_{1i} &= \ddot{q}_i\varphi_1 \\ \ddot{u}_{2i} &= \ddot{q}_i\varphi_2 = 0 \\ \ddot{u}_{3i} &= -(\ddot{q}_i + (\dot{q}_i)^2)\int_0^r \left(\frac{\partial\varphi}{\partial r}\right)^2 dr \end{aligned} \tag{2.3.11}$$

and,

$$\begin{aligned} \alpha_1 &= \ddot{q}_4Q^{11} + \ddot{q}_3Q^{W1} + \dot{q}_3\dot{q}_4Q^{A1} \\ \alpha_2 &= \ddot{q}_4Q^{12} + \ddot{q}_3Q^{W2} + \dot{q}_3\dot{q}_4Q^{A2} \\ \alpha_3 &= \ddot{q}_4Q^{13} + \ddot{q}_3Q^{W3} + \dot{q}_3\dot{q}_4Q^{A3} \\ Q^{W1} &= \cos(q_4)Q^{21} + \sin(q_4)Q^{31} \\ Q^{W2} &= \cos(q_4)Q^{22} + \sin(q_4)Q^{32} \\ Q^{W3} &= \cos(q_4)Q^{23} + \sin(q_4)Q^{33} \\ Q^{A1} &= \cos(q_4)Q^{31} - \sin(q_4)Q^{21} \\ Q^{A2} &= \cos(q_4)Q^{32} - \sin(q_4)Q^{22} \\ Q^{A3} &= \cos(q_4)Q^{33} - \sin(q_4)Q^{23} \end{aligned} \tag{2.3.12}$$

the $\ddot{q}$'s are the second time derivatives of the q's and Q^{11} through Q^{33} are transformation given in 2.1.1. The

angular velocity can be written using Eq. 2.3.7 as

$$({}^{N}\mathbf{w}^{Q}) = w_1\mathbf{f}_1 + w_2\mathbf{f}_2 + w_3\mathbf{f}_3 \qquad (2.3.13)$$

The angular acceleration can be written using Eq. 2.13.12 as

$$({}^{N}\boldsymbol{\alpha}^{Q}) = \alpha_1\mathbf{f}_1 + \alpha_2\mathbf{f}_2 + \alpha_3\mathbf{f}_3 \qquad (2.3.14)$$

2.4 Aerodynamic Loading

The method for determination of aerodynamic loads is based on the momentum theory. The momentum theory applies continuity, momentum, and energy to the flow passing through the rotor plane. Figure 2.3 shows the one-dimensional flow past the rotor. Two expressions for the thrust on the rotor can be found. From a conservation of momentum

$$\frac{dT}{dA} = \rho u(V_\infty - u) \qquad (2.4.1)$$

where dT/dA is the axial force per unit area on the actuator disk, ρ is the fluid density, and V_∞ and u are velocities defined on Figure 2.3. From the Bernoulli equation

$$\frac{dT}{dA} = \Delta P \qquad (2.4.2)$$

where ΔP is the pressure difference across the actuator disk expressed as

$$\Delta P = P^{+} - P^{-} = \frac{1}{2}\rho(V_\infty^2 - u_1^2) \qquad (2.4.3)$$

Solving equations 2.4.1 and 2.4.2 gives the velocity in the rotor disk as

$$u = \frac{1}{2}(V_\infty + u_1) \qquad (2.4.4)$$

Defining a as the axial induction factor through the relation $aV_\infty = V_\infty - u$ the momentum relation Eq. 2.4.1 can be written as

$$\frac{dT}{dA} = 2\, V_\infty^2\, a\, (1 - a) \qquad (2.4.5)$$

By defining the rotor thrust coefficient as

$$C_T = \frac{\frac{dT}{dA}}{\frac{1}{2}\rho V_\infty^2} \qquad (2.4.6)$$

the thrust coefficient can be expressed as a function of the axial induction factor

$$C_T = 4\, a\, (1 - a) \qquad (2.4.7)$$

The effect of the wake expansion on the thrust coefficient was studied by Glauret both empirically [2] and analytically [3]. The follwing expression given by Wilson and Walker [4] can be used to specify the thrust coefficient

$$\begin{aligned} C_T &= 4\, a\, F\, (1 - a) && a \le a_c \\ C_T &= C_{T_{ac}} + \frac{\partial C_T}{\partial a}\Big|_{ac}(a - a_c) && a > a_c \end{aligned} \qquad (2.4.8)$$

A value of $a_c = 0.2$ gives the best fit to the data. F

is a tip loss factor, given by Prandtl [5] as follows

$$F = \frac{2}{\pi} \cos^{-1} \left[\exp \frac{-B\,(R - r)}{2\,\pi\, r \sin\phi_\alpha}\right] \qquad (2.4.9)$$

Strip theory combines the momentum theory with a blade element theory and is based on the assumption that the flow through the rotor can be divided into individual streamtubes that can be analyzed independently. The advantage of strip theory is the axial induction factors can be found for each element independently of one another. The thrust relation Eq. 2.4.8 can be related to the blade element thrust coefficient, which is given as follows

$$C_T = \frac{B\,c\,(1 - a)^2\, C_L \cos\phi_\alpha}{2\,\pi\, r \sin^2\phi_\alpha} \qquad (2.4.10)$$

where,

$$\phi_\alpha = \tan^{-1} \frac{V_\infty\,(1 - a)}{r\Omega} \qquad (2.4.11)$$

A solution to Eq's. 2.4.8, 2.4.10, 2.4.11, and 2.4.12 can be found in an iterative manner to give the steady-state axial induction factor. This allows the lift and drag to be determined along the blade for any blade azimuth location, as follows.

$$\begin{aligned} \text{Lift / (unit length)} &= \frac{1}{2}\,\rho\, W^2\, c\, C_L \\ \text{Drag / (unit length)} &= \frac{1}{2}\,\rho\, W^2\, c\, C_D \end{aligned} \qquad (2.4.13)$$

Referring to the geometry of Figure 2.4, the lift and drag can be resolved onto the blade coordinates such that

the aerodynamic forces acting on a blade element can be written as

$$\mathbf{f} = f_n \mathbf{f}_1 + f_t \mathbf{f}_2 \qquad (2.4.14)$$

where,

$$\begin{aligned} f_n &= L \cos\phi_\alpha + D \sin\phi_\alpha \\ f_t &= -L \sin\phi_\alpha + D \cos\phi_\alpha \end{aligned} \qquad (2.4.15)$$

where, L = lift, and D = drag.

2.5 Equations of Motion

The kinematics and forces are evaluated at discete points along the blades, so that determination of the equations of motion requires numeric integration along the blades. The methods of Kane and Levinson [6] were used for obtaining the equations of motion. The equations are of the form

$$F_r + F_r^* = 0 \qquad (2.5.1)$$

where,

F_r = generalized active force

F_r^* = generalized inertia force

The subscript r refers to the number of generalized coordinates. In this model, the number of generalized coordinates is equivalent to the number of degrees-of-freedom. As defined in section 2.1, r=1 and r=2 correspond to the blade deflections of the two blades, r=3 for the

teeter angle, and r=4 for the variable speed. The generalized active forces are determined from the blade kinematics using

$$F_r = \mathbf{V}_r^Q \cdot \mathbf{R} + \boldsymbol{\omega}_r^Q \cdot \mathbf{T} \qquad r=1,4 \qquad (2.5.3)$$

where,

$\mathbf{V}_r^Q$ = holonomic partial velocity of point Q

$\mathbf{R}$ = resultant of all external force

$\boldsymbol{\omega}_r^Q$ = holonomic partial angular velocity of point Q

$\mathbf{T}$ = resultant torque of all external torques

The generalized inertia forces are determined using the followind relation

$$F_r^* = \mathbf{V}_r^Q \cdot (-m\,\mathbf{a}^Q) + \boldsymbol{\omega}_r^Q \cdot (-\boldsymbol{\alpha} \cdot \mathbf{I} - \boldsymbol{\omega} \times \mathbf{I} \cdot \boldsymbol{\omega}) \qquad r=1,4 \qquad (2.5.3)$$

where,

m = mass per unit length of the blade

$\mathbf{a}^Q$ = acceleration of point Q, Eq. 2.3.9

$\mathbf{I}$ = Inertia dyadic of blade element Q

$\boldsymbol{\alpha}$ = angular acceleration of point Q, Eq. 2.3.14

$\boldsymbol{\omega}$ = angular velocity of point Q, Eq. 2.3.13

The generalized speeds are defined as $u_r=q_r$ (r=1,4). The partial velocities can be found from the expression for blade velocity, Eq. 2.3.5,

$$
\begin{aligned}
\mathbf{v}_r^{q_j} &= \phi_{1r}\mathbf{f}_1 + \phi_{2r}\mathbf{f}_2 - q_r\int_0^r \left(\frac{\partial\phi}{\partial r}\right)^2 dr\,\mathbf{f}_3 \quad j=r \\
\mathbf{v}_r^{q_j} &= 0 \qquad j\neq r \qquad r = 1,2 \\
\mathbf{v}_3^{q_j} &= N_{31}^j\mathbf{f}_1 + N_{32}^j\mathbf{f}_2 + N_{33}^j\mathbf{f}_3 \quad r = 1,2 \\
\mathbf{v}_4^{q_j} &= N_{41}^j\mathbf{f}_1 + N_{42}^j\mathbf{f}_2 + N_{43}^j\mathbf{f}_3 \quad r = 1,2
\end{aligned}
\tag{2.5.4}
$$

where,

$$
\begin{aligned}
N_{31} &= Q^{W2}P_3 - Q^{W3}P_2 \\
N_{32} &= Q^{W3}P_1 - Q^{W1}P_3 \\
N_{33} &= Q^{W1}P_2 - Q^{W2}P_1 \\
N_{41} &= Q^{12}P_3 - Q^{13}P_2 \\
N_{42} &= Q^{13}P_1 - Q^{11}P_3 \\
N_{43} &= Q^{11}P_2 - Q^{12}P_1
\end{aligned}
\tag{2.5.5}
$$

The partial angular velocities can be found from the expression for blade angular velocity, Eq. 2.3.13,

$$
\begin{aligned}
\boldsymbol{\omega}_r^{q_j} &= 0 \qquad r = 1,2 \\
\boldsymbol{\omega}_3^{q_1} &= \mathbf{b}_2 \\
\boldsymbol{\omega}_3^{q_2} &= -\mathbf{b}_2 \\
\boldsymbol{\omega}_4^{q_j} &= \mathbf{a}_1 \qquad j = 1,2
\end{aligned}
\tag{2.5.6}
$$

The resultant **R** can be written as a combination of aerodynamic Eq. 2.4.5 and gravity forces

$$
\mathbf{R} = R_1\mathbf{f}_1 + R_2\mathbf{f}_2 + R_3\mathbf{f}_3 \tag{2.5.7}
$$

where,

$$
\begin{aligned}
R_1 &= -m\,g\,(\cos(\chi)Q^{21} - \sin(\chi)Q^{11}) + f_n \\
R_2 &= -m\,g\,(\cos(\chi)Q^{22} - \sin(\chi)Q^{12}) + f_t \\
R_3 &= -m\,g\,(\cos(\chi)Q^{23} - \sin(\chi)Q^{13})
\end{aligned}
\tag{2.5.8}
$$

The resultant torque **T** is due solely to that of the

restraining torque of the generator. The generator model is discussed in section 2.6. The relation for the generalized inertia forces can be taken as

$$F_r^* = -\sum_{j=1}^{2} \left(\int_0^R \mu \mathbf{v}_r^{q_j} \cdot \mathbf{a}^0 \, dr \right) \qquad r = 1,4 \qquad (2.5.9)$$

This relation can be expanded into a form where the second time derivatives are extracted so that the equations can be written in the form

$$[\mathbf{M}]\{\ddot{\mathbf{q}}\} = \{\mathbf{G}\} \qquad (2.5.10)$$

This form lends itself to a predictor-corrector scheme for solution of the equations. With this in mind, the first two generalized inertia forces can written as

$$\begin{aligned} F_r^* = & -\ddot{q}_r \int_0^R \mu \left(\phi_1^2 + \left(q_r \int_0^r \left(\frac{\partial \phi}{\partial r} \right)^2 d\bar{r} \right)^2 \right) dr \\ & -\ddot{q}_3 \int_0^R \mu \left[\left(Q^{W2} P_3 - Q^{W3} P_2 \right) \phi_1 + \left(Q^{W1} P_2 - Q^{W2} P_1 \right) \phi_3 \right] dr \\ & -\ddot{q}_4 \int_0^R \mu \left[\left(Q^{12} P_3 - Q^{13} P_2 \right) \phi_1 + \left(Q^{11} P_2 - Q^{12} P_1 \right) \phi_3 \right] dr \\ & -g_r(q_i \, , \, \dot{q}_i) \qquad r = 1,2 \qquad i = 1,4 \end{aligned} \qquad (2.5.11)$$

where,

$$\phi_3 = (-\int_0^r (\frac{\partial \phi}{\partial \bar{r}})^2 d\bar{r})$$

$$g_r(q_i, \dot{q}_i) = \dot{q}_3 \dot{q}_4 \int_0^R \mu \left[(Q^{A2}P_3 - Q^{A3}P_2)\phi_1 + (Q^{A1}P_2 - Q^{A2}P_1)\phi_3 \right] dr$$

$$-\int_0^R \mu \left[(W_2V_3 - W_3V_2)\phi_1 + (W_1V_2 - W_2V_1)\phi_3 + \dot{q}_r^2\phi_3 \right]$$

$$r = 1,2 \qquad (2.5.12)$$

The second two generalized inertia forces can be written as

$$F_r^* = -\sum_{j=1}^{2} [\ddot{q}_j \int_0^R \mu(\phi_1 N_{r1}^j + \phi_3 N_{r3}^j) dr + \frac{1}{2}\ddot{q}_4 I_{\text{generator}} \qquad (\text{if } r = 4)$$

$$-\ddot{q}_3 \int_0^R \mu [(Q^{W2}P_1 - Q^{W3}P_2) N_{r1} + (Q^{W3}P_1 - Q^{W1}P_3) N_{r2} + (Q^{W1}P_2 - Q^{W2}P_1) N_{r3}] dr$$

$$-\ddot{q}_4 \int_0^R \mu [(Q^{12}P_3 - Q^{13}P_2) N_{r1} + (Q^{13}P_1 - Q^{11}P_3) N_{r2} + (Q^{11}P_2 - Q^{12}P_1) N_{r2}] dr$$

$$-g_r(q_i, \dot{q}_i)] \qquad r = 3,4 \quad i = 1,4 \qquad (2.5.13)$$

where,

$$g_r(q_i, \dot{q}_i) = \dot{q}_3 \dot{q}_4 \int_0^R [(Q^{A2}P_3 - Q^{A3}P_2) N_{r1}^j + (Q^{A3}P_1 - Q^{A1}P_3) N_{r2}^j + (Q^{A1}P_2 - Q^{A2}P_1) N_{r3}^j] dr$$

$$+2 \int_0^R [(W_2\dot{U}_3 - W_3\dot{U}_2) N_{r1}^j + (W_3\dot{U}_1 - W_1\dot{U}_3) N_{r2}^j + (W_1\dot{U}_2 - W_2\dot{U}_1) N_{r3}^j] dr$$

$$+ \int_0^R [(W_2V_3 - W_3V_2) N_{r1}^j + (W_3V_1 - W_1V_3) N_{r2}^j + (W_1V_2 - W_2V_1) N_{r3}^j] dr$$

$$+\dot{q}_j^2 \int_0^R (\phi_3 N_{r3}^j) dr \qquad r = 3,4 \quad j = 1,2$$

$$+ \dot{q}_4^2 I_{\text{generator}} \quad (\text{If } r=4) \qquad (2.5.14)$$

The first two generalized active forces can be written as

$$F_r = \int_0^R (R_1\phi_1 + R_3\phi_3 - q_r \int_0^r EI(\frac{\partial^2\phi}{\partial\bar{r}^2})^2 d\bar{r} - q_r \int_0^r \dot{q}_4^2 \mu (\frac{\partial\phi}{\partial\bar{r}})^2 d\bar{r}) dr \qquad r = 1,2 \tag{2.5.15}$$

The second two terms arise from the relation between the potential and the generalized active force

$$F_r = - \frac{\partial V}{\partial q_r} \tag{2.5.16}$$

where, the potential for a blade element is given as

$$V = \frac{1}{2}\int_0^r EI\ (\frac{\partial^2 u_1}{\partial\bar{r}^2})^2 d\bar{r} + \frac{1}{2}\int_0^r \dot{q}_4^2\ \mu\ (\frac{\partial u_1}{\partial\bar{r}})^2 d\bar{r} \tag{2.5.17}$$

The second two generalized active forces can be written as

$$F_r = \sum_{j=1}^{2} [\ \int_0^R (R_1 N_{r1}^j + R_2 N_{r2}^j + R_3 N_{r3}^j) dr\ ] + \mathbf{T}\cdot \boldsymbol{\omega}_r^{q_j} \qquad r = 3,4 \tag{2.5.18}$$

where, $\mathbf{T}$ is the generator restaining torque. The hub mass has a contribution to the third and fourth generalized active and inertia forces.

$$
\begin{aligned}
F_{3_{HUB}} &= M_{HUB}\, R_U\, g(\cos\chi\cos q_3 \sin q_4 + \sin\chi\sin q_3) \\
F_{4_{HUB}} &= M_{HUB}\, R_U\, g(\cos\chi \sin Q_3 \cos q_4) \\
F^*_{3_{HUB}} &= -\ddot{q}_3[M_{HUB}\, R_U + I_{HUB}] - M_{HUB}\, R_U\, \dot{q}_4^2 \sin q_3 \cos q_3 \\
F^*_{4_{HUB}} &= -\ddot{q}_4[M_{HUB}\, R_U \sin^2 q_3] \\
&\quad -M_{HUB}\, R_U\, \dot{q}_3 \dot{q}_4 \sin q_3 \cos q_3
\end{aligned}
\qquad (2.5.19)
$$

The generalized active and inertia forces are combined using equation 2.5.1 into the form of equation 2.5.10 for numerical solution.

2.6 Generator Model

Two variable speed generator models are to be used for the generator restaining torque. The first model is for an induction generaotr that has small variations about a rated rotation speed due to generator slip. The second model is for a variable speed generator operating at a constant tip speed ratio.

For an induction generator the restaining torque can be divided into two components

$$T = T_{electrical} + T_{losses} \qquad (2.6.1)$$

where,

$$
\begin{aligned}
T_{electrical} &= \frac{c_e\, N^2}{\eta_{GB}}\,(\Omega - \Omega_0) \\
T_{losses} &= \frac{N}{\eta_{GB}}\left(T_{fixed}\left(\frac{\Omega}{\Omega_0}\right) + T_{variable}\left(\frac{\Omega - \Omega_0}{\Omega_R - \Omega_0}\right)^2\right)
\end{aligned}
\qquad (2.6.2)
$$

where, N is the gearbox step up ratio, η_{GB} is the gearbox efficiency, and c_e, Ω_0, and Ω_R are constants. The

fixed and variable losses are functions of the generator fixed loss factor f and can be expressed as

$$T_{fixed} = f\ (\frac{1}{\eta_{GEN}} - 1)\frac{P_{Rated}}{\Omega_R}$$
$$T_{variable} = (1 - f)\,(\frac{1}{\eta_{GEN}} - 1)\frac{P_{Rated}}{\Omega_R} \qquad (2.6.3)$$

where, η_{GEN} is the generator maximum efficiency and P_{Rated} is the generator rated power output.

The variable speed generator operating at constant tip speed ratio should have a restaining torque that varies to allow the rotor speed to follow the wind speed preserving the tip speed ratio, $R\Omega/V$. In most wind turbine applications, future wind speed measurements are not available. The variable speed controller has only past torque and wind histories to use in it's control algorithm. This can result in the generator lagging the wind reducing the power captured. The following relation for the generator restraining torque follows the optimum power coefficient as a function of the tip speed ratio, λ. The tip speed ratio used in this relation is based on a moving average of the last 100 tip speed ratios. This results in slowly varying torque.

$$T = \frac{\frac{1}{2}\,\pi\,\rho\,V^2\,R^3\,C_p}{\lambda} \qquad (2.6.4)$$

The variable speed generator can be used as a start-up motor or a shut down brake. For a motor configuration the generator torque has a negative sign. The generator

braking torque must be greater than the aerodynamic torque for deceleration of the rotor. Both the motor and brake can be a function of time, rotor speed, or any other generator variable.

2.7 Deterministic Wind Model

The deterministic wind model consists of two parts, wind shear and tower shadow. The shear model uses a power law expression to determine the velocity distribution with height, as follows

$$V = v_{HUB} \left(1 - \frac{r \sin q_4}{H_{HUB}} \right)^n \qquad (2.7.1)$$

where, q_4 is the azimuth angle, which starts when the blade is horizontal to the ground. The blade starts moving downward, therefore a negative sign is used in equation 2.7.1. H_{HUB} is the hub height, r is the blade radius location, and n is the power law exponent.

The tower shadow occurs when the blade is straight down and in the wake from the upstream tower. The shadow model assumes the tower wake to have a cosine-squared shaped deficit where the blade passes through it. Assuming a wake width of two diameters, an expression for the velocity distribution can be found using a momentum balance

$$V(y) = V_\infty \left(1 - \epsilon \cos^2\left(\frac{\pi}{2}\frac{y}{D}\right)\right) \qquad (2.7.2)$$

where, the velocity deficit can be expressed as a function of the tower drag coefficient, as follows

$$\epsilon = \left(\frac{2}{3}\right)\left[1 - \left(1 - \frac{3\,C_D}{2}\right)^{\frac{1}{2}}\right] \qquad (2.7.3)$$

In the case of the ESI-80, the tower has three legs in a truss arrangement. The tower diameter d in equation 2.7.2 can be expressed as the distance between two legs and the tower drag coefficient C_D is the sum of the individual tower leg drag coefficients.

2.8 Numerical Solution Technique

A numerical solution of the four equations of motion is achieved using a fourth-order Adams-Bashforth Predictor formula together with an Adams-Moulton Corrector formula. This numerical method is not self starting, therefore a fourth-order Runge-Kutta method is employed to calculate the first three points.

2.9 Code Organization

The computer code based on the previous theoretical development was named the DRT code. A detailed description of the procedure to operate this code can be found in the

DRT users manual [7].

The DRT code is written in standard FORTRAN 77. The code operates in the time domain using time as the marching variable. Figure 2.5 shows a flowchart of the different subroutines used. Subroutine INPUT reads in the input file containing the characteristics of the turbine to be modeled. Subroutine INTERP takes the blade data and interpolates them at a constant blade increment. This increment is the integration increment used for calculation of the generalized active and inertial forces. Subroutine COEF determines a number of values that are used repeatedly through out the program and calculates the blade mode shapes. The main program starts at time equal to zero. The total time the code will run depends on the options chosen. The teeter and variable speed degrees-of-freedom can be turned off independently. The variable speed option can be a start-up, shut down, or normal operation with two different generator models. Subroutine SOLVER solves the four equations of motion using the numerical scheme described in section 2.8. Subroutine RTHS (right hand side) calculates the generalized active and inertia forces and integrates them down both blades. RTHS calls subroutines TRANS, CALC, GENTORQ, and GAUSS. Subroutine TRANS calculates the coordinate transformations given in Eq. 2.3.12. Subroutine CALC determines the aerodynamic normal and tangential forces, Eq. 2.4.15, based on the method described in section 2.4. Subroutine CALC calls

subroutine WIND, which calculates the wind shear and tower shadow contributions described in section 2.7. Subroutine CALC calls subroutine AERO, which has the lift and drag airfoil characteristics as a function of angle of attack and airfoil thickness. Subroutine GENTORQ supplies the generator restraining torque based on a model from section 2.6. Subroutine GAUSS inverts the matrix Eq. 2.5.10 for solution in Subroutine SOLVER. If turbulence is desired the turbulent wind values are read by subroutine RTHS for every time increment. The main program checks after every new set of values are calculated to see if it should be writing loads to the output file and to see if has completed a simulation. The various loads; blade bending moments, rotor torque, rotor thrust, and the generator output power are calculated in subroutine RTHS.

2.10 References

1. Wilson, R.E., Hartin, J.R., "Mode Shapes for Wind Turbine Vibration Analysis," ASME J. Solar Engr., May, 1990.

2. Glauret, H., "The Analysis of Experimental Results in Windmill Brake and Vortex Ring States of an Airscrew," ARC Reports and Memoranda, No. 1026, 1926.

3. Glauret, H., "On Contradiction of the Slipstream of an Airscrew," ARC Reports and Memoranda, No. 1067, 1926.

4. Wilson, R.E., Walker, S.N., "Performance Analysis of HAWTS," Oregon State University, Corvallis, Oregon, September 1984.

5. Prandtl, L, "Appendix to Schraubenpropellor mit Gerngstein Energieverlust," by Betz, A, Guttingen Nachr, 1919.

6. Kane, T.R., Levinson, D.A., Dynamics: Theory and Applications, McGraw-Hill Book Co, New York, 1985.

7. Weber, T.L., Walker, S.N., Wilson, R.E., "User's Manual for the DRT Rotor Code," Oregon State University, SERI XG-0-19165-1, 1991.

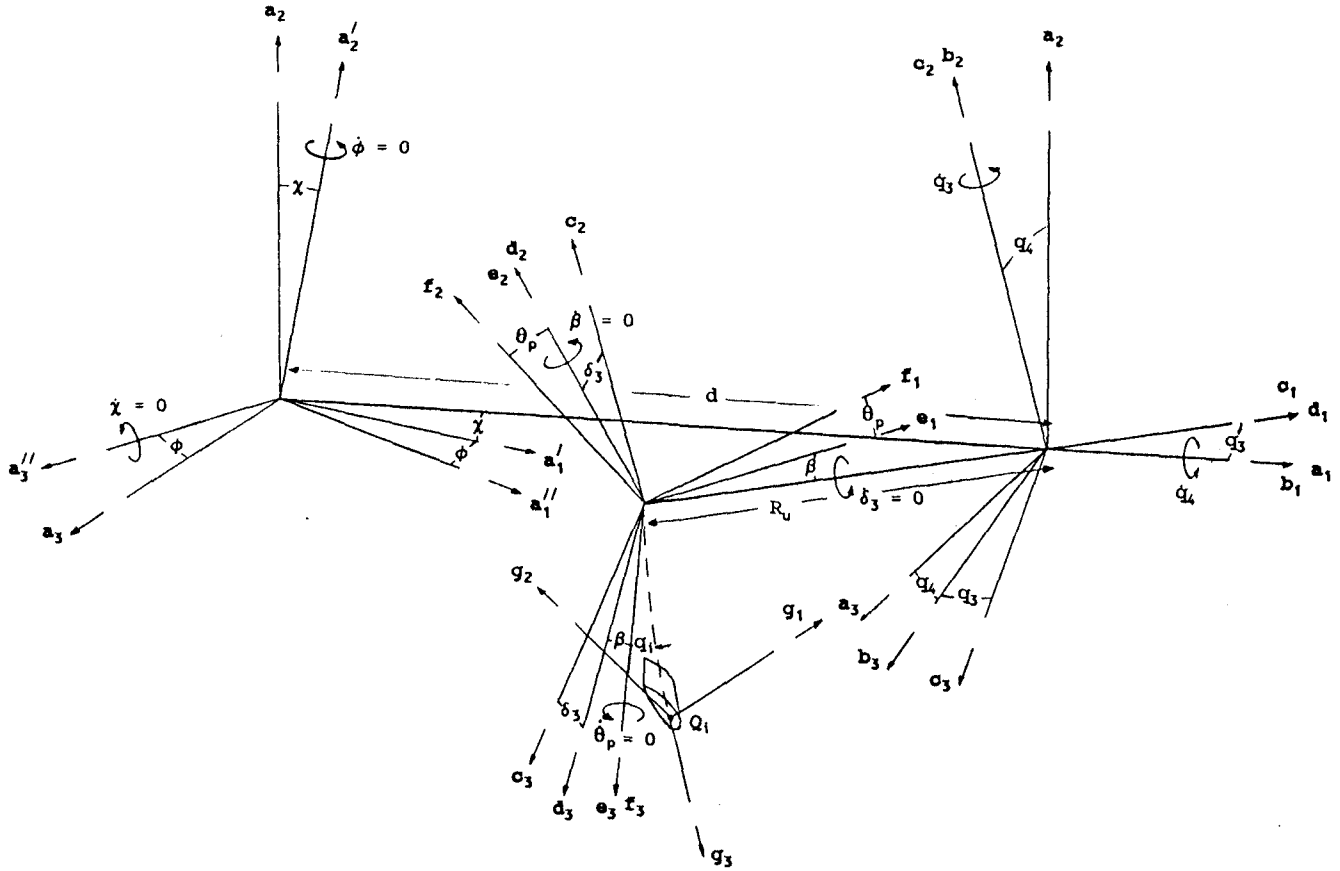

Figure 2.1 Rotor Coordinate System

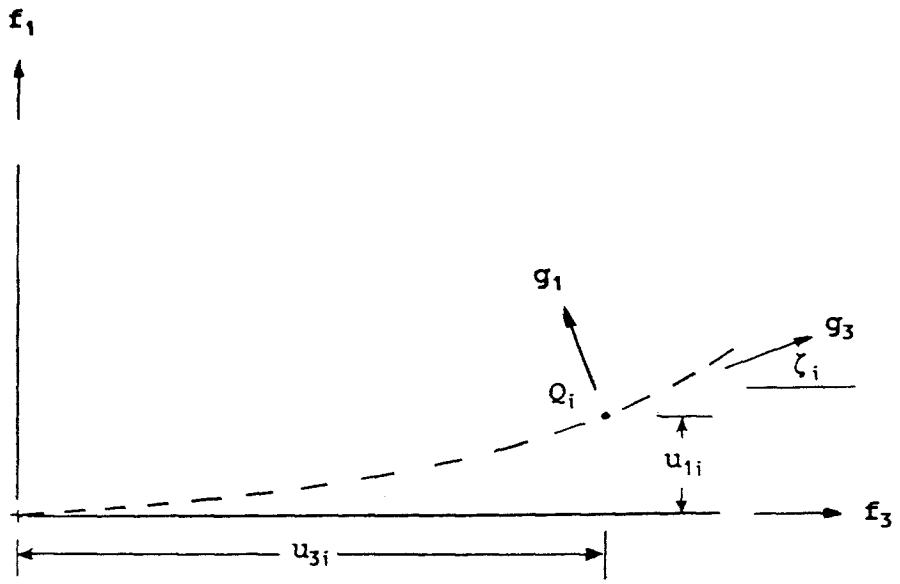

Figure 2.2 Blade Deflection

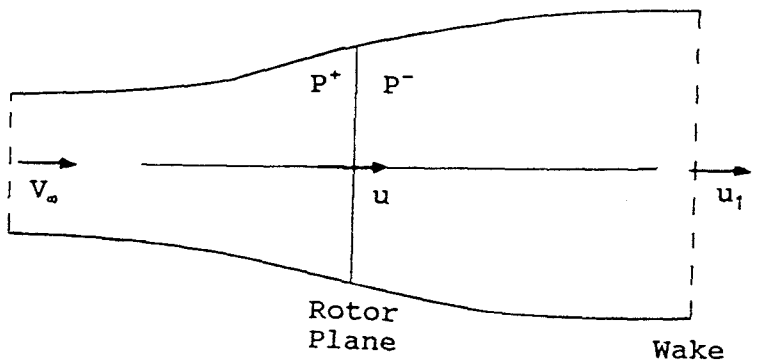

Figure 2.3 One Dimensional Flow Past Rotor

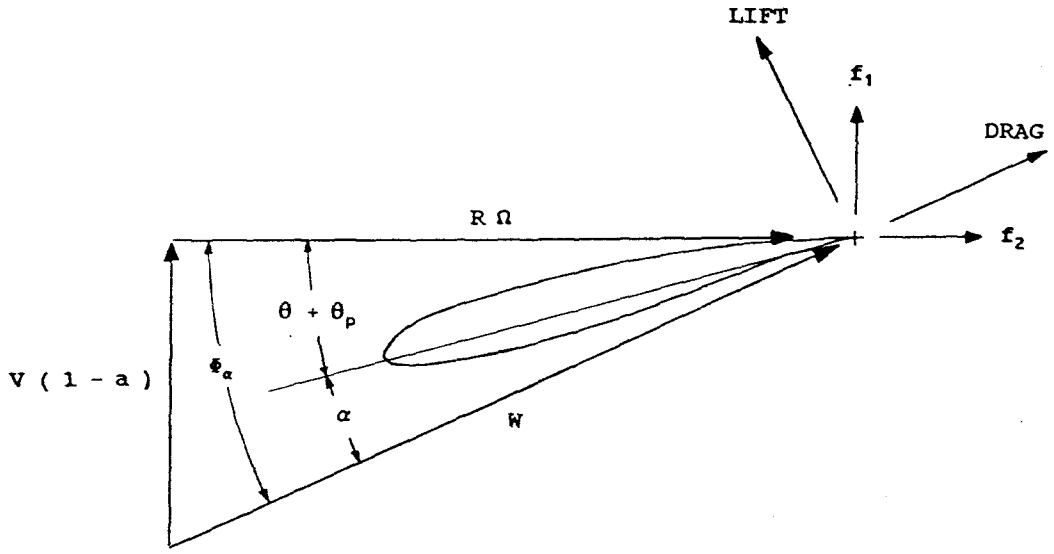

Figure 2.4 Airfoil Velocities

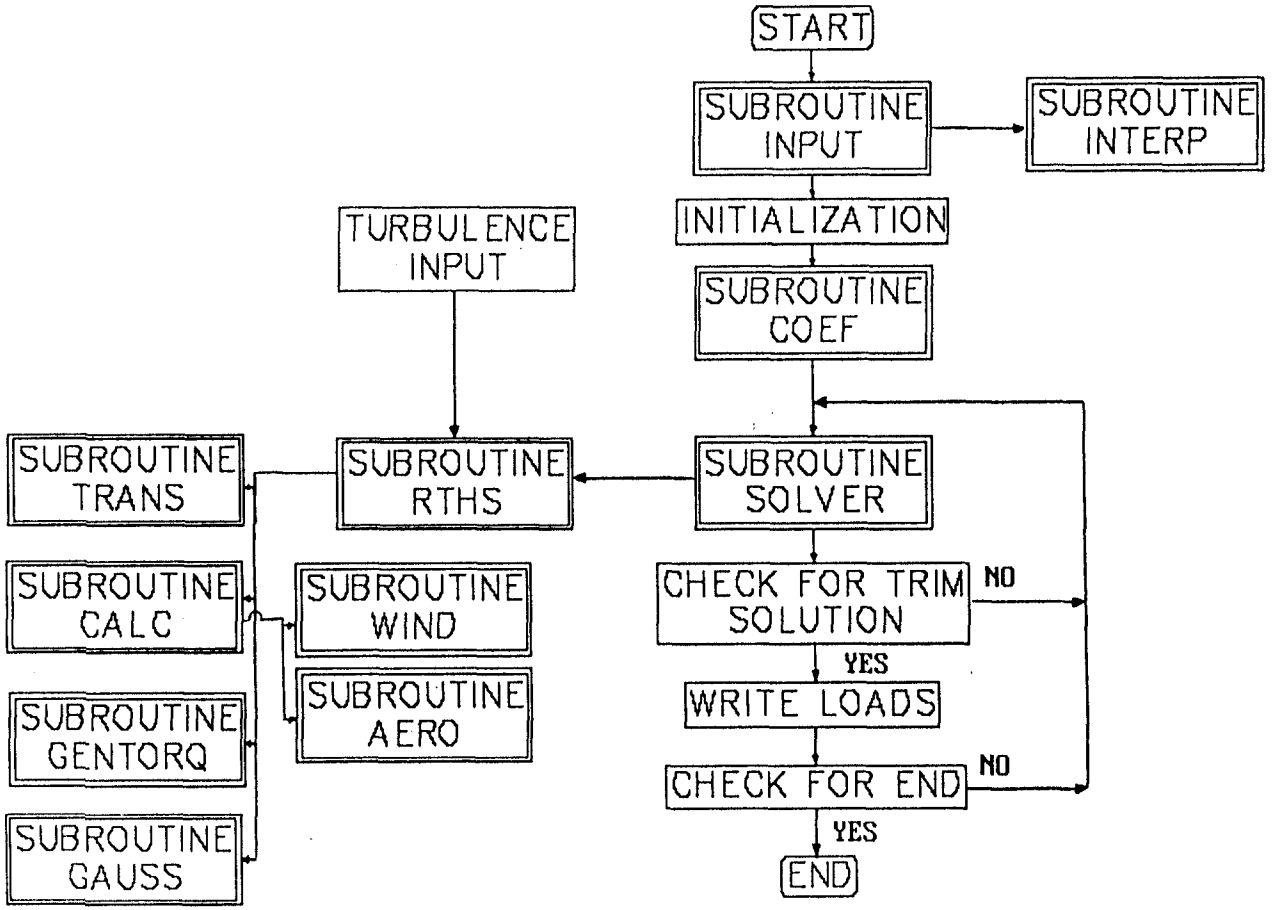

Figure 2.5 Code Flowchart

Chapter 3

Model Validation

Validation of the model was done using two methods. The results from the model were compared to results from simple models where analytical solutions could be found. Additionally, comparisons between model loads predictions and experimental loads were also made. The experimental loads were taken from an ESI-80 wind turbine, which is documented in Appendix A. Loads that were compared were blade root bending moments, rotor torque, and rotor thrust for both mean and cyclic loads.

3.1 Simple Beam

In order to validate the static deflections and natural frequencies of the rotor blades a simple beam, together with linear aerodynamics, was implemented in the code. The blade properties: chord, twist, mass and stiffness were assumed to be constant over the length of the blade. Undersling, delta-3, the elastic bending axis rotation, and coning were set at zero and the variable speed and teeter degrees-of-freedom were turned off. Lift was assumed to vary linearly with the angle of attack, $C_L = 2\pi\sin\alpha$. It was assumed that the induced velocity was constant over the blade given by the relation for the induction factor as

$$a = \frac{c\,\Omega}{2\,V_\infty} \tag{3.1.1}$$

Ignoring the cyclic effect of gravity, a relation for the static tip deflection can be written as

$$q_{static} = \frac{\int_0^R f_n\,\phi\,dr}{\left(\int_0^R \left(\frac{\partial^2\phi}{\partial\bar{r}^2}\right)^2 EI\,d\bar{r}\right) + \int_0^R T\left(\frac{\partial\phi}{\partial\bar{r}}\right)^2 d\bar{r}\right)} \tag{3.1.2}$$

where,

$$T = \int_R^r \Omega^2\,\mu\,\bar{r}\,d\bar{r} \tag{3.1.3}$$

and,

$$f_n = \frac{1}{2}\,\rho\,W^2\,c\,C_L\cos\phi_\alpha \tag{3.1.4}$$

which can be written as,

$$f_n = \rho\,\pi\,c\,r\,\Omega\,V\left(1 - \frac{C\,\Omega}{2\,V}\right) \tag{3.1.5}$$

The numerator can be expressed as,

$$\rho\,\pi\,C\,\Omega\,V\left(1 - \frac{C\,\Omega}{2\,V}\right)\int_0^R r\,\phi_1\,d\,r \tag{3.1.6}$$

Letting the shape function be that from Eq. 2.2.9, with a value of b=0, ρ=1 kg/m^3, c=.25 m, Ω=60 rpm, V=10 m/s, R=10 m, EI=5,000,000 N-m^2, and μ=10 kg/m, gives a static deflection of 0.07747 meters. Implementing the linear lift and the induction factor given in Eq. 3.1.1,

the code gives a static deflection within a half of a percentage point of the analytical value, when the integration step size is one hundredth of the blade length.

Using the same conditions, a relation for the blade flapping natural frequency can be written as

$$w_n^2 = \frac{\int_0^R EI\left(\frac{\partial^2\phi}{\partial r^2}\right)^2 dr + \int_0^R \left(\int_R^r \Omega^2 \mu \bar{r} d\bar{r}\right)\left(\frac{\partial\phi}{\partial r}\right)^2 dr}{\int_0^R \mu\, \phi^2 dr} \qquad (3.1.7)$$

This gives a value for the natural frequency of 4.165 Hertz. The code predicted a value within a half of a percentage point, when the integration step size was set at one hundredth of the blade length.

3.2 Linearized Teeter Motion with Delta-3

A analytical expression can be obtained for the teeter motion through simplification and linearization of the teeter equation (r=3 in section 2.6). The analytical expression can be used for validation of the teeter motion in the code. Letting the blade displacements and motions be zero, setting the rotor speed constant, and ignoring higher order terms, the teeter equation can be written as

$$\sum_{j=1}^{2} \int_{0}^{R} (f_n r\cos\delta_3 - \mu g \sin q_3 \sin q_4 r\cos\delta_3)\,dr$$
$$-\sum_{j=1}^{2} \int_{0}^{R} \mu\,(\ddot{q}_3(\cos\delta_3\, r)^2 + \Omega^2 \sin q_3 \cos q_3 (\cos\delta_3\, r)^2)\,dr = 0 \qquad (3.2.1)$$

where, coning, the elastic bending axis rotation, and the undersling have been set to zero. Linearizing the teeter angle q_3 and assuming the two blade mass distributions are the same, Eq. 3.2.1 can be written as

$$\ddot{q}_3\, I \cos^2\delta_3 + q_3\, I\, \Omega^2 \cos^2\delta_3 = \int_{0}^{R} f_n\, r\, \cos\delta_3\, dr\Big|_{\text{blade 1}} - \int_{0}^{R} f_n\, r\, \cos\delta_3\, dr\Big|_{\text{blade 2}} \qquad (3.2.2)$$

Assuming linear lift, an induced velocity as given in Eq. 3.1.1, and a linear wind shear Eq. 3.1.4 can be written as

$$f_n = \rho\pi c r \Omega (V(1-a)) \mp (\Omega \sin\delta_3\, q_3 + \dot{q}_3 \cos\delta_3)\, r \qquad (3.2.3)$$
$$(\text{- blade 1}) \quad (\text{+ blade2})$$

Combining Eq's. 3.2.2 and 3.2.3 and integrating along the blade gives

$$\ddot{q}_3 + B\cos\delta_3\, \Omega\, \dot{q}_3 + (B \sin\delta_3 + 1)\, \Omega^2\, q_3 = \frac{B\,\Omega}{2\,R}(V_{top} - V_{bottom})\, \sin(\Omega t + \delta_3) \qquad (3.2.4)$$

where,

$$B = \frac{\rho \pi R^4 c \Omega}{2 I \cos^2\delta_3} \tag{3.2.5}$$

with a change of variables

$$\frac{d(\ )}{dt} = \frac{d(\ )}{dq_4}\frac{dq_4}{dt} = \Omega \frac{d(\ )}{dq_4} \tag{3.2.6}$$

Eq. 3.2.4 can be written as

$$q_3'' + B\cos\delta_3\, q_3' + (B\sin\delta_3 + 1) q_3 = \frac{-B(V_{top} - V_{hub})}{R\Omega} \sin(q_4 + \delta_3) \tag{3.2.7}$$

Looking for a steady-state solution of the form

$$q_3 = C_1 \sin q_4 + C_2 \cos q_4 \tag{3.2.8}$$

results in the analytical solution

$$q_3 = \frac{V_{top} - V_{hub}}{R\Omega} \cos(q_4 + 2\delta_3) \tag{3.2.9}$$

Using the same parameters as in section 3.1 and implementing the linear lift, the induction factor from Eq. 3.1.1, and a difference of two meters per second for (V_{top} - V_{hub}), the analytical solution is compared to the code prediction for three values of delta-3 in Figure 3.1. The code accurately predicts the analytical solution for all three cases. Note that the relation for the teeter angle in Eq. 3.2.9 is independent of blade mass and inertia.

3.3 Mean Loads

The ESI-80 was used for comparisons of mean loads. The data for both the mean and cyclic loads were digitized from the report by Musial et al [1]. The measured mean loads were determined by averaging the values in one mile per hour divisions. Data was taken at 5 Hertz from fifteen to thirty minutes. Some data were taken on different days when the atmospheric conditions were different. This can be seen on Figure 3.2, which shows a staircase effect on the bending moment. Atmospheric conditions were not reported. The code was run using only the teeter option. The variable speed and turbulence options were not used.

Figure 3.2 compares code predictions to test root bending moments. The code predictions match well within the standard deviation for the data, which is approximately 5000 N-m, except in the high wind speed portion where the prediction is conservative. The mean root bending moment is the difference between two large moments, the aerodynamic moment and the centrifical moment. In the high wind speed case where aerodynamic stall characteristics are not well known, a small error in either of these would be greatly exaggerated in their difference. Figure 3.3 shows the comparison of rotor thrust and Figure 3.4 compares rotor torque. The code predictions for both of these loads matches the data well.

3.4 Cyclic Loads

The cyclic data used for comparison were recorded at 24 Hertz for five to twenty minute intervals and then averaged versus rotor position. This coarse data sampling rate combined with a rotor averaging increment of fifteen degrees results in a fair amount of uncertainty with the cyclic data. The code was run using the teeter option. The variable speed and turbulence options were not used.

Figure 3.5 compares the teeter angle at 42 miles per hour. The code was run with a 3.6 degree interval. The prediction lags the data by approximately thirty degrees and underpredicts the amplitude. The ESI-80 has teeter dampers when teeter amplitudes of two degrees are reached but that is not a concern for this case as neither the data nor the predictions exceed that value. Figure 3.6 compares the root bending moment at 22 miles per hour. The prediction follows the general trend of the data, however the prediction shows more detail in the blade flapping response, especially in the tower shadow region where the blade passes through the wind deficit and then springs out of it. This occurs approximately at a rotor position of ninety degrees. The blade natural frequency of 2.5 Hertz also can be seen in this Figure. Figure 3.7 shows the comparison of cyclic rotor thrust. The effect of the blade entering the tower shadow can be seen at 90 degrees for blade one and 270 for blade two. The prediction appears to

have a phase lag of 90 degrees. Thrust measurements were taken at the base of ESI-80 support tower, so it is possible that tower motion caused this anomaly. Figure 3.8 shows cyclic rotor torque. The prediction shows the same trend with exaggerated tower shadow effects. The larger amplitude for both the thrust and torque data suggests a yaw error. The yaw errors were unreported for these cases.

3.6 References

1. Musial, W.D., Butterfield, C.P., Handman, D., "ESI-80/EPRI Test Program," EPRI RP1996-14, December 1985.

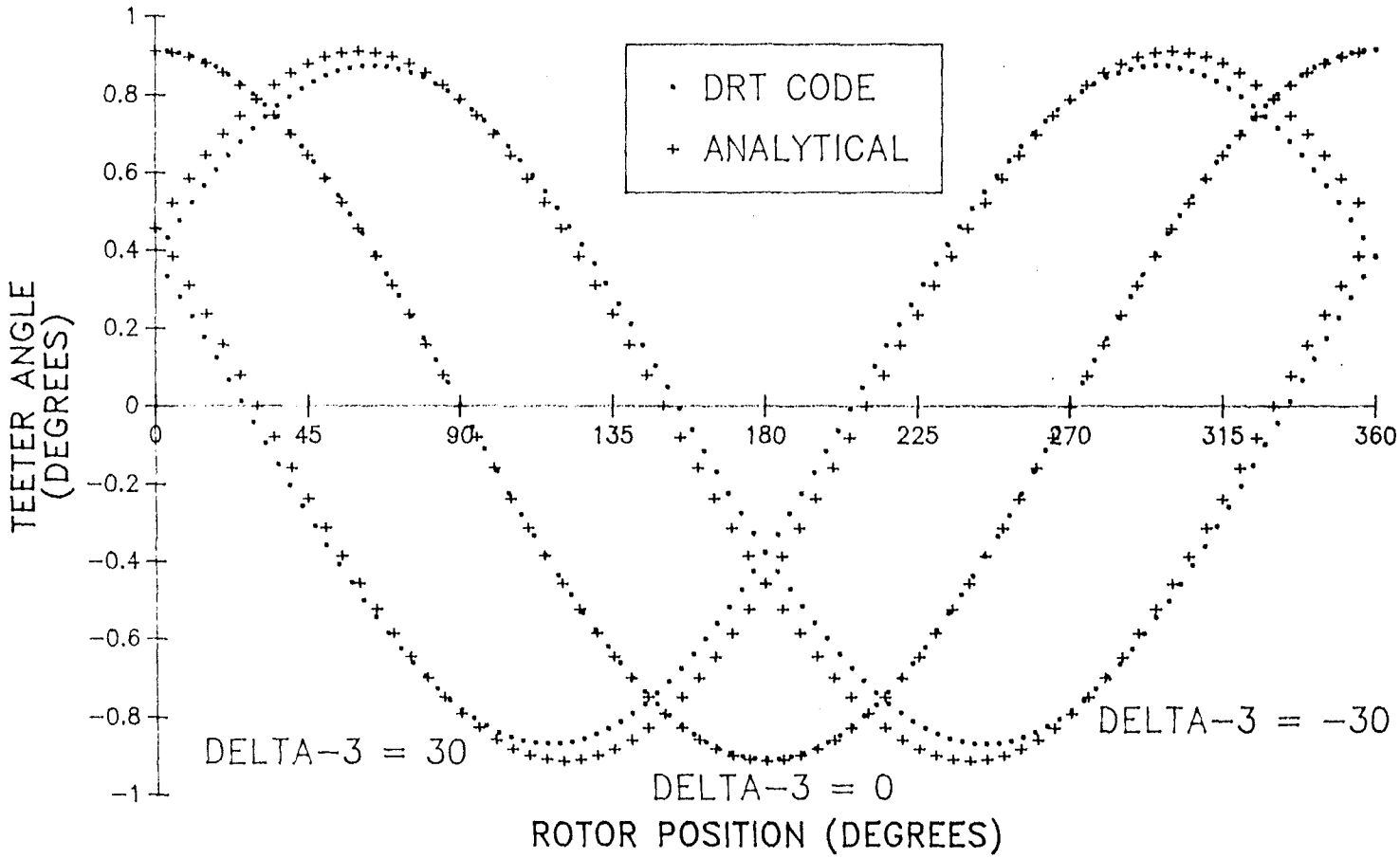

Figure 3.1 Comparison of Analytical and Code Teeter Angle

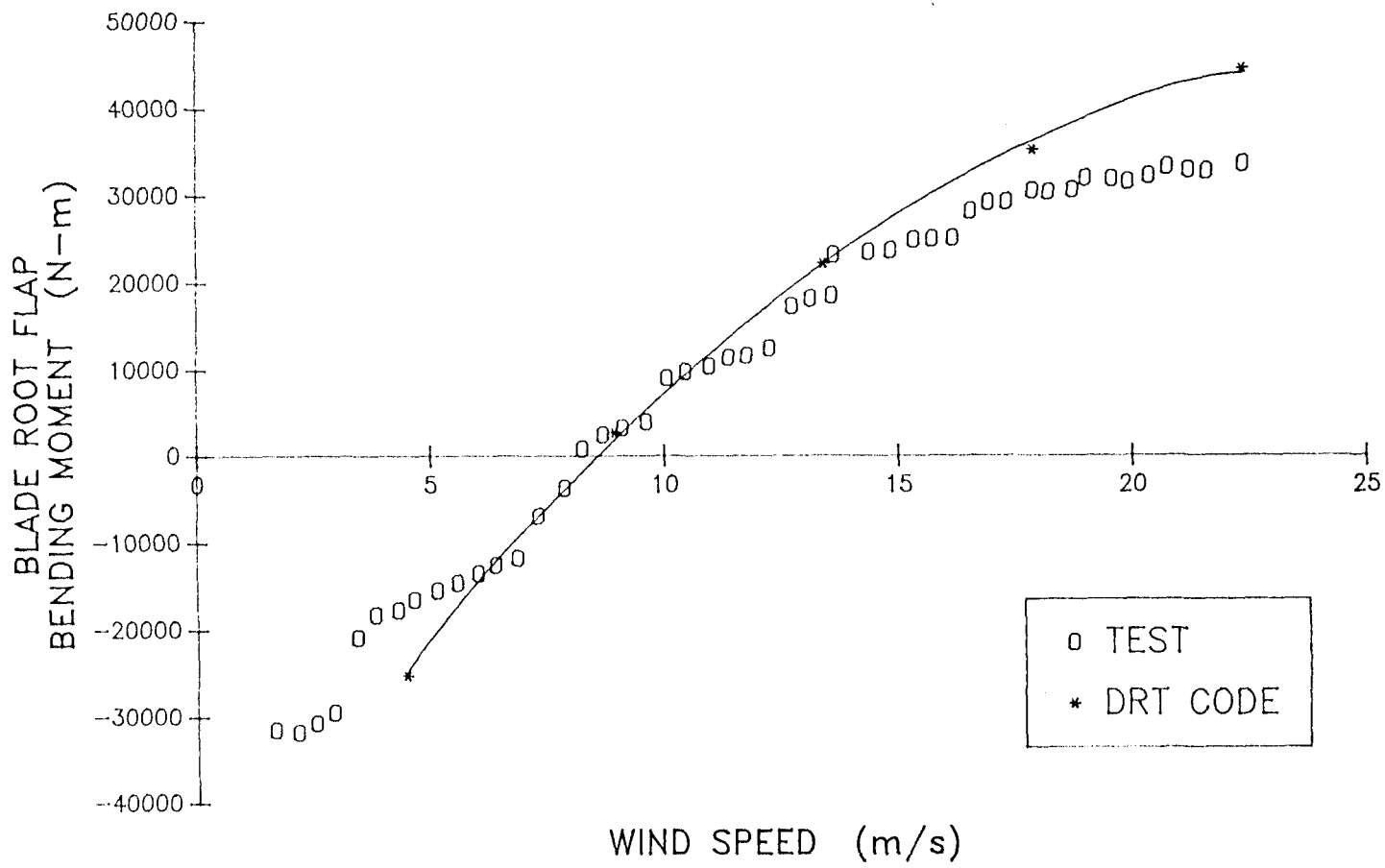

Figure 3.2 Comparison of Mean Blade Root Bending Moments

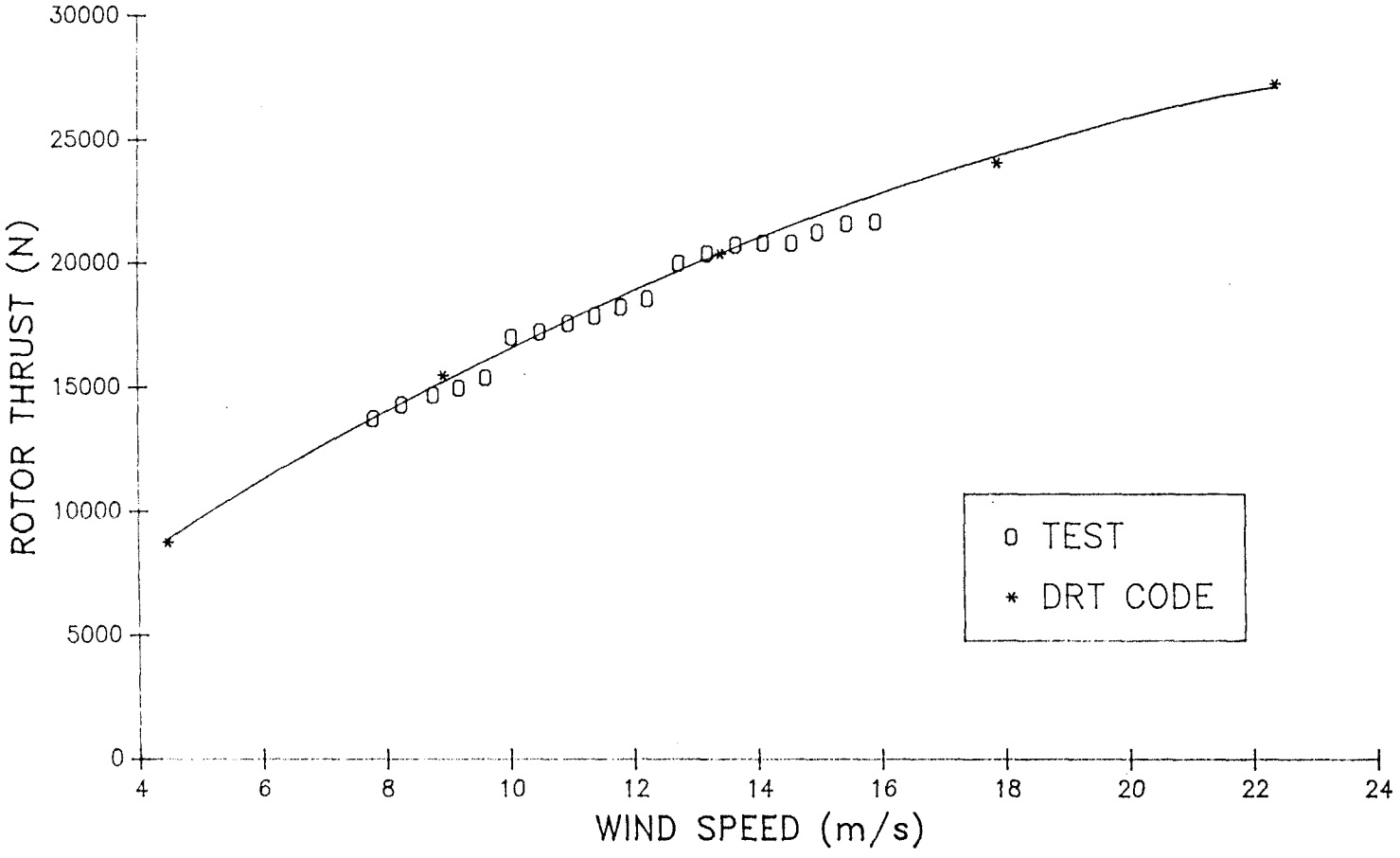

Figure 3.3 Comparison of Mean Rotor Thrusts

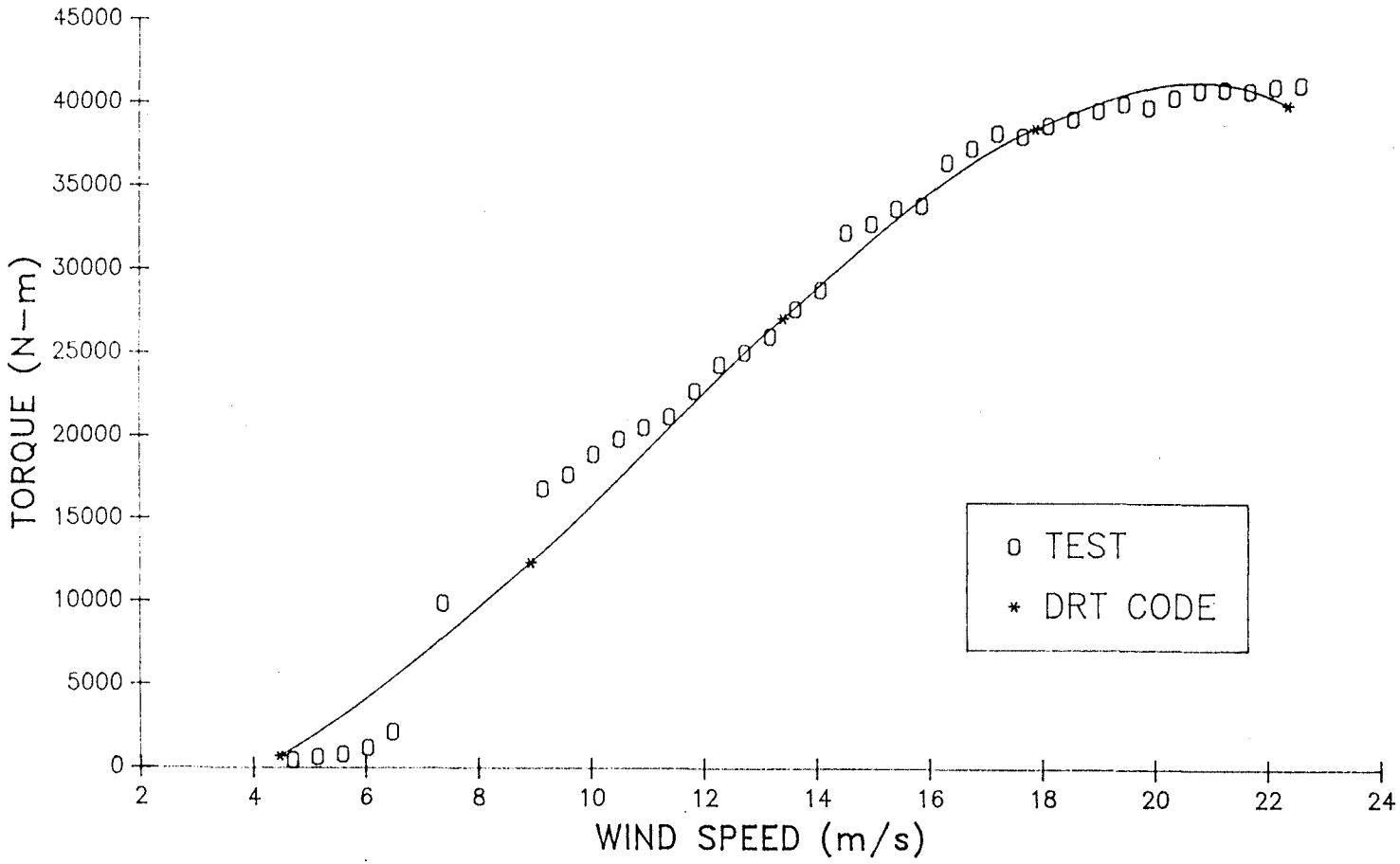

Figure 3.4 Comparison of Mean Rotor Torques

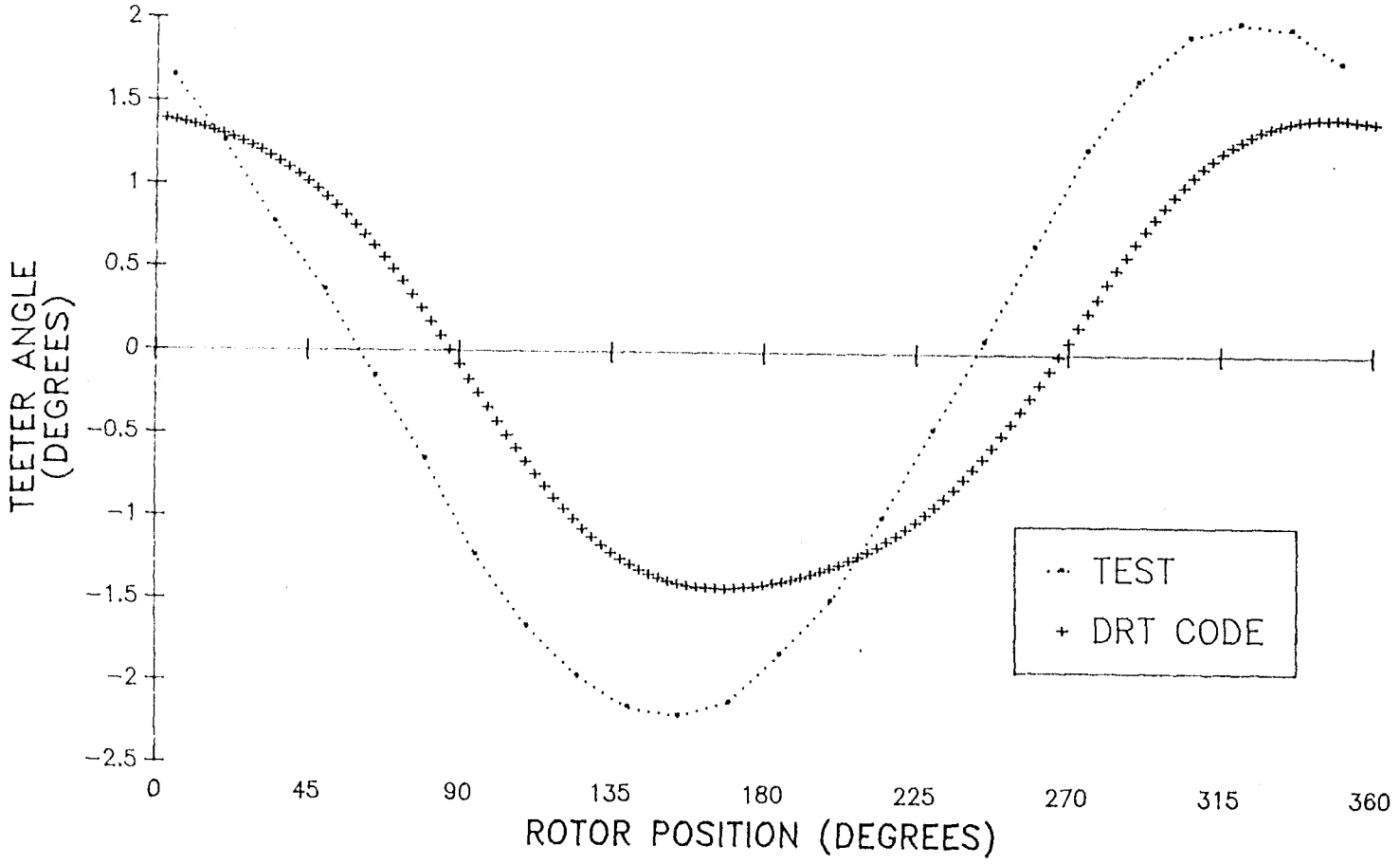

Figure 3.5 Comparison of Teeter Angle at 18.78 m/s

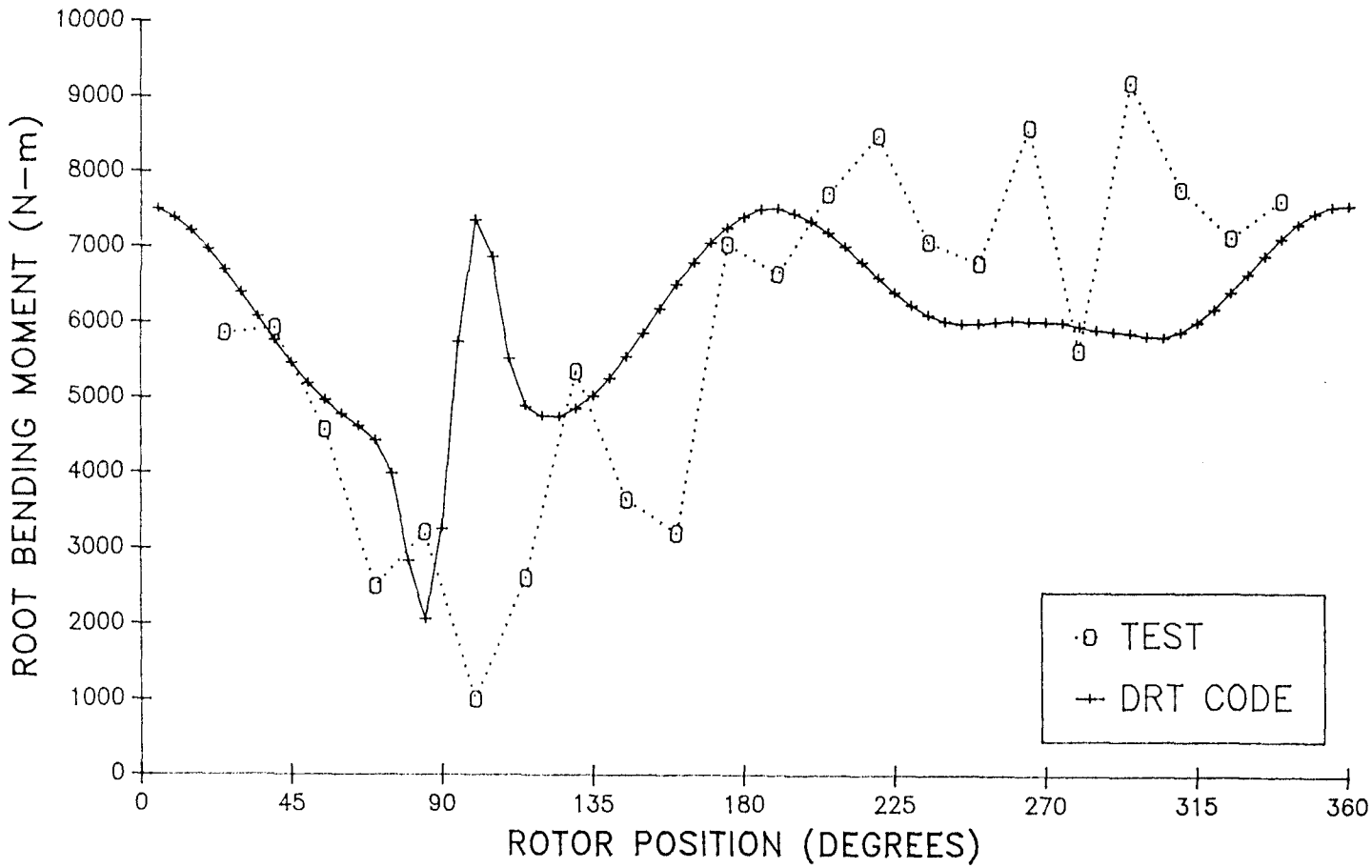

Figure 3.6 Comparison of Cyclic Blade Root Bending Moment at 9.83 m/s

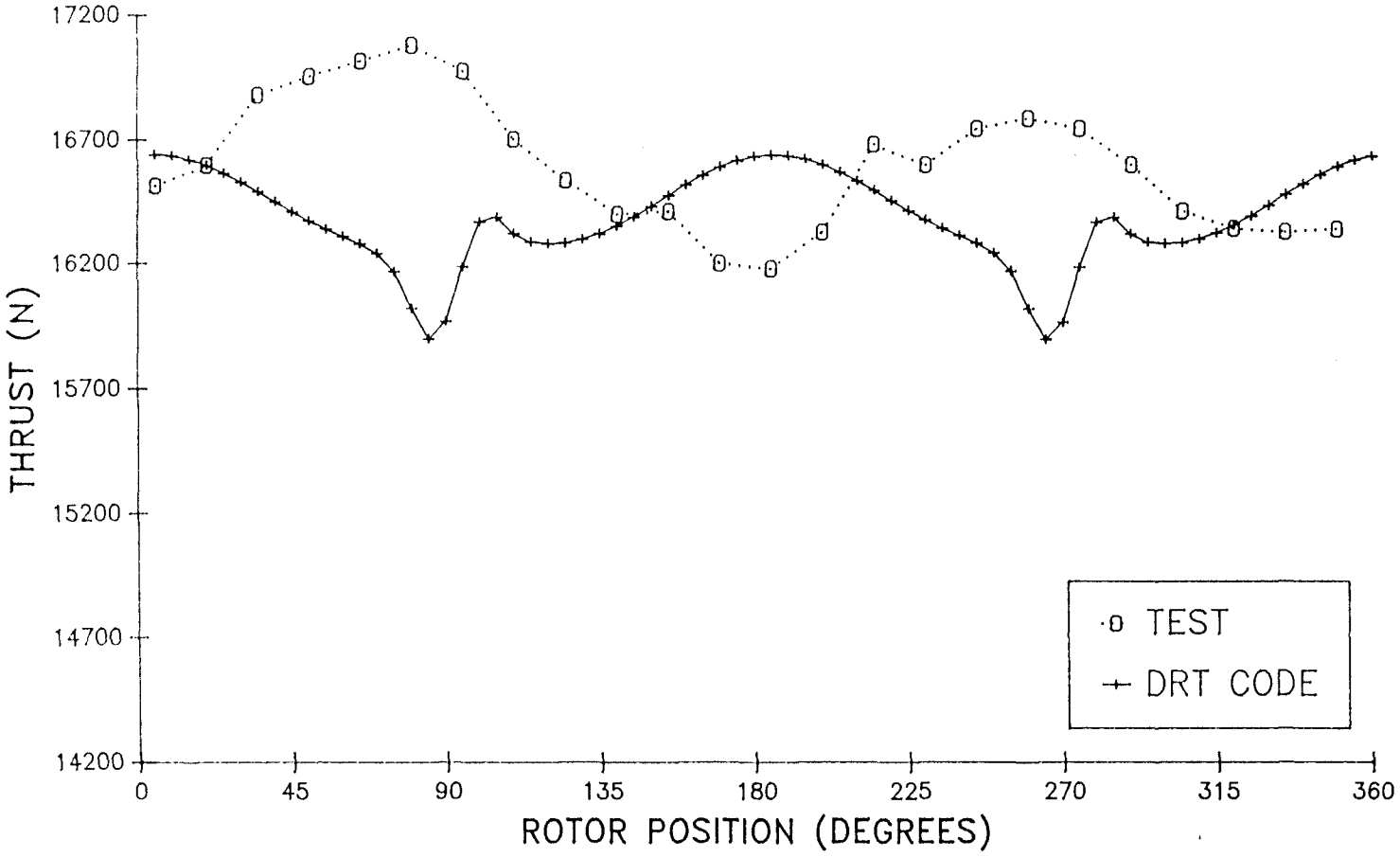

Figure 3.7 Comparison of Cyclic Rotor Thrust at 9.83 m/s

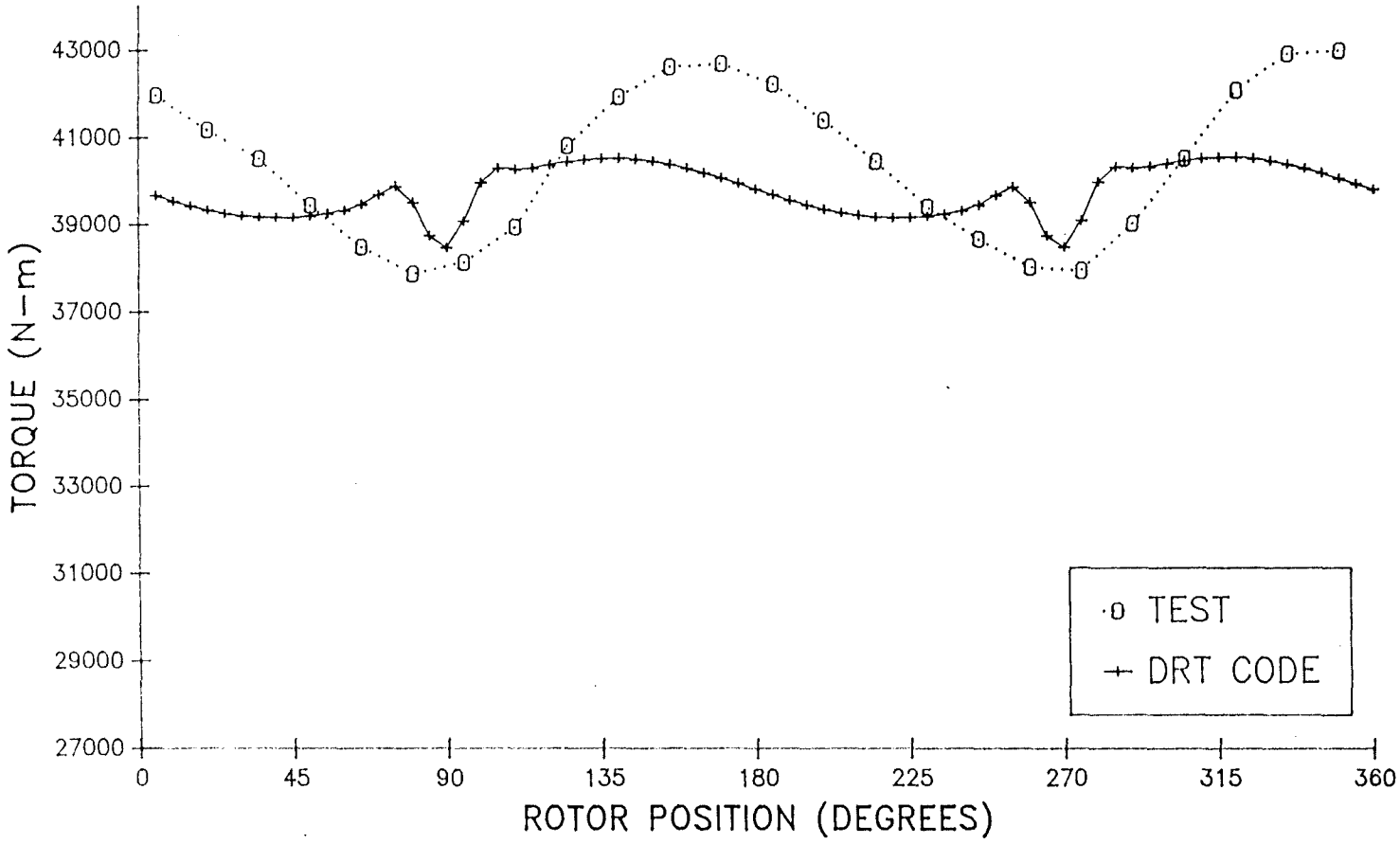

Figure 3.8 Comparison of Cyclic Rotor Torque at 19.67 m/s

Chapter 4

Turbulence Simulation

There are many multi-bladed rigid-hub horizontal axis wind turbines that can be analyzed by examining the loads on only one blade. Rotor loads can be determined by superimposing the loads from the one blade in the place of the others with an appropriate phase shift. If the rotor diameter of the wind turbine is smaller than the longitudinal turbulence integral length, the loads due to turbulent wind can be analyzed using the turbulence simulation at one point for the entire blade. For rotors perpendicular to the mean flow only the longitudinal turbulence component is important. Wright [1] and Hartin [2] chose an arbitrary location on the blade to determine the rotational time series. This point is then used as the turbulent wind input along the entire blade.

Turbulence simulation for HAWT analysis codes which model only one blade on a rigid hub has been well studied. A comparison of wind turbulence simulation models for analysis of stochastic loads was made by Walker et al [3]. Rosenbrock [4] developed an autocorrelation for a point rotating in turbulent wind. Hohenemser et al [5] used this relation to determine the frequency response function for a linearized teeter equation for a helicopter rotor. A number of researchers [6-8] have used the method of Shinozuka [9] together with the rotational autocorrelation

function to create models that create a rotational time series. Holley et al [10] created a rotational turbulence simulation model based on a harmonic balance of the rotational autocorrelation function.

When more complicated rotors are analyzed these codes cannot be used. The code developed by Holley will generate multi-blade multi-station turbulence, but it is only valid up to twice the rotor rotational frequency. This is limiting, considering that most blade flapwise natural frequencies are above that. The rotational autocorrelation codes generate only one point on one blade. These codes cannot be used with a teetered rotor where coherent turbulence is needed because of blade interaction through the teeter degree-of-freedom. Nor will it be valid for turbines where the rotor diameter is of the same magnitude as the longitudinal turbulence integral scale, and the turbulence over the entire blade must be modeled at more than one point. These turbulence codes are based on constant rotor speed so they cannot be used for variable speed analysis.

A method for simulating a full field of turbulence was developed at Sandia National Laboratories by Veers [11]. This model is also based on the Shinozuka method. It allows the user to simulate turbulence at many points in a field preserving the power spectral densities at each point, and relating all locations through a coherence function. A method similar to this one could possibly be developed for

the rotational autocorrelation for a number of moving points, but this code would still only work for constant rotor speed. Veers [12] developed a special version of his code to handle HAWTS running at fixed rotor speed. For the case where variable speed operation is being studied the original code is needed. The Veers model instead of using constant rotor speed uses a constant time step. This results in interpolation for variable speed operation, but if the grid of turbulence points is tight enough the statistical qualities of the turbulence can be preserved. The limiting factor for the Veers full field code is the large main memory requirements. The size of the compiled code increases approximately by the square of the number of points being modeled. A desktop PC with a standard 640 kilobytes of memory can simulate only one point on one blade. The memory required to generate four points on a blade at a 3.6 degree azimuthal spacing for 1024 points exceeds the normal 2^{20} byte standard FORTRAN 77 array size limitation.

The objective of this chapter is to optimize the rotor loads induced by turbulence from a single point model on two blades with a multi-blade multi-station turbulence model using the DRT code. Rainflow cyclic counting and power spectra of the flapwise root bending moments will be used for the optimization. Rainflow cycle counting determines the number of cycles as a function of their magnitude about the mean value. A cosine wave would have

one cycle with a magnitude of twice the amplitude of the cosine wave.

4.1 The Turbulence Simulation Code

A brief discussion of the full field turbulence simulation model developed by Veers follows. A full field of turbulent wind can be generated on a grid of points perpendicular to the mean wind direction. Well known relations for the power spectral densities [13] (psd) can be used to define the second order statistics of the wind speed at each point. Each point is related to the other points through the cross spectral density (csd). The csd is related to the psd through the expression:

$$|S_{ij}|^2 = \gamma_{ij}^2 S_{ii} S_{jj} \qquad (4.1.1)$$

where,

γ_{ij}^2 = coherence function
S_{ij} = csd between points i and j
S_{ii} = psd at point i

If the csd are approximated as real functions, a spectral matrix [**S**] can be formed using a coherence function suggested by Frost [13].

$$\gamma_{ij}^2 = \exp\left(\frac{-aw\Delta r}{V}\right) \qquad (4.1.2)$$

where,

a = decay coefficient
w = frequency
Δr = distance between points i and j
V = mean wind speed

The spectral matrix can be converted into a vector of time series realizations, by the equation:

$$\{\mathbf{V}\} = \mathcal{F}^{-1}\left([\mathbf{H}][\mathbf{X}]\right)\{\mathbf{1}\} \qquad (4.1.3)$$

where,

$\{\mathbf{V}\}$ = vector of time series relations

$[\mathbf{X}]$ = diagonal matrix of independent white noise Gaussian signals with unit variance. Gives a random phase at each frequency to each column of $[\mathbf{H}]$.

$\{\mathbf{1}\}$ = a column of ones. This is used to sum the rows of the inverse Fourier Transform of $[\mathbf{H}][\mathbf{X}]$.

$[\mathbf{H}]$ = matrix of transformation functions relating white noise to the correlated spectra through the relation:

$$[\mathbf{H}]^*[\mathbf{H}]^T = [\mathbf{S}] \qquad (4.1.4)$$

The matrix $[\mathbf{H}]$ is determined using "Cholesky decomposition" of the matrix $[\mathbf{S}]$. This requires the assumption that the matrix $[\mathbf{H}]$ is lower diagonal. The

vector {**V**} has zero mean, so the mean wind and wind shear must be added. [**S**], [**H**], and [**X**] are N by N matrices, for N input points. Each element in the matrices must be defined at M/2 discrete frequencies. The number M is equivalent to the number of time series values required. The size of the memory required by the program is proportional to N by N by M. Recent work by Winkelaar [14] suggests a more efficient method for the decomposition of the matrix [**H**]. Veer's constant rotor speed version shifts the frequencies by a phase angle equal to the product of the rotor angular speed and the time of the blade passage at that point. This reduces the memory requirement by the ratio of the number of points per revolution to the number of blades simulated.

Assuming the turbulence components in the lateral, vertical, and longitudinal directions are uncorrelated, the procedure above can be repeated to generate turbulence in the lateral and vertical directions using appropriate psd and csd.

4.2 Optimization

The first step for optimizing a two-bladed single rotating point turbulence model was to determine the computational boundaries in the full field turbulence model. One bound already mentioned is the 2^{20} byte FORTRAN

array size limitation. The author had access, through the National Center for Supercomputer Applications, to a Cray X-MP computer. The Cray computer had 32 megawords of main memory allocated to each user. This allowed three blade locations (four including the hub), ninety blade locations per revolution, and a 2048 point time series length. An additional limitation to the Cray was an one megabyte file size. The above mentioned case created an intermediary file that exceeded 500 megabytes. This barrier reduced the size of the turbulence file that could be created to PC proportions. It was then decided to use Veer's constant rotor speed (CRS) HAWT version to optimize the single point model. Once the optimization was achieved, the full field model could be used for variable speed analysis. The Cray was abandoned and the CRS Code was run on a 386/33 computer using a virtual memory FORTRAN compiler. Computer virtual memory allowed three blade stations, 128 blade locations per revolution and 2048 time series points. Total compiled memory was 10.8 megabytes. The three blade stations were chosen by dividing the rotor swept area into three equal areas and letting the radial location that divided these areas in half be the radial location used in the turbulence simulation. Figure 4.1 shows the three areas and the corresponding blade station locations.

The ESI-80 was the test turbine used for this analysis. The CRS Code generates a file containing turbulence values for both blades with three stations each.

The CRS Code does not generate a hub value. The Kaimal [15] Spectrum was used as the fixed point input spectrum (S_{ii}). A 2048 point time series with 128 blade locations and a rotor speed of 60 revolutions per minute corresponds to 16 seconds real time. This is a long enough sample to allow analysis of the spectral energy around the one period frequency component. Figure 4.2 shows the typical power spectral density of wind seen by an outer blade station. Notice the energy spikes at multiples of the fundamental frequency, which is the frequency at which the rotor makes one revolution. The ESI-80 has a rotor speed of 60 rpm which gives a fundamental frequency of one Hertz. These energy spikes result from the blades passing through the same turbulent eddies once per revolution. Bending moments will show similar spectral characteristics except more energy will be prevalent at system natural frequencies. The ESI-80 has a blade flapwise natural frequency at 2.51 Hertz. This value includes centrifugal stiffening.

The first choice for a single blade point is the radius that divides the rotor swept area in two. This occurs at the 70.7 percent radius location. A second choice can be made by finding the radial centroid of the aerodynamic bending moment load assuming it varies with the radius squared. This value is the 75 percent radial station. The CRS Code was run for these two single-point cases and the three-point case with parameters of 22.352 meters per second (50 mph) and a turbulence intensity of 15

percent. The three output files from the CRS Code were used as inputs to the DRT code. Figure 4.3 shows the comparison of the power spectral density of the root bending moment for the multi-blade station simulation against the two single-point simulations. The same random number seed was used for all three cases. The 70.7 percent and 75 percent cases have nearly identical results. Notice the strong spectral spike at three Hertz caused by turbulence induced excitation of the blade natural frequency. All three cases predict an equivalent amount of spectral energy at this point. For rigid-hub rotors the one period component usually has the largest spectral spike, but the teetering mechanism of the ESI-80 transfers one period flapwise bending moment to one period teeter motion. The strong peak at two Hertz is due to turbulence and the blades passing through the tower shadow. The two single-point simulations have a lower standard deviation (area under spectra) as that of the three-point simulation, approximately 18.5 and 17 percent lower for the 70.7 and 75 percent radial stations, respectively. This difference in area occurs mostly in the lower frequency range under one Hertz. Table 4.1 shows the rainflow cycle counts for the same three cases. Again the two single-point simulations have nearly identical results. The single-point simulations under-predict the high cycles, above 60,000 N-m. This concurs with the lower energy values in the low frequency range of the power spectra, since the low

frequency, high energy component of the spectra is responsible for the large cycles. The CRS Code was run again using a 80 percent radius value and the same random seed. Figure 4.4 shows this simulation compared with the three-point simulation for the power spectral density of the root bending moment. The 80 percent radius simulation has the same characteristics as those of the lessor radial stations, except the standard deviation is 14 percent lower than that of the three-point simulation. The rainflow comparison in Table 4.2 has some slightly higher cycles, but follows the same trend. Midrange cycles are more numerous with the 80 percent radius than the other two single-point simulations and the three-point simulation. It appears, the three-point simulation averages the turbulent values over the blade transferring energy from high to low frequencies.

Figure 4.5 shows the power spectral density for a 15.65 m/s (35 mph) case with 15 percent turbulence. Three simulations are compared; a three-point simulation, and two single-point simulations at radii of 75 and 80 percent. The same random number seed was used for all three. The trends for the three cases are similar to that of the 50 mph cases. The two single-point cases are nearly identical, and strong spectral spikes are seen at the blade natural frequency, the teeter frequency, and twice the teeter frequency, in descending order of magnitude. As in

the 50 mph cases, the spectral energies drop drastically after the blade natural frequency is encountered, over two decades. The standard deviations for the two single-point simulations are 10 and 6 percent lower that the three-point simulation for the 75 and 80 percent radial locations, respectively. Table 4.3 shows the rainflow cycle counts for the same case. Again, the three-point simulation has a few more high cycle counts, and the two-point simulations have more low cycle counts. The 80 percent case is more conservative with more high cycle counts than the 75 percent case.

Figure 4.6 and Table 4.4 compare the power spectral density and the rainflow cycle counts for three 8.94 (20 mph) with a turbulent intensity of 15 percent. The cases are the same as the previous wind speed case; a three-point and two single-point simulations. The trend is similar except the standard deviations of the root bending moment of the two single-point simulations is 11 and 14 percent higher than the three point simulation for the 75 and 80 percent radial stations. The comparison of the rainflow cycle counts is much closer at this wind speed case, with approximately the same number of high and low cycle counts.

The final windspeed case is shown in Figure 4.7 and Table 4.5. A three-point and an 80 percent radius station single point simulation are shown for a 35 mph case with a

turbulence intensity of 25 percent. The comparison is similar to the case with the same wind value and lessor turbulence intensity. The single-point simulations standard deviation is 5 percent lower than the three-point simulation, unchanged from the lower turbulence intensity case. The rainflow cycle counts are nearly identical in the low cycle end, however the single-point simulation has fewer counts at the high cycle end as seen in all previous cases.

4.3 Conclusions

The 80 percent radial station is the optimal point for single-point turbulence simulation when compared to three-point simulation. The corresponding spectral characteristics of the root bending moment is well preserved, although the spectral area (standard deviation) is high for low wind speeds and increasingly lower for higher windspeeds. This shift of the spectral area is a function of mean wind only, no dependence on the turbulence level was noted. The rainflow cycle counts are shifted from high to low cycles, when compared to three-point simulations. This effect increases proportionally with increased wind speed. The three-point simulation averages the turbulent values over the blade transferring energy from high to low frequencies (or low to high cycles, respectively). When using a 80 percent radius simulation

the predictions will be nonconservative in the low frequency range. For estimation of fatigue lifetimes, it is recommended that the rainflow cycle increments of root bending moment be multiplied by a factor of 1.2. This factor will better represent the high, most damaging, cycles. This factor will tend to overpredict low cycles for cases with low wind speeds and or high turbulence.

This optimization was found using an idealized fixed point spectrum. Actual wind turbine sites may have complicated terrains that change the spectral slope and shape. It is not known how a radically different spectrum will change the optimal value of the 80 percent radius.

4.4 References

1. Wright, A.D., Weber, T.L., Thresher, R.W., Butterfield, C.P., "Prediction of Stochastic Loads for Three-Bladed, Rigid Hub Rotors," Ninth ASME Wind Energy Symposium, New Orleans, LA, Jan. 14-18, 1990.

2. Hartin, J.R., "Evaluation of Prediction Methodology for Blade Loads on a Horizontal Axis Wind Turbine, Ninth ASME WES, New Orleans, LA, Jan. 14-18, 1990.

3. Walker, S.N., Weber, T.L., Wilson, R.E., " A Comparison of Wind Turbulence Simulation Models for Stochastic Loads Analysis for HAWT," SERI STR-217-3463, June, 1989.

4. Rosenbrock, H.H., "Vibration and Stability Problems in Large Wind Turbines Having Hinged Blades," The Electric Research Association, TR C/T 113, 1955.

5. Hohenemser, K.H., Gaonkar, G.H., "Flapping Response of Lifting Rotor Blades to Atmospheric Turbulence," J. AIAA, Vol. 6, No. 6, 1969.

6. Anderson, M.B., "The Interaction of Turbulence with a HAWT," Proc. of the British Wind Energy Assoc., March 24-26, 1982, Cavendish Lab, University of Cambridge.

7. Connell, J.R., "The Spectrum of Wind Speed Fluctuations Encountered by a Rotating Blade of a WEC," PNL 4083, Richland, WA, 1981.

8. Sundar, R.M., Sullivan, J.P., "Performance of Wind Turbines in a Turbulent Atmosphere," Proc. of Wind Dynamics, NASA CP 2185, Purdue University, 1981.

9. Shinozuka, M., "Simulation of Multi-Variate and Multidimensional Random Processes," J. of the Acoustical Society of America, Vol. 9, No. 1, part 2, 1971.

10. Holley, W.E., "An atmospheric Turbulence Model for Wind Turbine Dynamic Simulation: Its Verification and Implementation into the FLAP Code," Oregon State University, Unpublished OSU report, 1982.

11. Veers, P.S., "Modeling Stochastic Wind Loads on Vertical Axis Wind Turbines," SAND83-1909, Sandia National Lab., Sept, 1984.

12. Veers, P.S., "Three-Dimensional Wind Simulation," SAND88-0152, Sandia National Lab., March, 1988.

13. Frost, W., Long, D.H., Turner, R.E., "Engineering Handbook on the Atmospheric Environment Guideline for Use in Wind Turbine Generator Development," NASA TP-1359, Dec., 1979.

14. Winkelaar, D., "Fast Three-Dimensional Wind Simulation and the Prediction of Stochastic Blade Loads," Tenth ASME WES, Houston, TX, Jan. 20-23, 1991.

15. Kaimal, J.C., Wyngaard, J.C., Izumi, Y., Cole, O.R., "Spectral Characteristics of Surface-Layer Turbulence," Quart. J. of the Royal Meteorological Society, Vol. 113, No. 7, 1987.

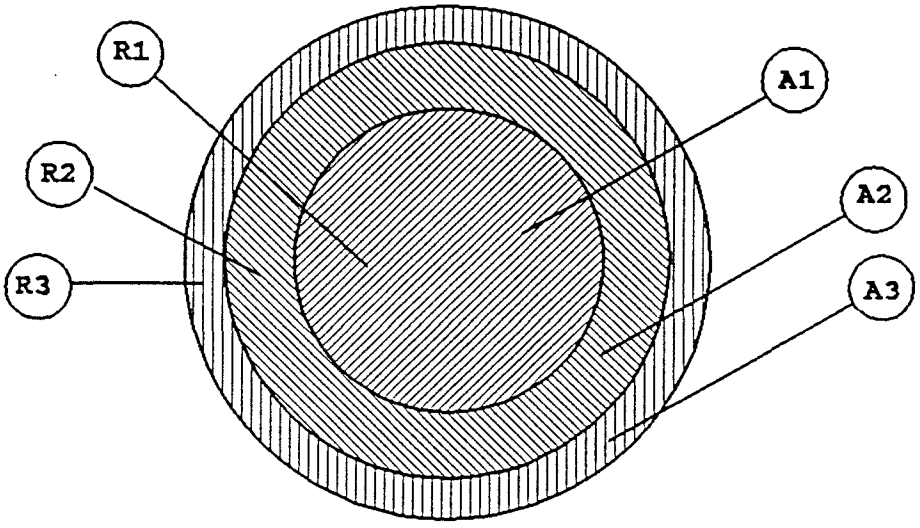

Figure 4.1 Rotor Swept Equal Areas and Radial Stations

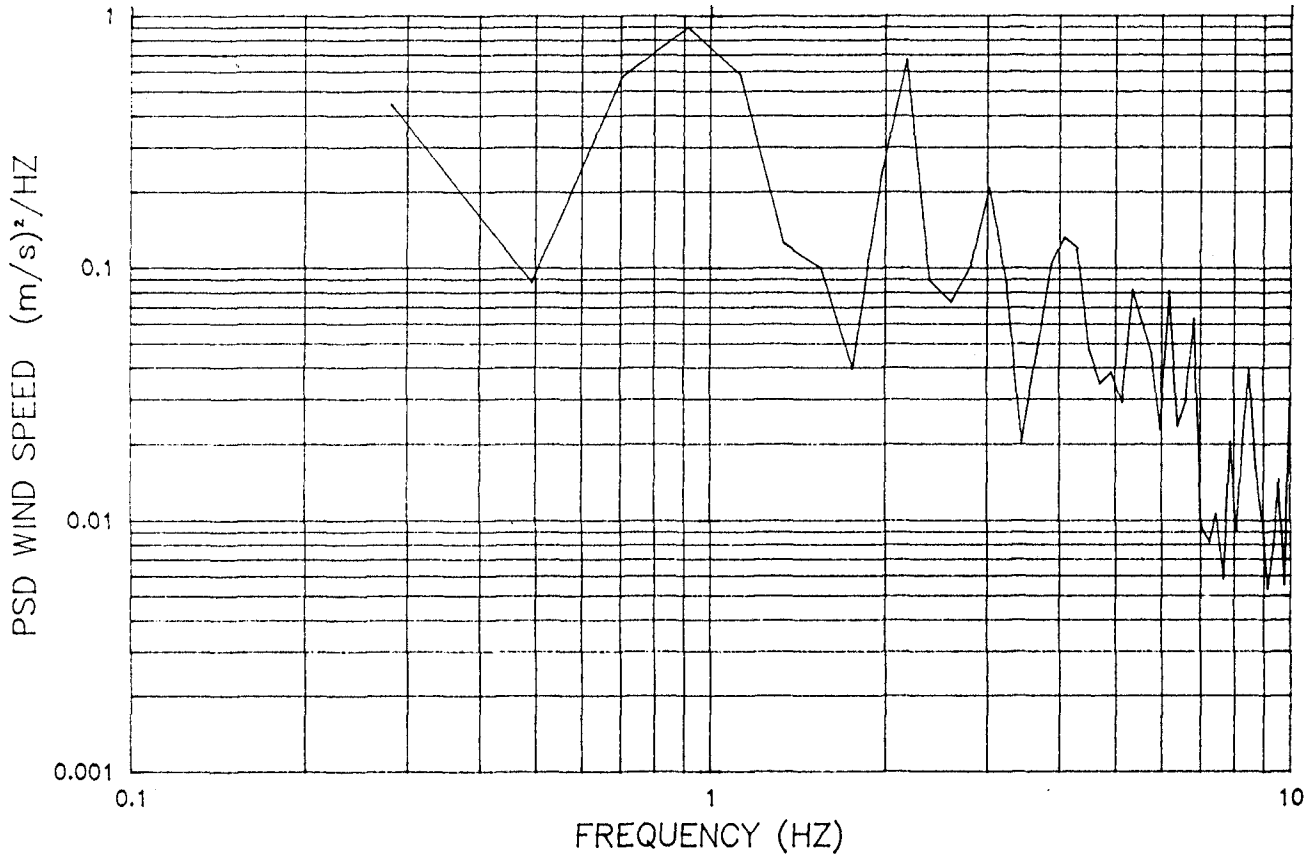

Figure 4.2 Power Spectral Density of Rotationally Sampled Wind

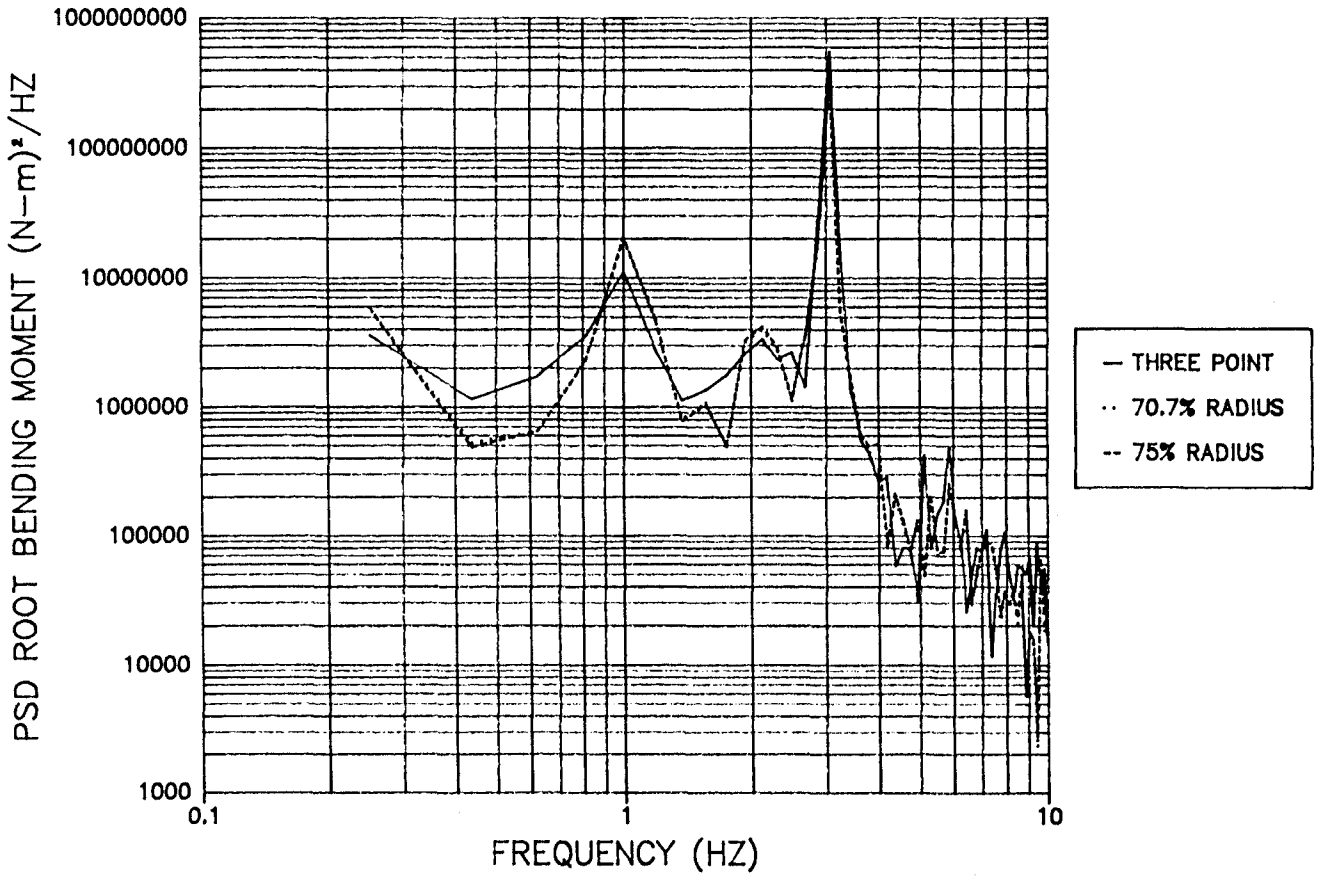

Figure 4.3 Comparison of Power Spectral Densities of Blade Root Bending Moment for a 22.353 m/s Wind with 15% Turbulence

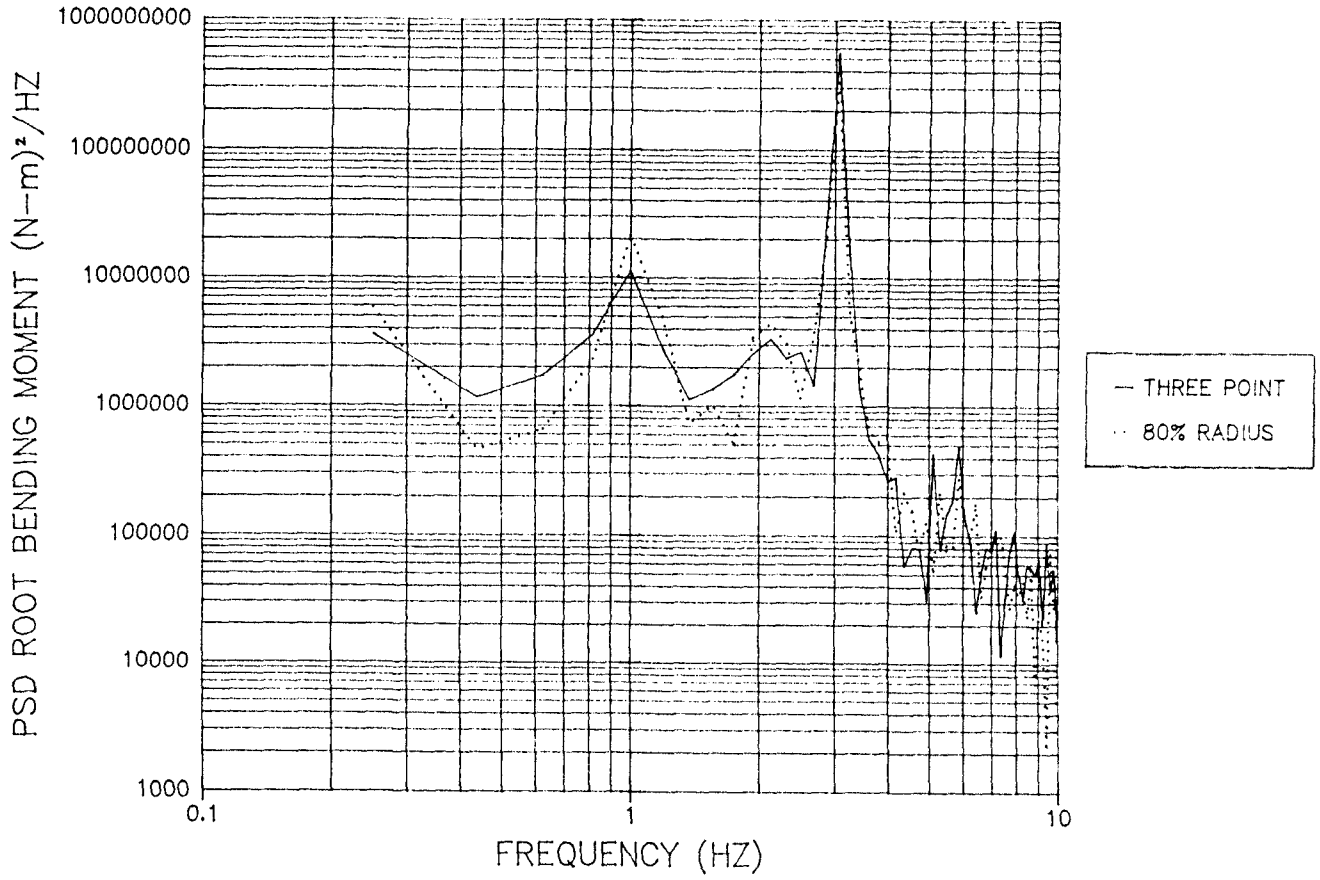

Figure 4.4 Comparison of Power Spectral Densities of Blade Root Bending Moment for a 22.353 m/s Wind with 15% Turbulence

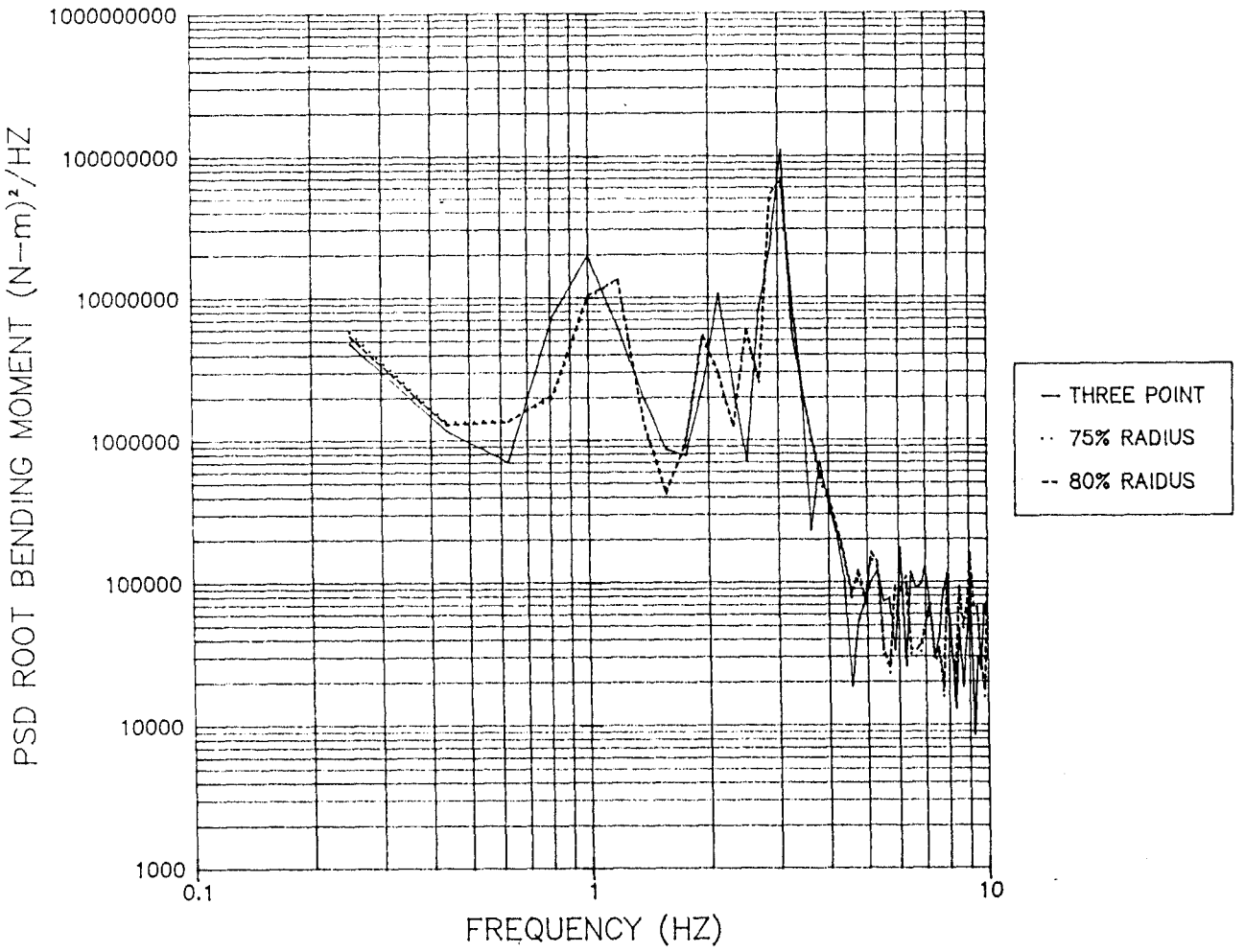

Figure 4.5 Comparison of Power Spectral Densities of Blade Root Bending Moment for a 15.65 m/s Wind with 15% Turbulence

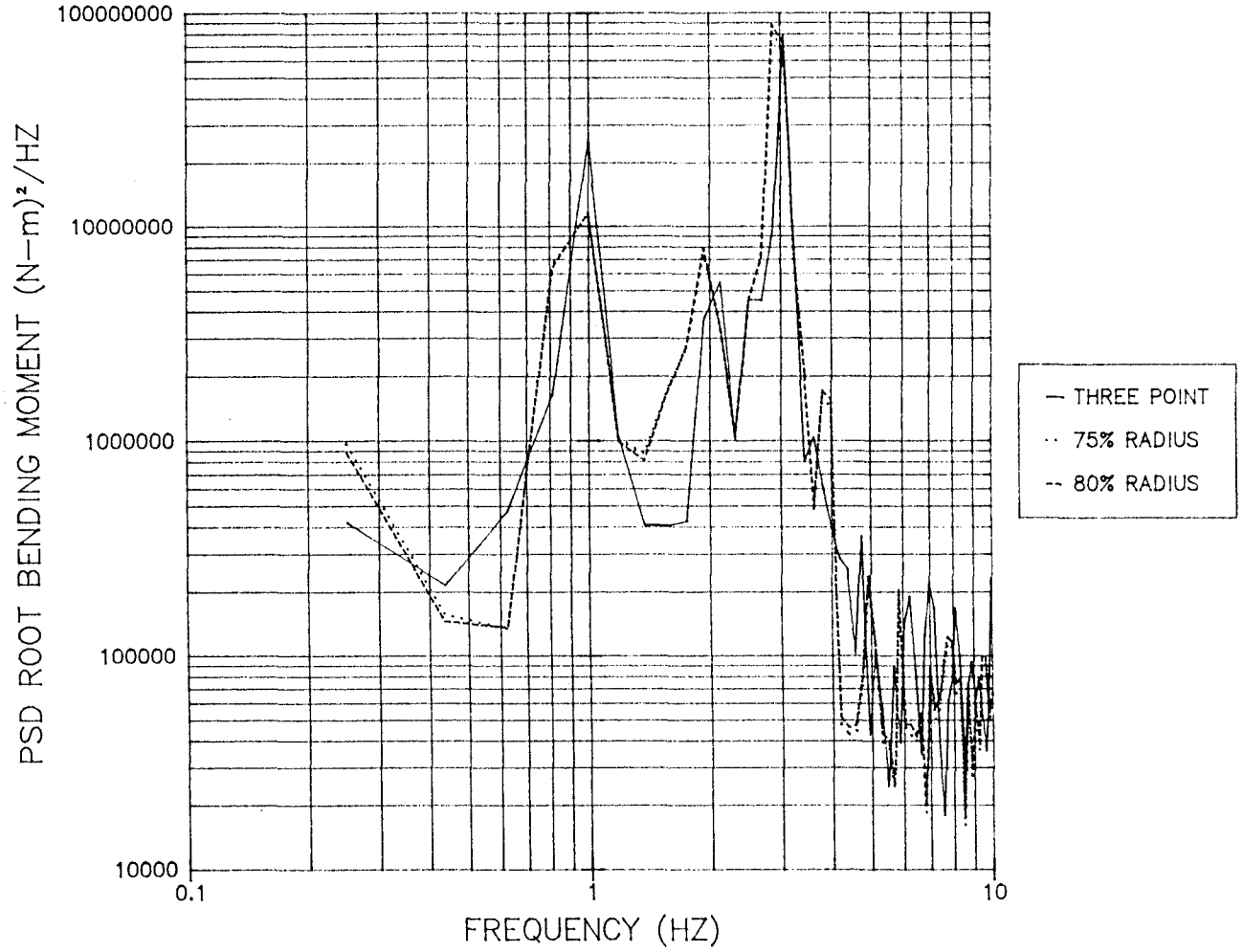

Figure 4.6 Comparison of Power Spectral Densities for Blade Root Bending Moment for a 8.94 m/s Wind with 15% Turbulence

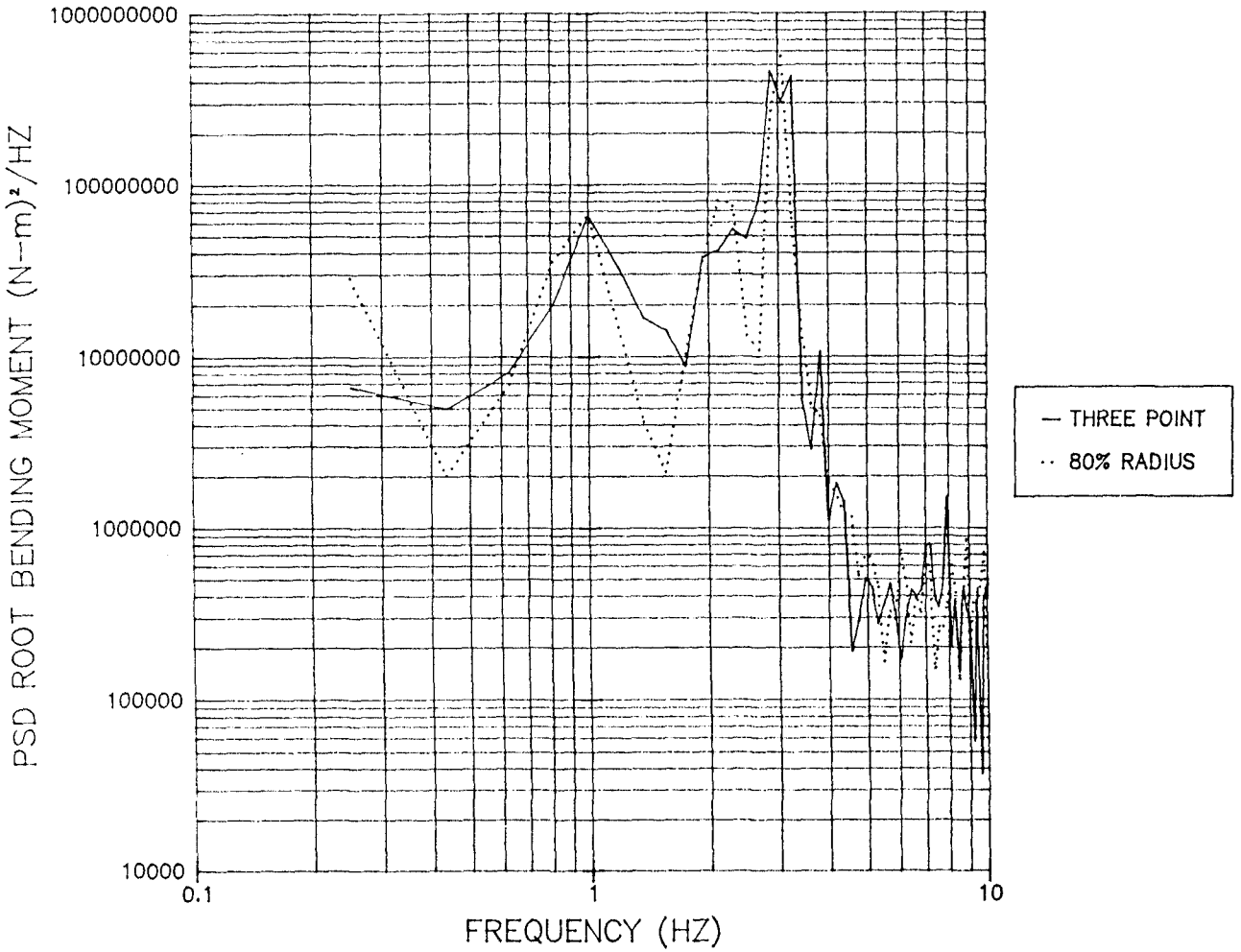

Figure 4.7 Comparison of Power Spectral Densities of Blade Root Bending Moment for a 15.65 m/s Wind with 25% Turbulence

Table 4.1 Rainflow Cycle Counts of Root Bending Moment for 22.35 m/s Wind with 15% Turbulence

Increment (x 2000 N-M)	Cycles Three-pt	Cycles 70.7%	Cycles 75%
1	16	22	23
2	34	21	19
3	8	5	6
4	1	1	1
5	2	0	0
6	1	0	0
7	0	3	1
8	4	0	2
9	1	3	1
10	1	4	4
11	2	2	3
12	1	2	4
13	0	4	2
14	1	2	1
15	1	1	2
16	1	5	5
17	1	0	1
18	0	3	4
19	4	2	1
20	0	1	0
21	1	0	1
22	2	4	2
23	3	0	3
24	1	1	0
25	2	2	2
26	0	1	1
27	3	2	0
28	0	2	3
29	2	0	1
30	1	1	1
31	1	1	1
32	3	0	0
33	0	1	1
34	1	0	0
35	2	0	0
36	2	0	0
37	1	0	0

Table 4.2 Rainflow Cycle Counts of Root Bending Moment for 22.35 m/s Wind with 15% Turbulence

Increment (x 2000 N-M)	Cycles Three-pt	Cycles 75%	Cycles 80%
1	16	23	22
2	34	19	22
3	8	6	7
4	1	1	1
5	2	0	1
6	1	0	0
7	0	1	1
8	4	2	2
9	1	1	0
10	1	4	1
11	2	3	6
12	1	2	4
13	0	2	3
14	1	1	0
15	1	2	2
16	1	5	2
17	1	1	4
18	0	4	5
19	4	1	1
20	0	0	0
21	1	1	0
22	2	2	2
23	3	3	2
24	1	0	2
25	2	2	0
26	0	1	3
27	3	0	0
28	0	3	2
29	2	1	0
30	1	1	3
31	1	1	0
32	3	0	1
33	0	1	1
34	1	0	0
35	2	0	0
36	2	0	0
37	1	0	0

Table 4.3 Rainflow Cycle Counts of Root Bending Moment for 15.64 m/s Wind with 15% Turbulence

Increment (x 2000 N-M)	Cycles Three-pt	Cycles 75%	Cycles 80%
1	90	115	83
2	89	79	55
3	25	18	13
4	7	3	10
5	4	5	6
6	3	4	9
7	1	4	0
8	6	2	2
9	4	2	6
10	1	1	3
11	2	4	2
12	3	1	2
13	2	4	1
14	5	4	4
15	6	2	1
16	2	1	1
17	1	0	2
18	1	2	3
19	2	1	1
20	2	1	0
21	0	0	1
22	1	2	0
23	1	1	0
24	0	0	0
25	0	0	0
26	0	0	0
27	1	0	0

Table 4.4 Rainflow Cycle Counts of Root Bending Moment for 8.94 m/s Wind with 15% Turbulence

Increment (x 2000 N-M)	Cycles Three-pt	Cycles 75%	Cycles 80%
1	132	111	107
2	105	87	89
3	35	13	18
4	15	4	4
5	4	5	5
6	2	3	4
7	4	3	0
8	4	4	2
9	2	4	5
10	8	1	1
11	3	5	4
12	0	5	5
13	2	3	3
14	5	1	2
15	0	1	1
16	4	4	4
17	1	4	1
18	4	2	4
19	2	2	3
20	0	0	1
21	1	1	0
22	0	0	1
23	0	1	0
24	0	1	1
25	1	1	1
26	0	0	1
27	0	0	0
28	0	1	1

Table 4.5 Rainflow Cycle Counts of Root Bending Moment for 15.64 m/s Wind with 25% Turbulence

Increment (x 6000 N-M)	Cycles Three-pt	Cycles 80%
1	85	83
2	47	53
3	19	13
4	9	10
5	3	6
6	3	9
7	2	0
8	3	2
9	4	6
10	6	3
11	2	2
12	1	2
13	4	1
14	2	4
15	2	1
16	0	1
17	3	2
18	4	3
19	1	1
20	1	0
21	1	1
22	1	0
23	1	0
24	0	0
25	0	0
26	1	0

Chapter 5

Variable Speed Loads

The torque loads experienced by a HAWT rotor and drivetrain are dependent on the generator load; the absence of a generator loads will cause the rotor to accelerate or decelerate depending on the aerodynamic torque, a synchronous generator (constant generator speed) will pass the aerodynamic torque through the drivetrain and the generator, a variable speed generator can operate with constant or slowly varying torque to reduce drivetrain torque variations and or follow maximum power efficiency points. The drivetrain system consisting of high and low speed shafts, a gearbox, and couplings have an equivalent torsional stiffness and damping. An impulse generator load will excite this system natural frequency. Typical HAWT drivetrain natural frequencies are on the order of 5-10 periods of the rotor period.

Chapter 5 includes the drivetrain as a fifth degree-of-freedom to analyze various generator configurations in a variety of operating conditions.

5.1 Drivetrain Dynamics

Figure 5.1 shows the drivetrain degree-of-freedom, $\dot{q}_4$ is the rotor angular velocity and $\dot{q}_5$ is the generator angular velocity. For simplicity generator values such as

angular velocity, torque, and inertia are calculated relative to the rotor through the step-up gearbox ratio. The two shafts are joined by a torsional spring, k_{TOR}, and a torsional damper, c_{TOR}. Eq. 2.5.18 is modified such that the restraining torque is given as

$$T = k_{TOR}(q_4 - q_5) + c_{TOR}(\dot{q}_4 - \dot{q}_5) \qquad (5.1.1)$$

The I_{GEN} must be set to zero in Eq's. 2.5.13 and 2,5,14. The fifth dynamic equation can be written as

$$I_{GEN}\,\ddot{q}_5 = T_{GEN} - k_{TOR}(q_4 - q_5) - c_{TOR}(\dot{q}_4 - \dot{q}_5) \qquad (5.1.2)$$

Notice that this equation is coupled only to the fourth degree-of-freedom and not though an acceleration term. This equation can be passed directly to the numerical solving scheme with out using the form of Eq. 2.5.10. This additional equation requires a smaller time step for solution because the natural frequency is higher that the other system natural frequencies.

5.2 Start-Up and Shutdown

All wind turbines regardless of their generator types have a variable speed rotor during start and stop conditions. Turbines may either freewheel or be motored to get them to a normal operating speed and use a variety of braking mechanisms for shutdown. The ESI-80 was used for start-up and shutdown predictions. Teeter springs were added at the teeter stops in the dynamics subroutine. The

springs model the rubber pads that the ESI-80 has for teeter stops. The natural frequency of this spring is approximately 10 rotor periods. Values of 7,872,000 N-m/radian and 9000 N-m-s were used for k_{TOR} and c_{TOR}, respectively. This results in a drivetrain natural frequency of 8 rotor periods and a damping of approximately one percent of critical damping. Figure 5.2 shows DRT predictions of rotor torque and teeter angle as a function of time for a motored start-up. Figure 5.3 shows DRT predictions of the rotor speed and blade root bending moment for the same case. A constant torque of 18,000 N-m was used to accelerate the rotor in a 11.18 m/s (25 mph) wind. After the rated rotor speed is reached (60 rpm), the motor is shut off and the induction generator model is turned on. A teeter angle of seven degrees was used as the initial condition, this corresponds to a blade resting against a teeter stop. Notice that the rotor never hits a teeter stop during this case. The eight period drivetrain ringing can be seen in the first four seconds of the rotor torque. A torque over shoot occurs when the induction machine switches from the motor to an induction generator. The rotor reaches rated speed after eight seconds. A slight over shoot occurs in the rotor speed during the motor to generator transition. The blade root bending moment fluctuations are due only to the blade motion. For this turbine with very little blade twist, the flapping motion and the drivetrain motion are uncoupled. The

periodic spikes seen in the bending moment are due to blade passage though the tower shadow.

Figure 5.4 shows data taken from a normal start-up of the ESI-80; teeter angle, electrical power output, rotor torque, and root bending moment are shown as a function of time. Note that the sign convention of the rotor torque is opposite that used thus far in this thesis. Operating conditions are unknown for this start-up, but general trends can be compared with the predictions shown in Figures 5.2 and 5.3. The ringing in the rotor torque is similar to the prediction as is the magnitude of the torque overshoot when the induction generator is engaged. The electrical power overshoot is compounded from the combined overshoots of the rotor speed and torque. This is in agreement with the predictions. The teeter angle and the bending moment show the same trends as the predictions, but no solid conclusions can be made.

Figure 5.5 shows DRT predictions of teeter angle and blade root bending moment for a motored start-up with a constant torque of 1,800 N-m in a 22.35 m/s (50 mph) case. This case is shown because of the three teeter strikes experienced by the rotor. The rotor hits the teeter spring once at approximately four seconds, is pushed off by the spring, and hits it again one second later. The rotor then hits the teeter spring again on the other side at nine seconds. Notice the sharp spikes in the bending moment caused by the rotor hitting the stops. Figure 5.6 shows

the same case with 15 percent turbulence. The turbulence induced fluctuations in bending moment almost completely obscure the spikes caused by the teeter strikes.

The ESI-80 is equipped with electro-magnetically controlled tip brakes on each blade. During loss of line conditions these tip plates are deployed to exert an aerodynamic braking torque. The magnitude of the braking torque for one blade is approximately $\frac{1}{2}\rho R^3\Omega^2 C_D A$, where $C_D A$ = 0.6 m^2 for the ESI-80. The tip brakes deploy in a tenth of a second through a exponential ramp function, $f_{TB}=(t/\tau)^2(2-(t/\tau)^2)$, where t is the time and τ is one tenth of a second. Figures 5.7 and 5.8 show DRT predictions of teeter angle, root bending moment, rotor speed, and torque for a loss of line condition with tip brakes as the braking torque in a 25 mph wind. The loss of line occurs at one second and the tip brakes are completely deployed at 1.1 seconds. The rotor slows to 25 percent of the rated speed in 20 seconds. A minor rotor over speed is experienced before the tip brakes are totally deployed. Resonant drivetrain ringing occurs for the first four seconds after tip deployment. The teeter angle slowly diverges and the rotor cycles can be seen in the bending moment fluctuations. The tip brake restraining torque eventually equals the torque produced by the blades and with out additional braking the rotor will continue to turn.

The ESI-80 is equipped with a dry caliper brake capable of exerting a restraining torque of 69,000 N-m on

the rotor side when the rotor is stopped. The braking ability decreases linearly with increased rotor speed with a 20 percent maximum decrease at rated speed.

Figures 5.9 and 5.10 show DRT predictions of teeter angle, root bending moment, rotor speed, and rotor torque for a loss of line condition where both tip brakes and the 69,000 N-m mechanical brake are used to restrain the rotor in a 22.352 m/s (50 mph) wind speed. The loss of line occurs at one second and both braking mechanisms are deployed using the 1/10 second ramping function. The rotor is brought to a complete stop in 2.6 seconds. Torque, bending moment, and the teeter angle behave nicely without any large divergences. Figure 5.11 shows root bending moment and rotor torque for the same case with 15 percent turbulence. The bending moment has some high cycle response to the turbulence, while the torque is essentially unaffected.

Figure 5.12 shows data from a loss of line condition from the ESI-80. Electrical power, teeter angle, rotor torque, and bending moment are shown as a function of time. Again, operating conditions are unknown so a direct comparison cannot be made with code predictions. Instead, general trends will be compared. The loss of line starts when the electrical power drops from 200 Kw to 0 Kw. It appears from the torque plot that the mechanical brake does not engage for approximately one second. Once the brake engages, the characteristic drivetrain ringing can be seen.

The rotor stops after 3.6 seconds. The additional time to stop compared with the prediction of 2.6 seconds could be due to the one second delay of the brake onset during which the rotor is accelerating. The odd oscillations in rotor torque at the end of the stop are believed to be caused by brake "stiction," where the brake seizes with the rotor momentarily. Teeter angle and bending moment follow the same trends as the predictions.

5.3 Generator Models

Three generator models are evaluated under normal operating conditions. Blade root bending moment and rotor torque are examined using azimuthal averaging and power spectral densities for all three cases. The synchronous generator operates at a constant angular velocity, removing the generator degree of freedom. The induction generator model allows some variation in angular velocity due to generator slip. This model was discussed in Chapter 2. The induction model used with the drivetrain degree-of-freedom is numerically unstable except for extremely small time steps. A 0.07 second moving average of the generator torque was added to remove the instability. The variable speed generator operates with a slowly varying torque that keeps the turbine operating at an optimum tip speed ratio. The tip speed ratio is based on a moving average of the wind speed for 1.4 seconds. Consequently torque variations

are on the order of one revolution or greater. This model was also discussed in Chapter 2. All three cases were run using the Veers' full field turbulence simulation model with a single-point at the 80% station, as suggested by the conclusions of Chapter 4, with a mean wind speed of 8.94 m/s (20 mph) and a turbulence intensity of 15 percent. This wind speed case was chosen as it is closest to the design optimum tip speed ratio, between 8 and 11. A tip speed ratio of 8.6 was used in the variable speed model. To operate at the true optimum tip speed ratio would require the wind speed to be so low that the loads would be difficult to examine. A drivetrain spring constant of 3,900,000 N-m/radian was used in this analysis. This spring value results in a drivetrain natural frequency of approximately 5 Hz. 1024 turbulent wind values were simulated with a time increment of 1/72 of a second. This corresponds to 72 azimuthal locations for a rotor speed of 60 rpm.

Figure 5.13 compares DRT predictions of the azimuth averaged root bending moment for the three generator cases. The variable speed slowly varying torque model has a slightly higher mean. This is due to a slightly lower mean rotor speed which results in less centrifugal bending relief. Although, the same turbulent wind was used the different rotor speeds cause the turbulence to be sampled at different rotor positions. This may be the cause of the different cyclic histories. Figure 5.14 compares the power

spectral densities of the root bending moment for the same case. The induction and synchronous generator models have similar results with strong energy spikes at two and three periods. The variable speed generator model has much less energy at one Hertz. This is due to the larger variation of rotor speed which tends to spread the one period component over a range of frequencies. None of the generator models show significant spikes at 5 hertz where the drivetrain resonance is located. The standard deviation of the bending moment for the induction and synchronous generator models is 30 and 31 percent higher than that of the variable speed model, respectively.

Figure 5.15 shows DRT predictions of the rotor torque for the same three cases. The synchronous generator has huge two period oscillations. This model locks out the fifth degree-of-freedom causing the rotor to ring at its natural frequency which due to a much higher inertia is approximately two Hertz. This resonance is excited by the blades passing through the tower shadow and by two Hertz rotational turbulence. The variable speed model has some ringing at the drivetrain five Hertz resonance. Figure 5.16 compares the rotor torque power spectral densities for the three cases. The synchronous generator model has a large spike at two Hertz and the variable speed model has a similar spike at five Hertz. The induction generator model has a small spike at two Hertz, but this is probably due to the tower shadow rather than the rotor resonance. The

standard deviation of the rotor torque for the induction and synchronous models were 30 percent lower and 175 percent higher than the variable speed model, respectively. The moving average of the induction model torque may have played a part in the lower spectral energy of this model.

5.4 Variable Speed Energy Capture

The ESI-80 yearly energy capture is compared using a variable speed generator and induction generator. Figure 5.17 show the ESI-80 power coefficient versus the tip speed ratio. A peak coefficient of 0.42 occurs ar a tip speed ratio of eleven. The ESI-80 operating with an induction generator and rated speed of 60 rpm has its design wind speed at 7 m/s (15.5 mph). The most efficient variable speed energy capture method is to operate the rotor at a tip speed ratio of eleven for all wind speeds. Unfortunately, at a moderate wind the turbine would be operating with a tip speed high enough to worry about compressibility effects. In addition, the centrifugal bending moment will be much larger than the aerodynamic bending and the power output would greatly exceed the ESI-80's 300 Kw generator. Obvious solutions to these individual problems would be to decrease the rotor swept rotor area, decrease the blade coning angle, and install a larger generator, respectively. Rather than investigate the effect of many parameters on variable speed operation,

the ESI-80 energy capture will be analyzed using the ESI-80 "as is" with its present design constraints.

Figure 5.18 show the tip speed schedule to be used for the DRT prediction of the ESI-80 variable speed yearly energy capture. A tip speed schedule was chosen that balances the centrifugal and aerodynamic blade root bending moments, for the ESI-80 that was achieved with a constant tip speed ratio of nine. A tip speed ratio of nine is sufficiently close to the peak tip speed ratio of eleven to maximize energy capture. At approximately 12.5 m/s, the variable speed tip speed schedule decreases at a value that holds the generator output at 275 Kw, with the added benefit of keeping the blade tip speed from becoming to high. The turbine will reach a maximum rotor speed of 90 rpm using the tip speed schedule of Figure 5.18.

Figure 5.19 compares DRT prediction of the power curve for the fixed and variable speed configurations. The variable rotor speed power exceeds the fixed rotor speed power at every wind speed except near the fixed rotor speed design wind speed, which is approximately 8 m/s for a tip speed ratio of nine. Yearly energy capture depends on a wind speed distribution. A Weibel distribution of the form

$$P(W \geq W_p) = \exp[- (\frac{W_p}{c})^k] \qquad (5.4.1)$$

can be used, where $P(W \geq W_p)$ is the probability that the wind speed will be greater than the wind speed W_p in question, and c and k are site characteristics. Frost [1] gives

average values of c=3.17 and k=1.59 for California. Using these values and the power curves of 5.19 results in a total energy capture for one year of 244,700 Kw-hr and 318,700 Kw-hr for the induction and variable speed configurations, respectively. The ESI-80 has a tower natural frequency at approximately 0.5 Hertz. The benefit of not operating the turbine at a rotational frequency near this resonance is greater than the low energy capture at the wind speed where this occurs, below 5 m/s. This reduces the variable speed yearly energy capture to 302,900 Kw-hr or a 24 percent energy capture gain over the fixed speed machine.

Figure 5.20 compares DRT prediction of the mean root bending moments for the fixed and variable speed machines. Variable speed operation has a zero bending mean up to approximately 12.5 m/s. The variable speed bending increases up to a value 6 percent higher that the induction bending moment at a wind speed of 23.8 m/s. A prediction of the change in the bending moment fatigue lifetime using the variable speed configuration can not be made using Figure 5.21 since other parameters such as the wind speed distribution and the turbulence intensity levels are involved.

5.5 References

1. Frost, W., Long, B., "Engineering Handbook on the Atmospheric Environmental Guidelines for Use in Wind Turbine Generator Development," The University of Tennessee Space Institute, Tullahoma, Tennessee, NASA 8-32118, July, 1977.

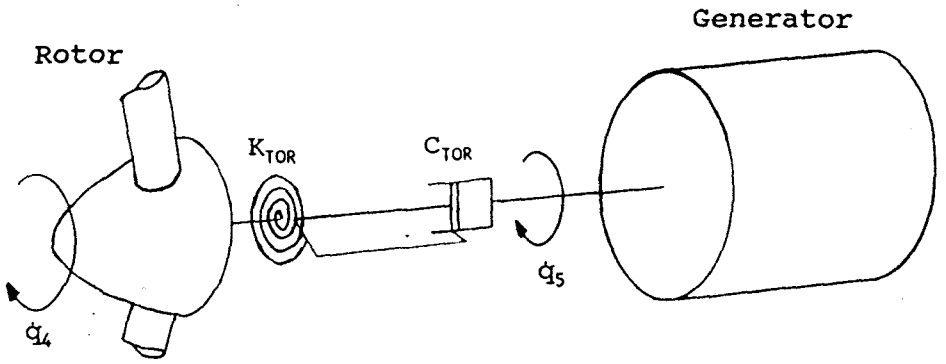

Figure 5.1 Drivetrain

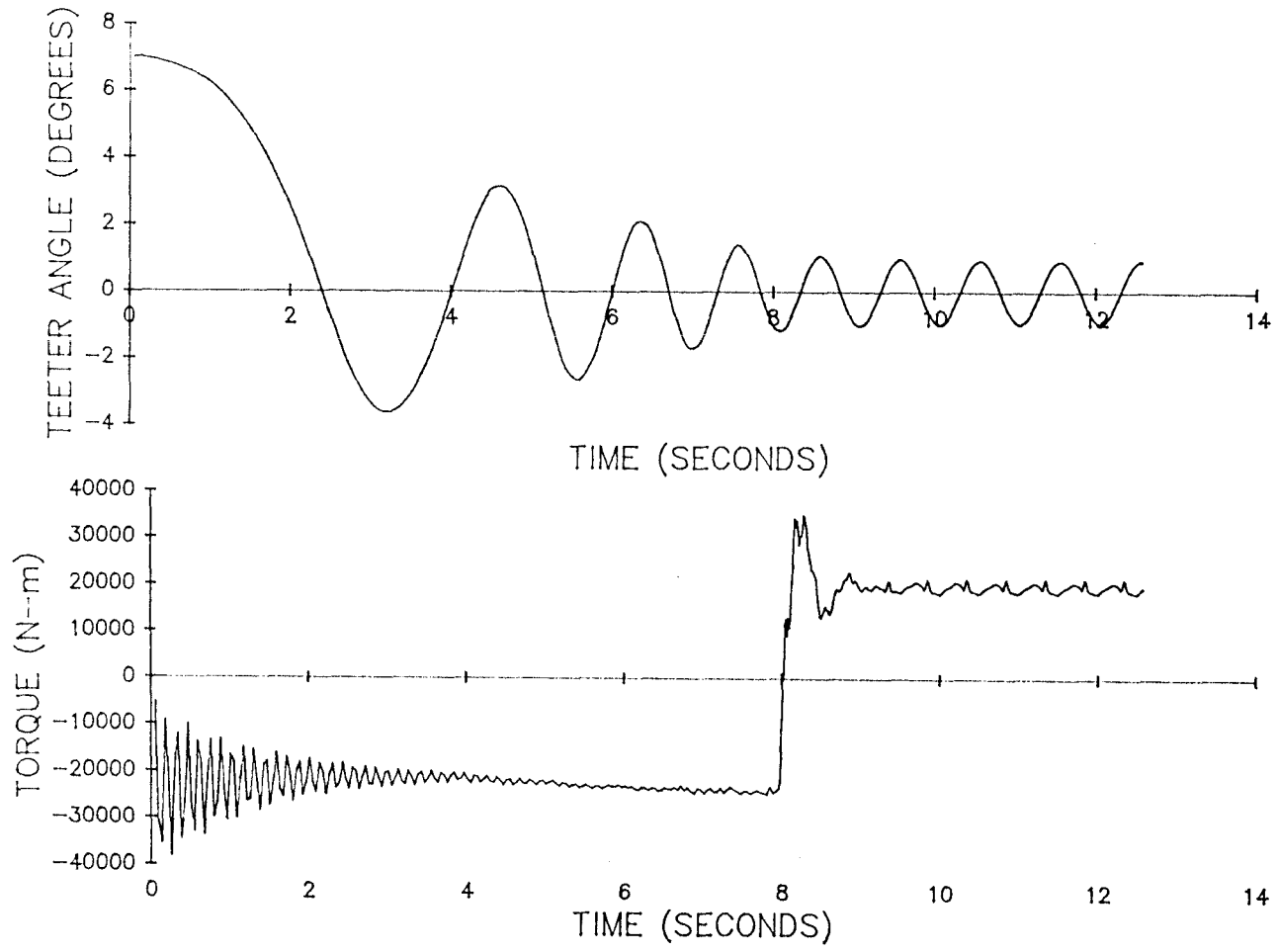

Figure 5.2 DRT Prediction of Rotor Torque and Teeter Angle for a Start-Up in a 11.18 m/s Wind

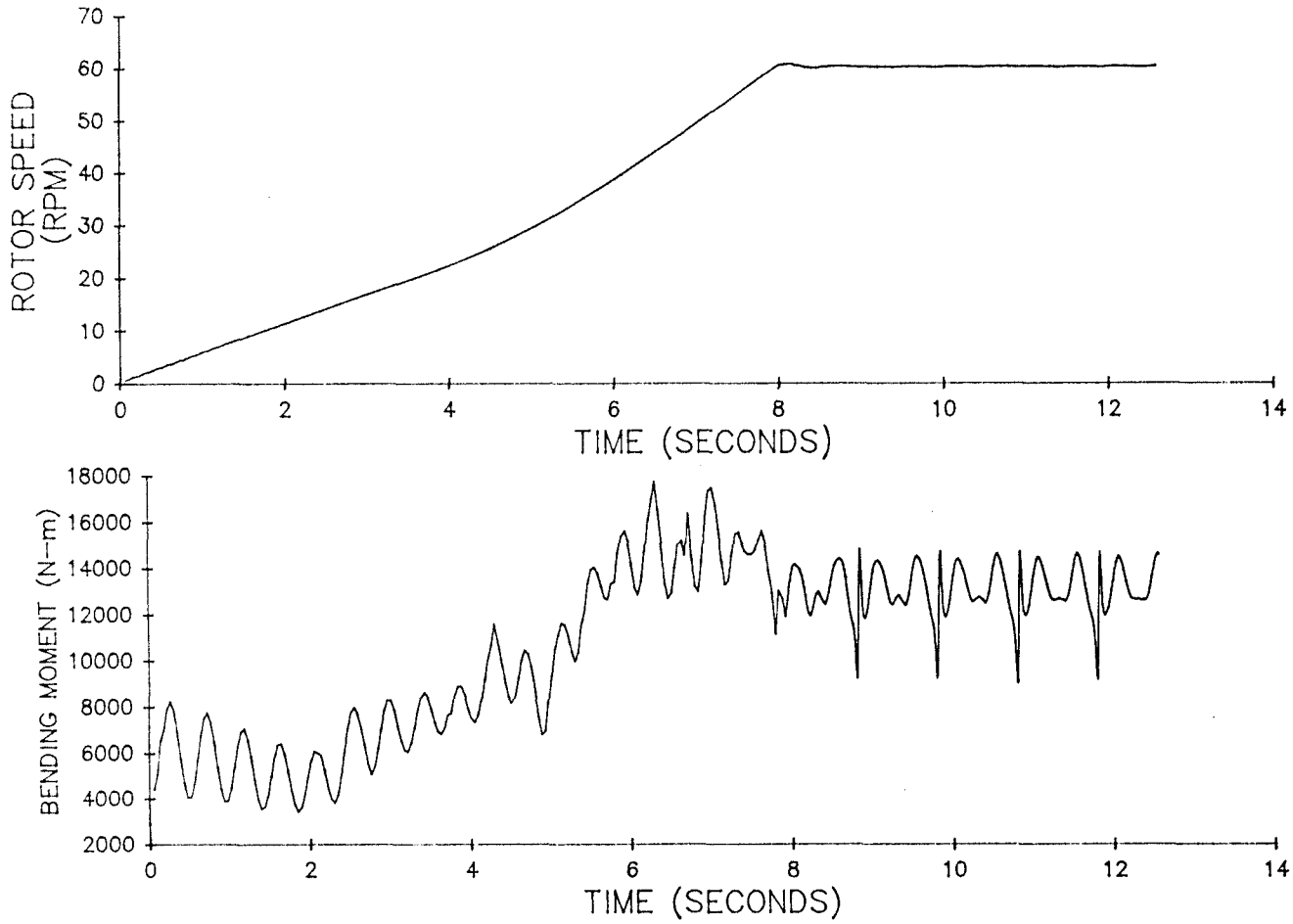

Figure 5.3 DRT Prediction of Rotor Speed and Blade Root Bending for a Start-Up in a 11.18 m/s Wind

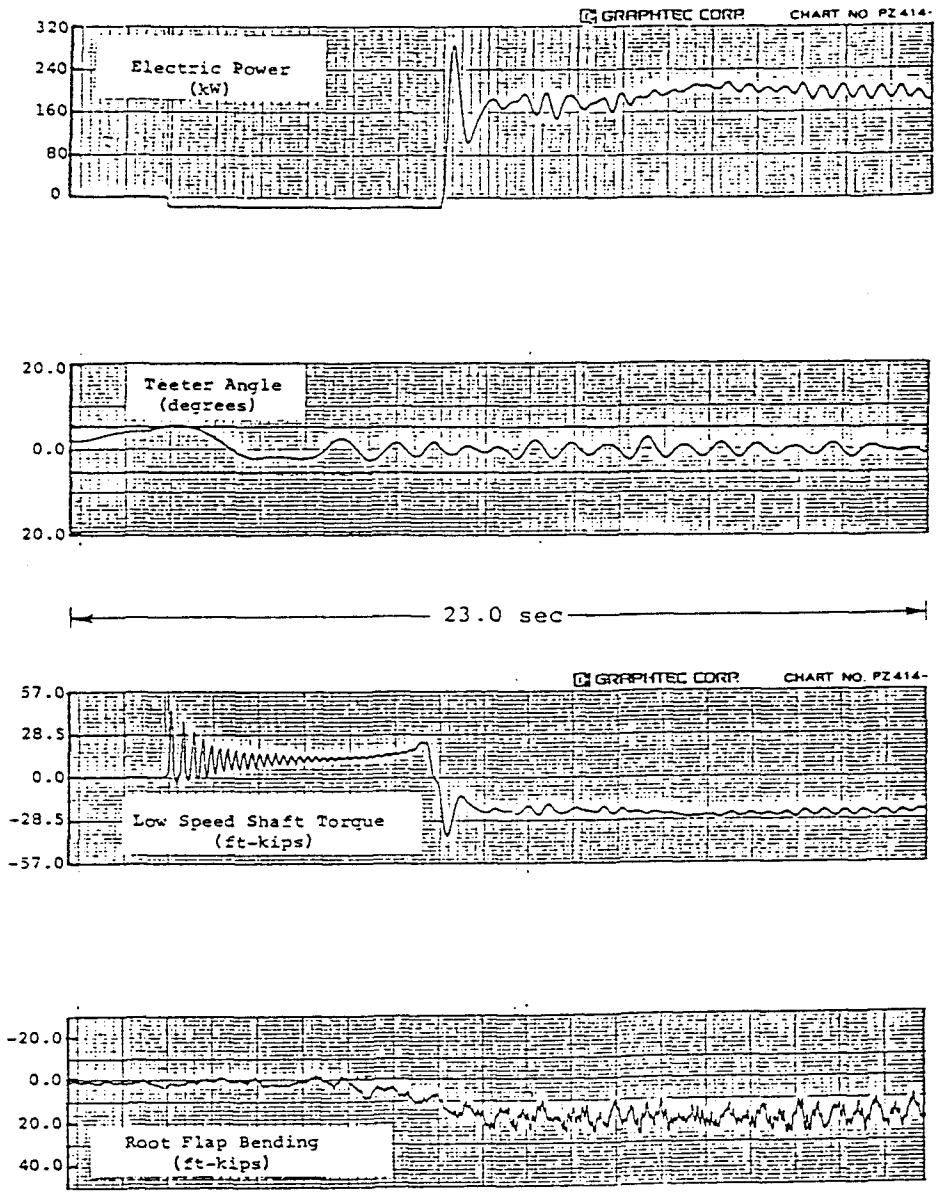

Figure 5.4 ESI-80; Electrical Power, Teeter Angle, Rotor Torque, and Blade Root Bending Moment Start-Up Data

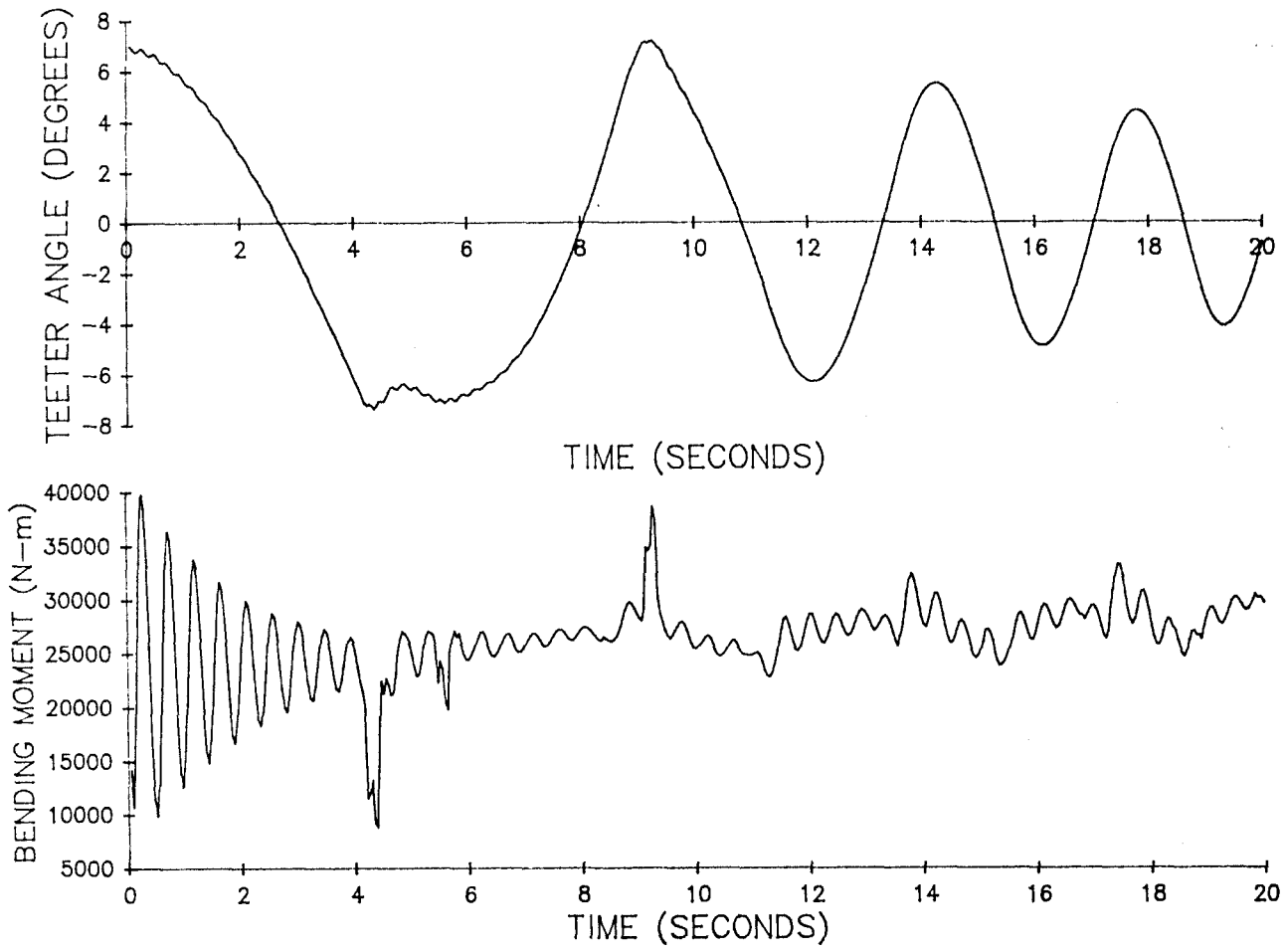

Figure 5.5 DRT Predictions of Teeter Angle and Blade Root Bending Moment for a Start-Up in a 22.35 m/s Wind

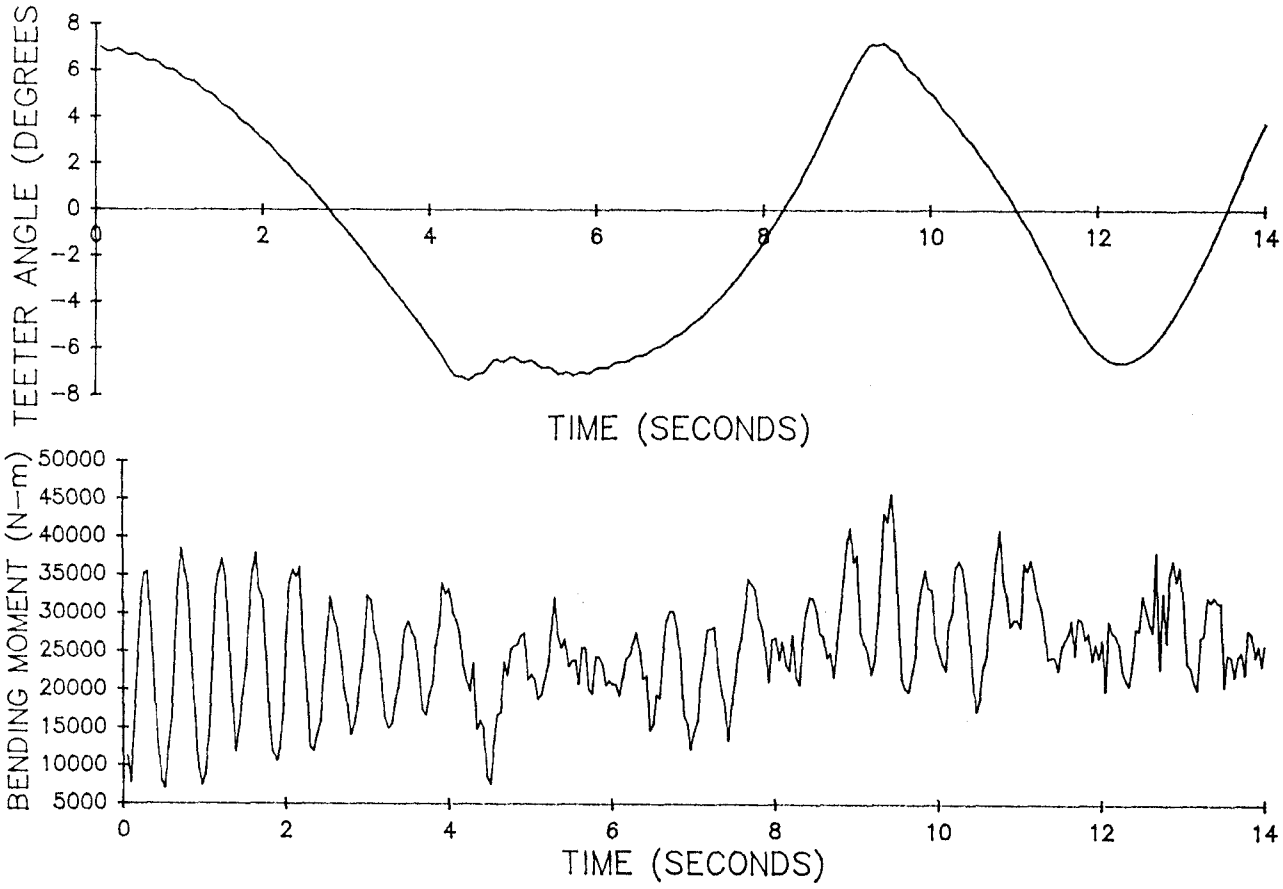

Figure 5.6 DRT Predictions of Teeter Angle and Blade Root Bending Moment in a 22.35 m/s Wind with 15% Turbulence

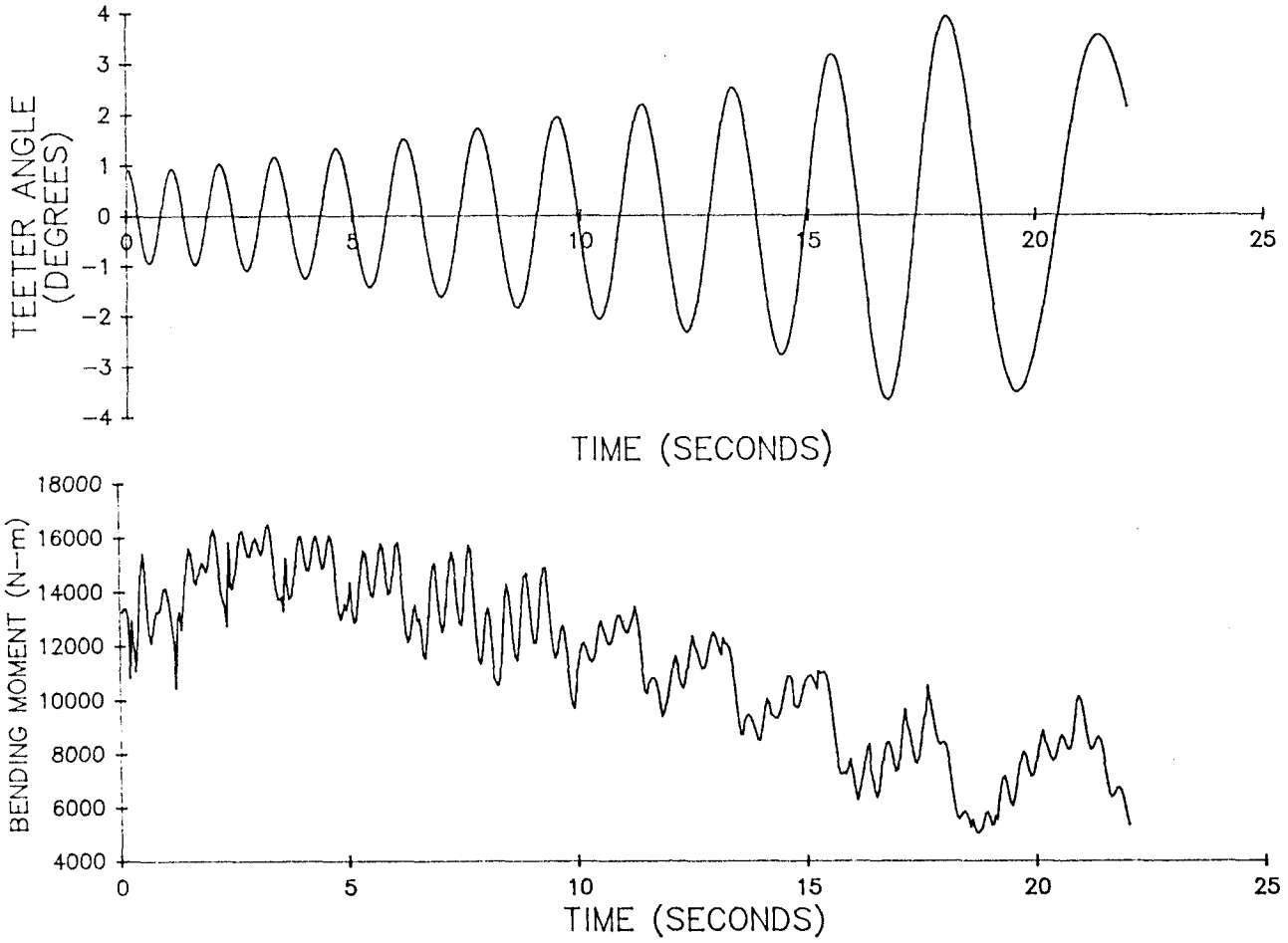

Figure 5.7 DRT Predictions of Teeter Angle and Blade Root Bending Moment for a Loss of Line with Tip Brakes

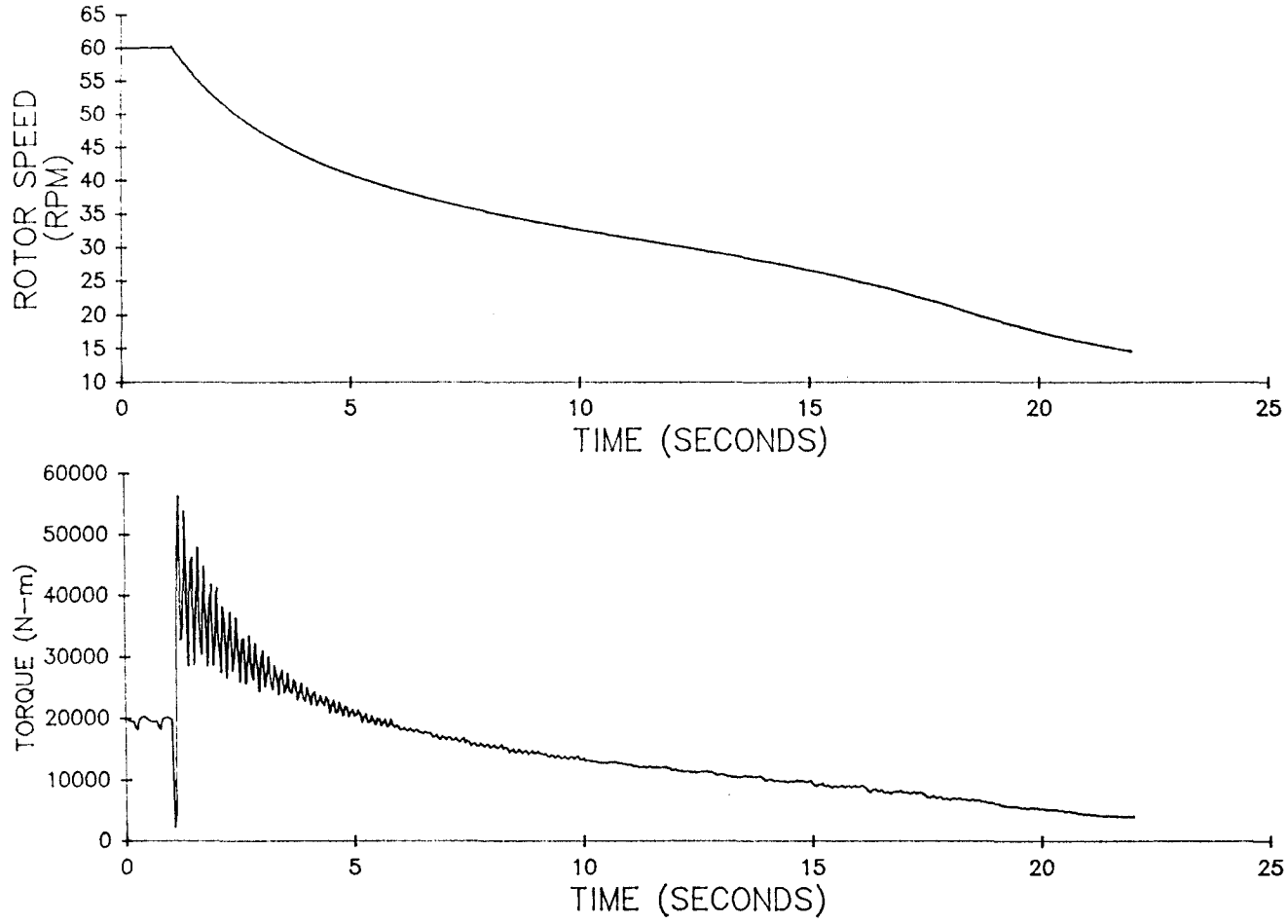

Figure 5.8 DRT Predictions of Rotor Speed and Rotor Torque for a Loss of Line with Tip Brakes

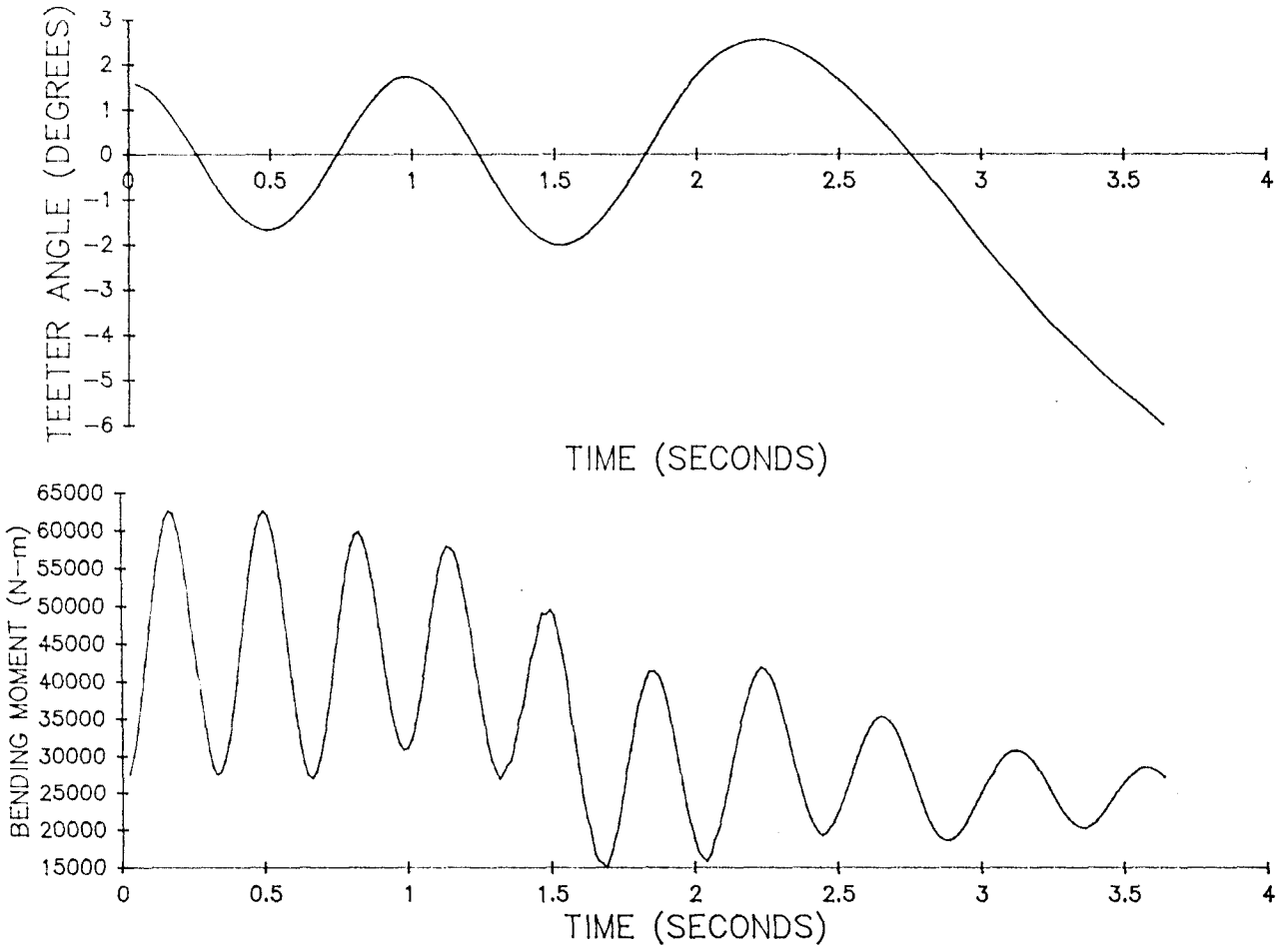

Figure 5.9 DRT Predictions of Teeter Angle and Blade Root Bending Moment for a Loss of Line with Mech. and Tip Brakes

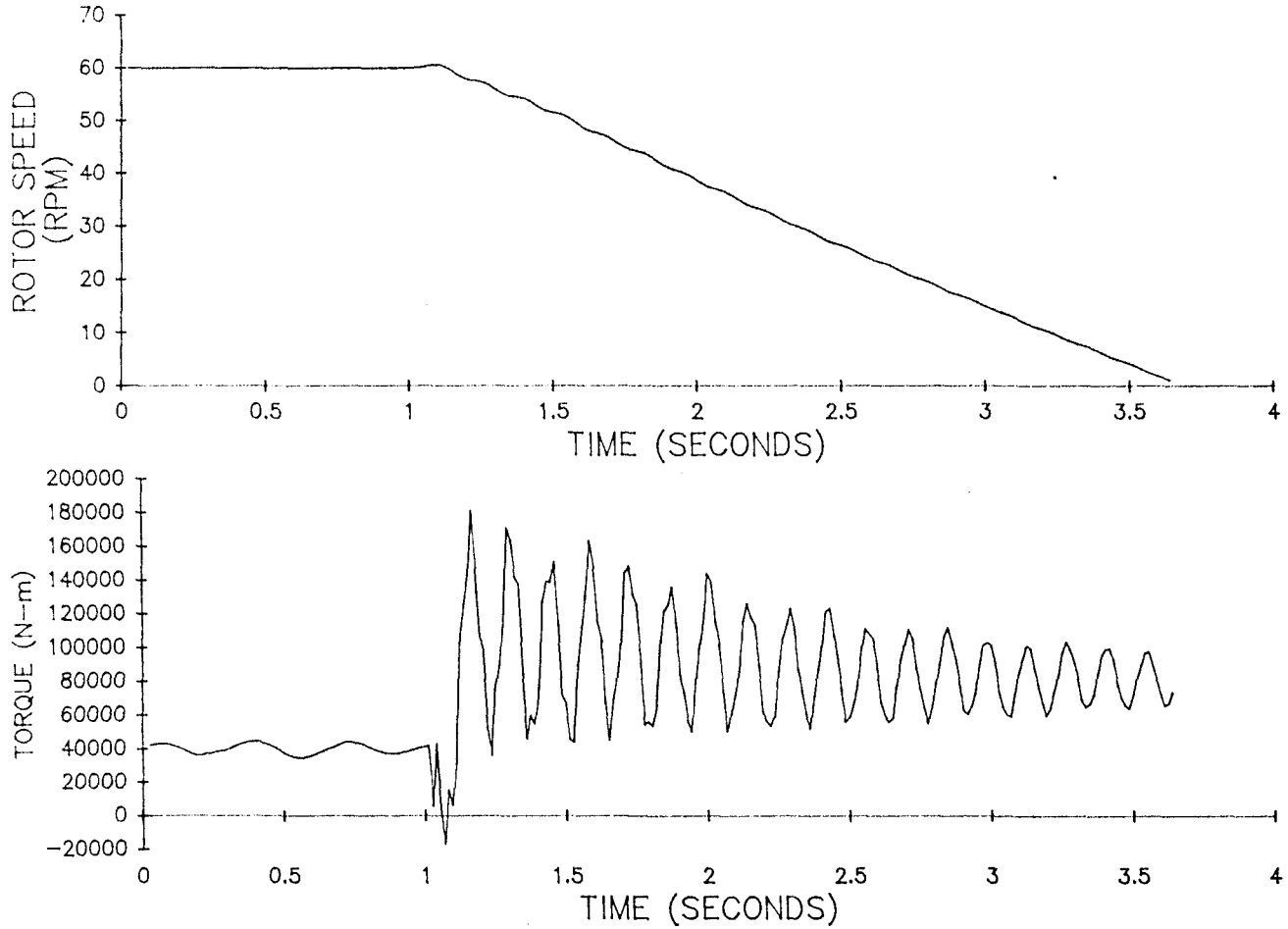

Figure 5.10 DRT Predictions of Rotor Speed and Rotor Torque for a Loss of Line with a Mechanical and Tip Brakes

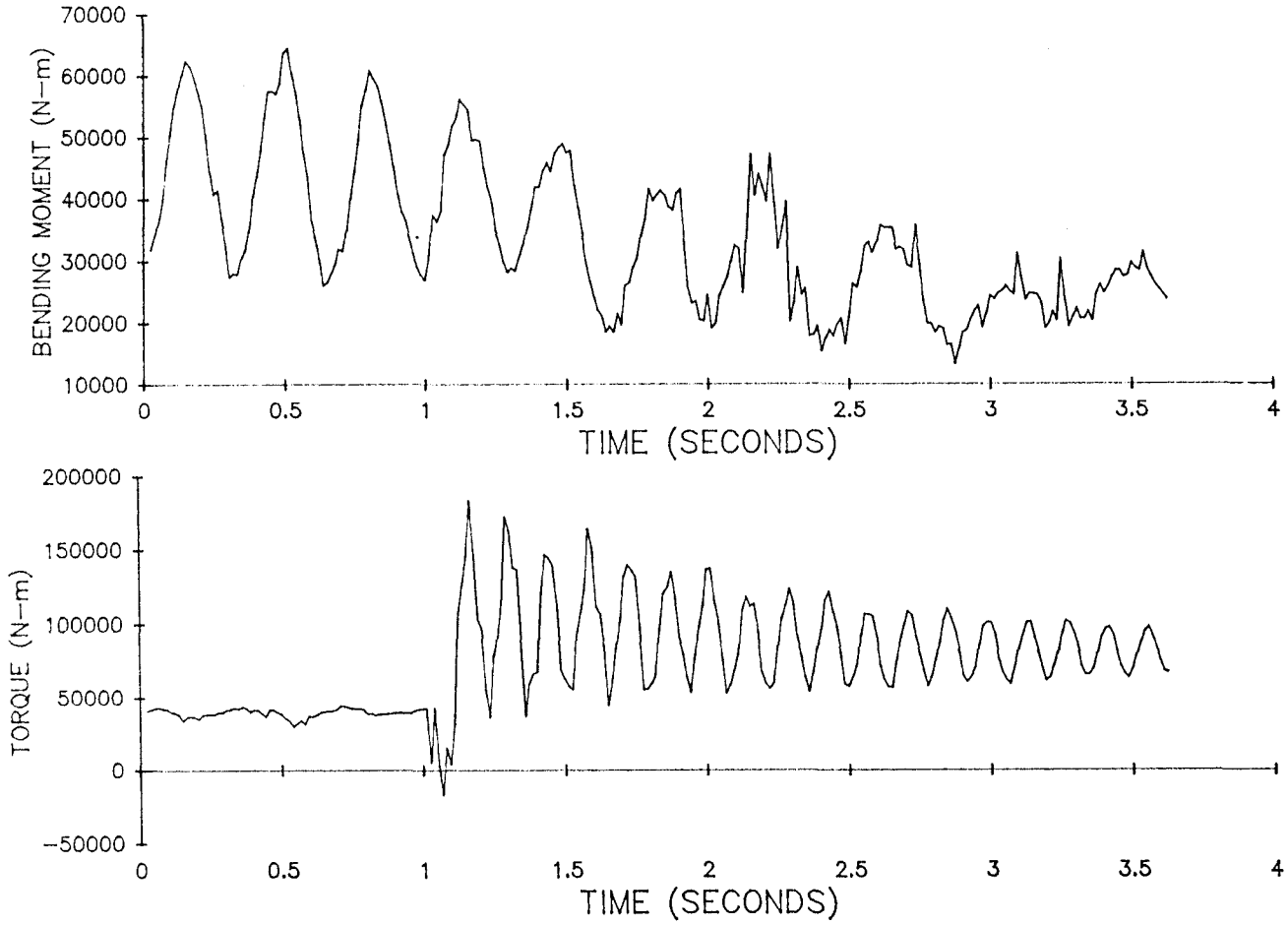

Figure 5.11 DRT Predictions of Bending Moment and Rotor Torque for a Loss of Line with 15% Turbulence

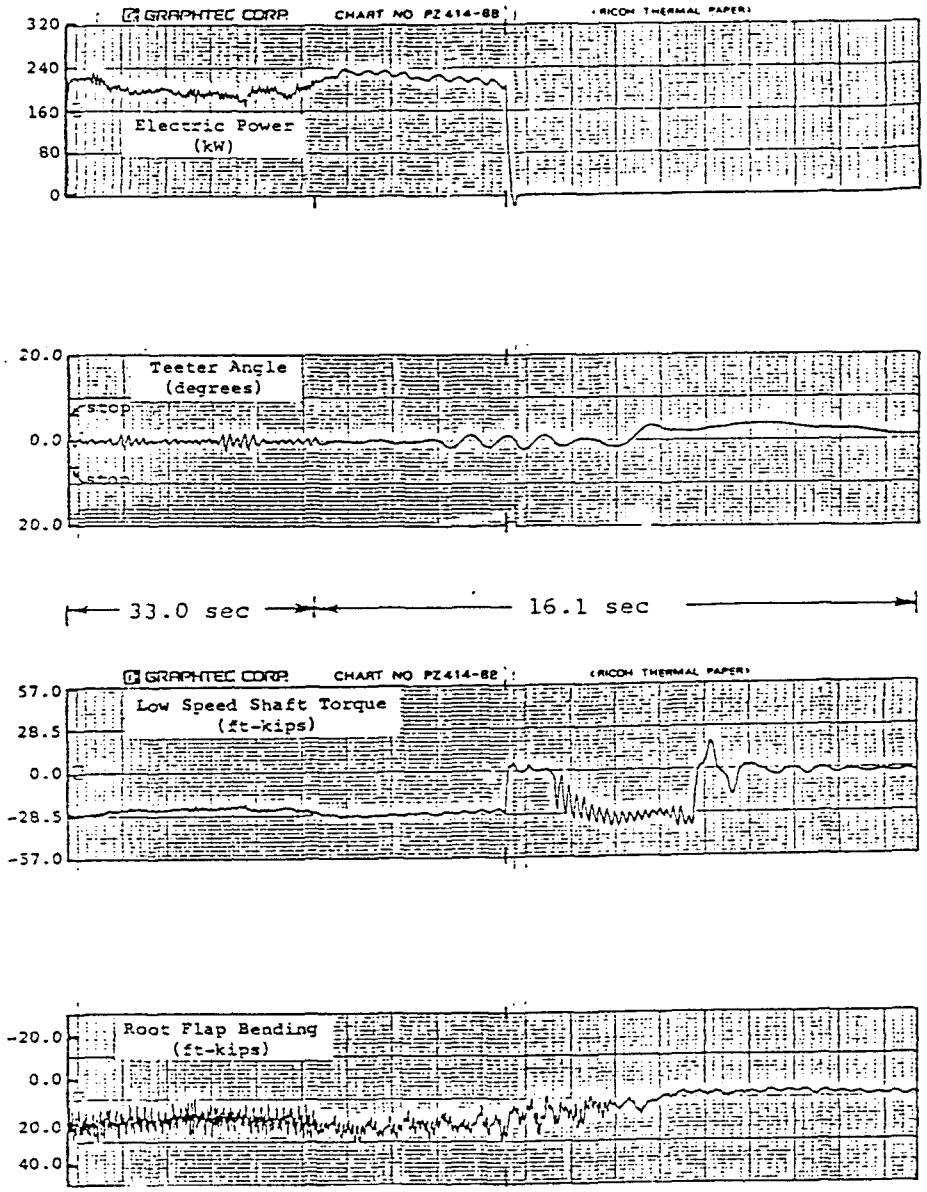

Figure 5.12 ESI-80; Electrical Power, Teeter Angle, Rotor Torque, and Blade Root Bending Moment Loss of Line Data

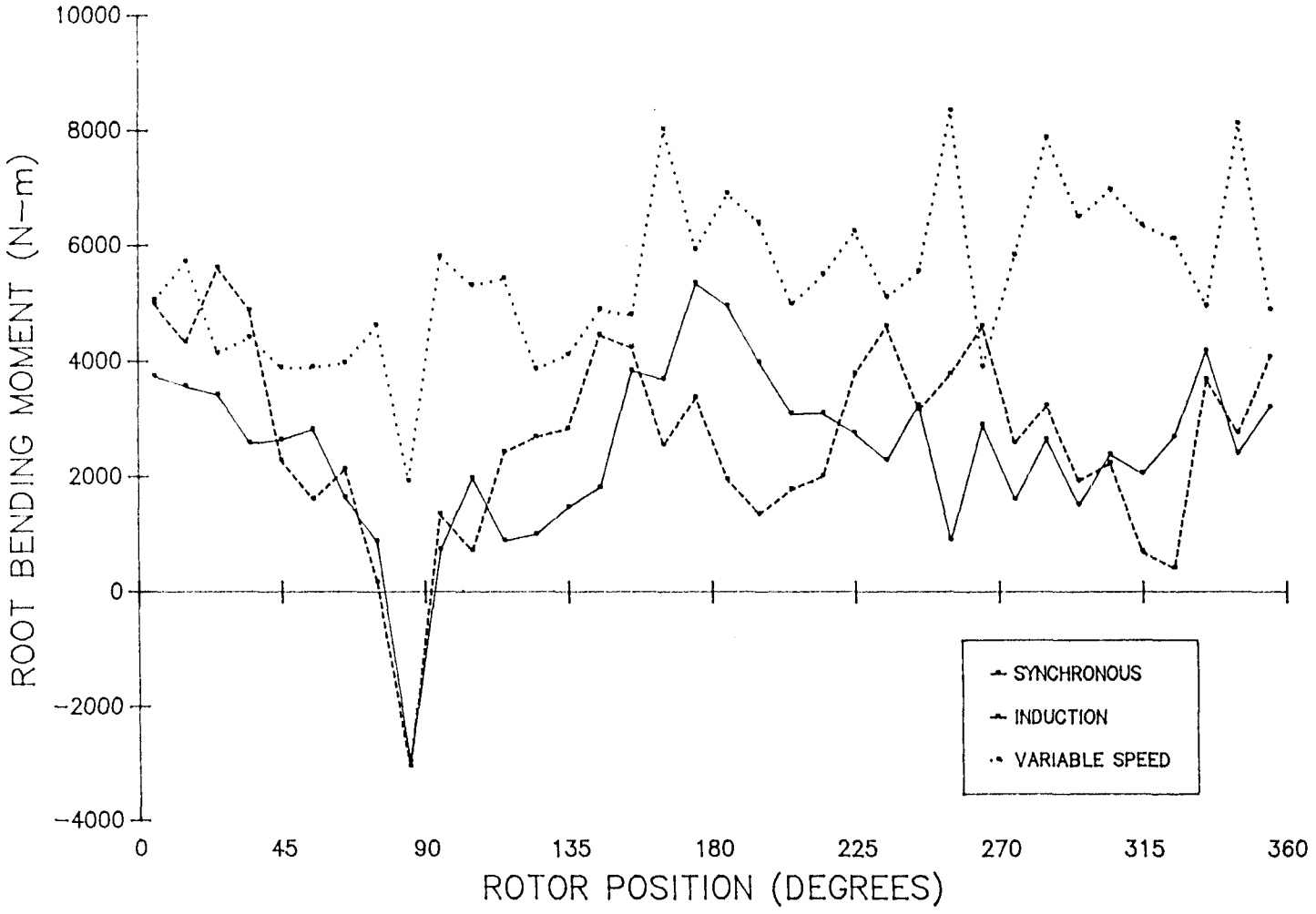

Figure 5.13 Comparison of Azimuth Averaged Blade Root Bending Moment for Three Generator Cases

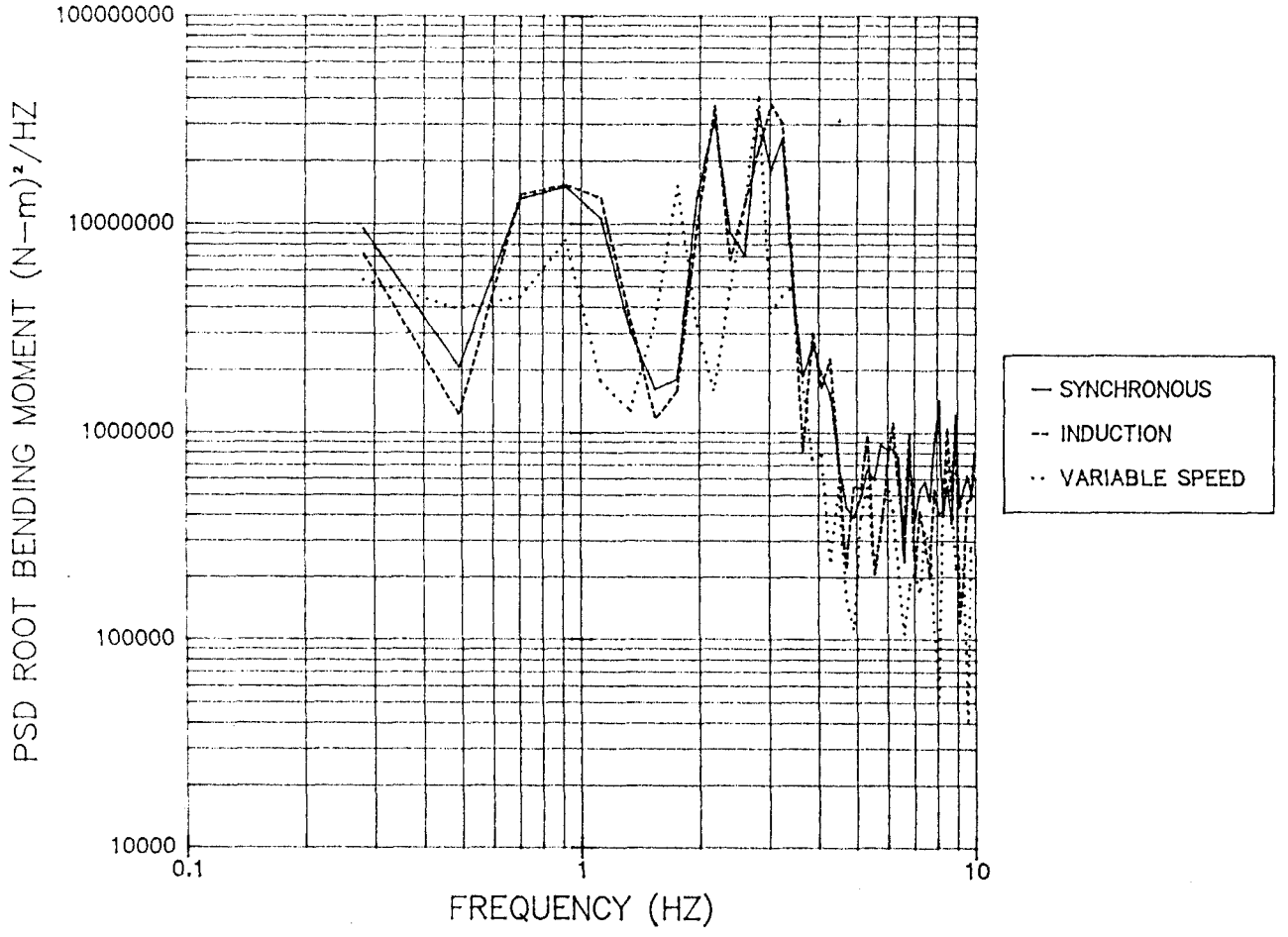

Figure 5.14 Comparison of PSD of Blade Root Bending Moment for Three Generator Cases

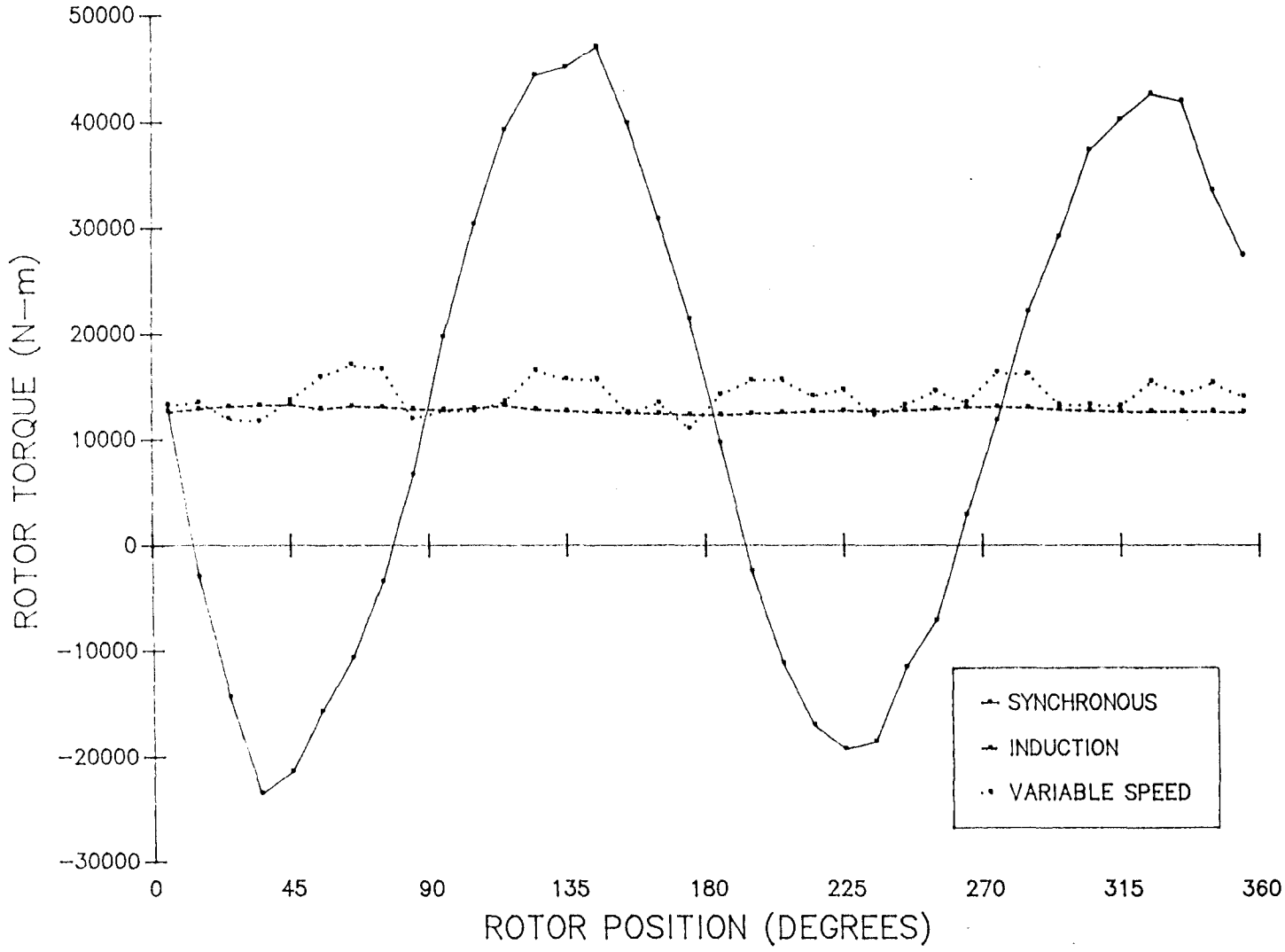

Figure 5.15 Comparison of Azimuth Averaged Rotor Torque for Three Generator Cases

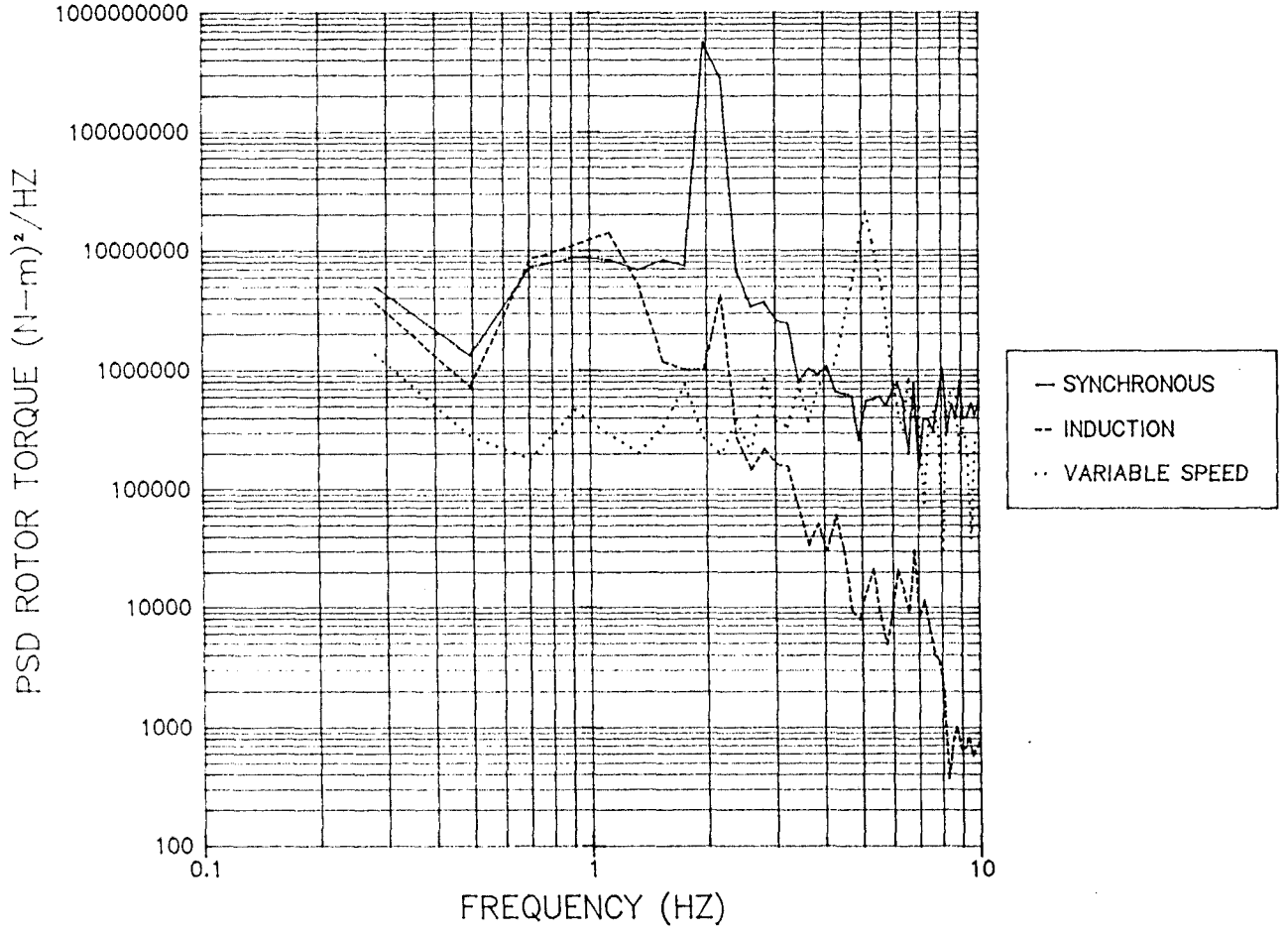

Figure 5.16 Comparison of PSD of Rotor Torque for Three Generator Cases

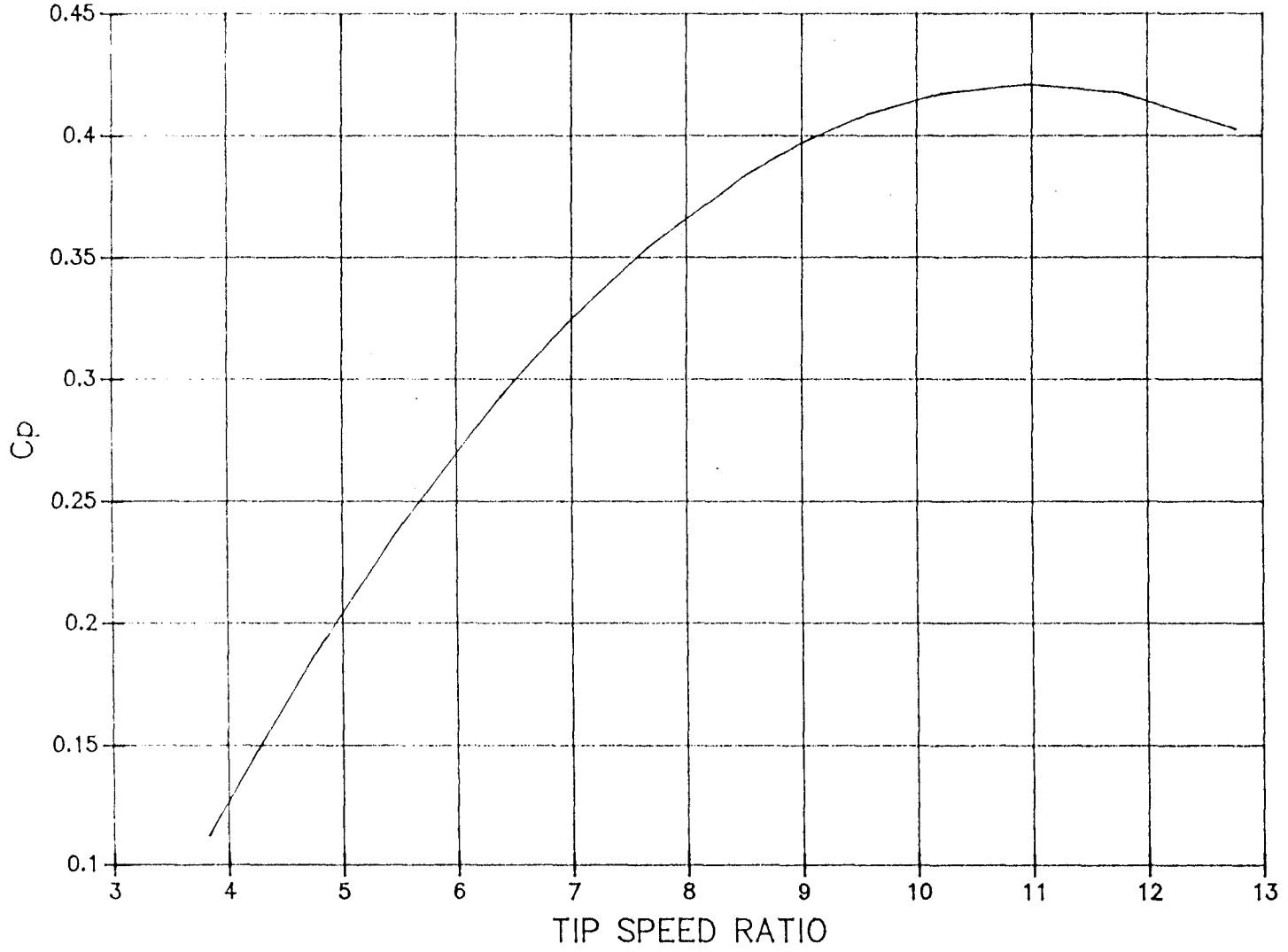

Figure 5.17 ESI-80 Power Coefficient Curve

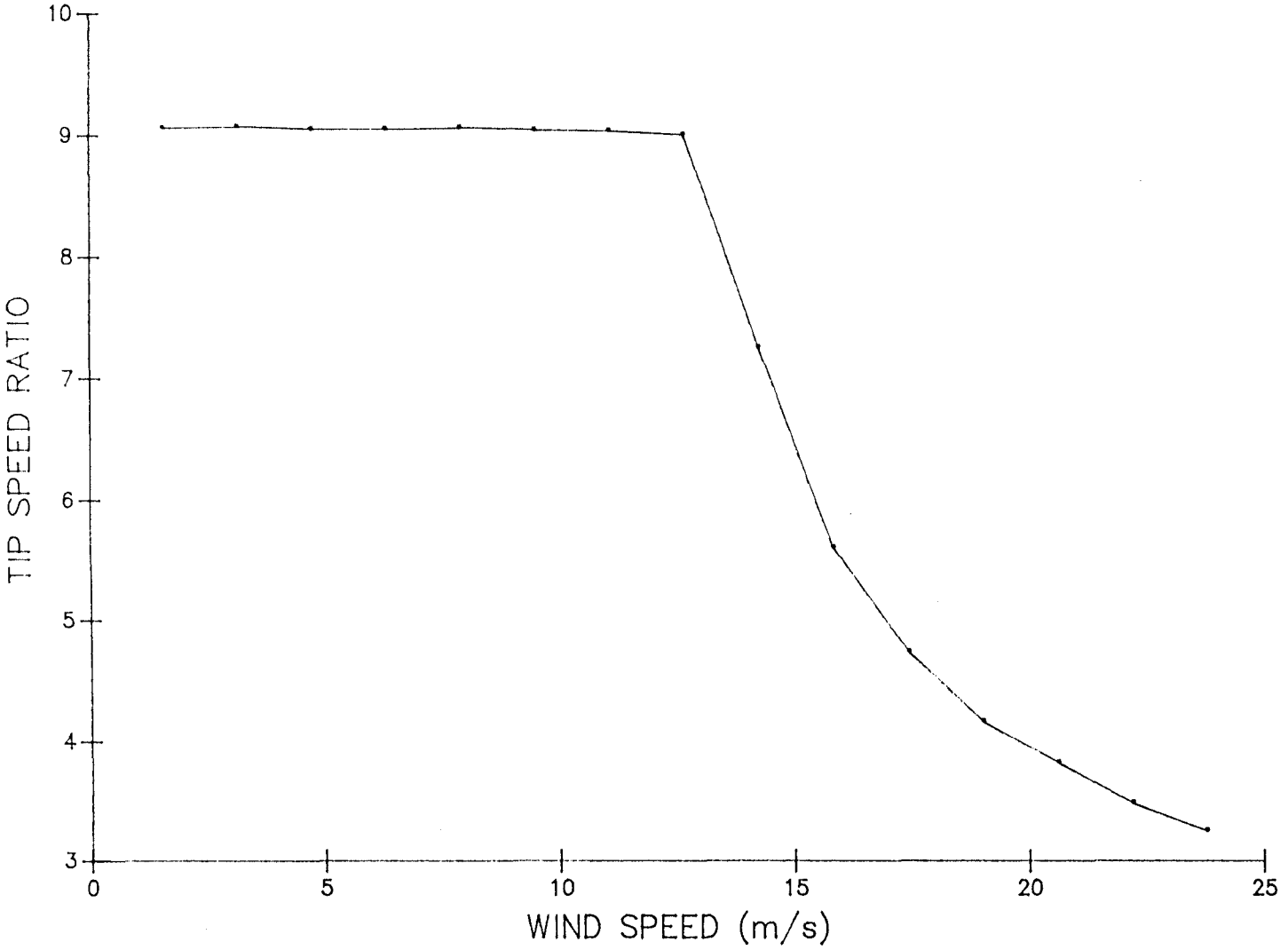

Figure 5.18 ESI-80 Variable Speed Tip Speed Schedule

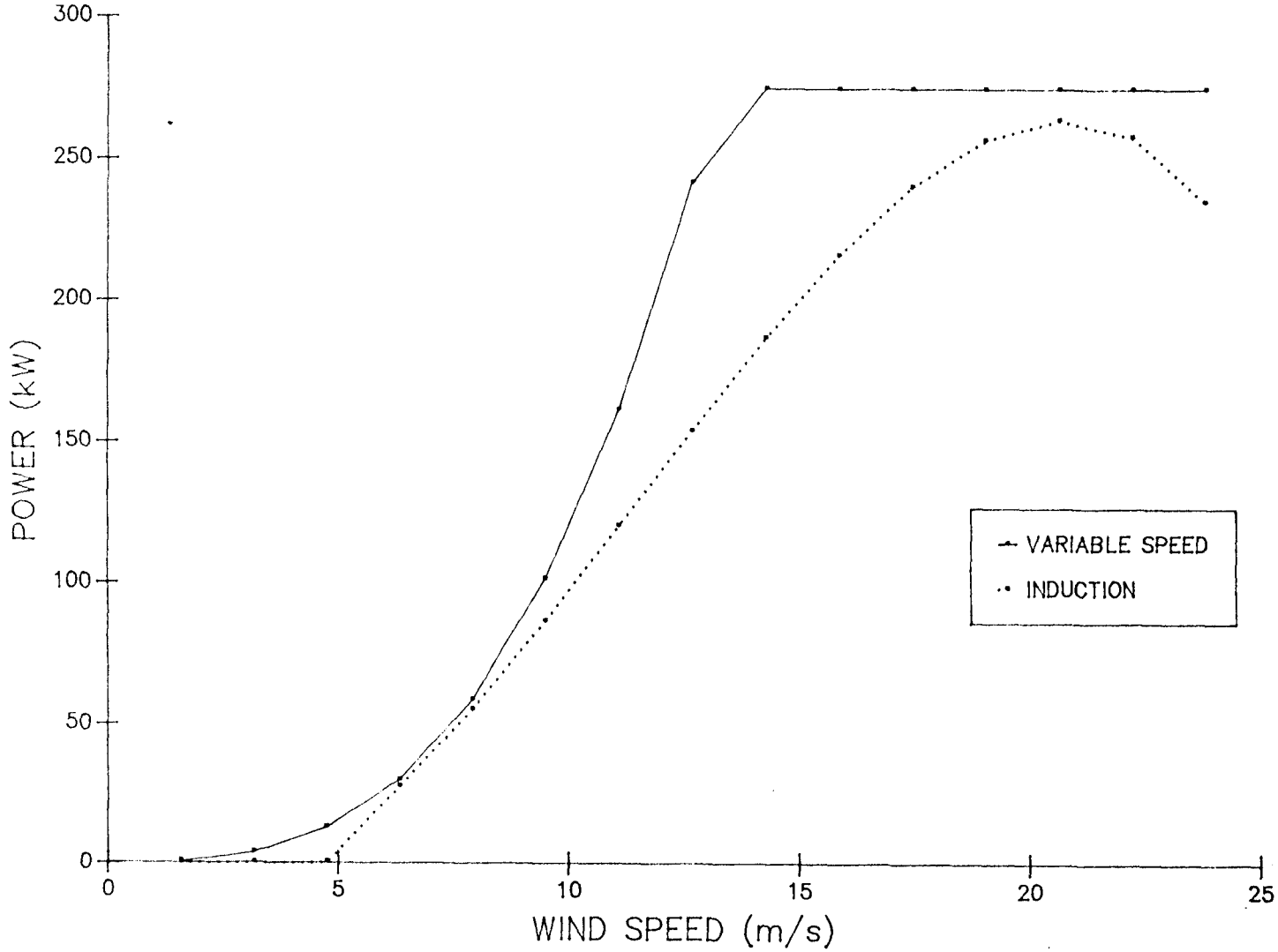

Figure 5.19 Comparison of Fixed and Variable Speed Power Capture

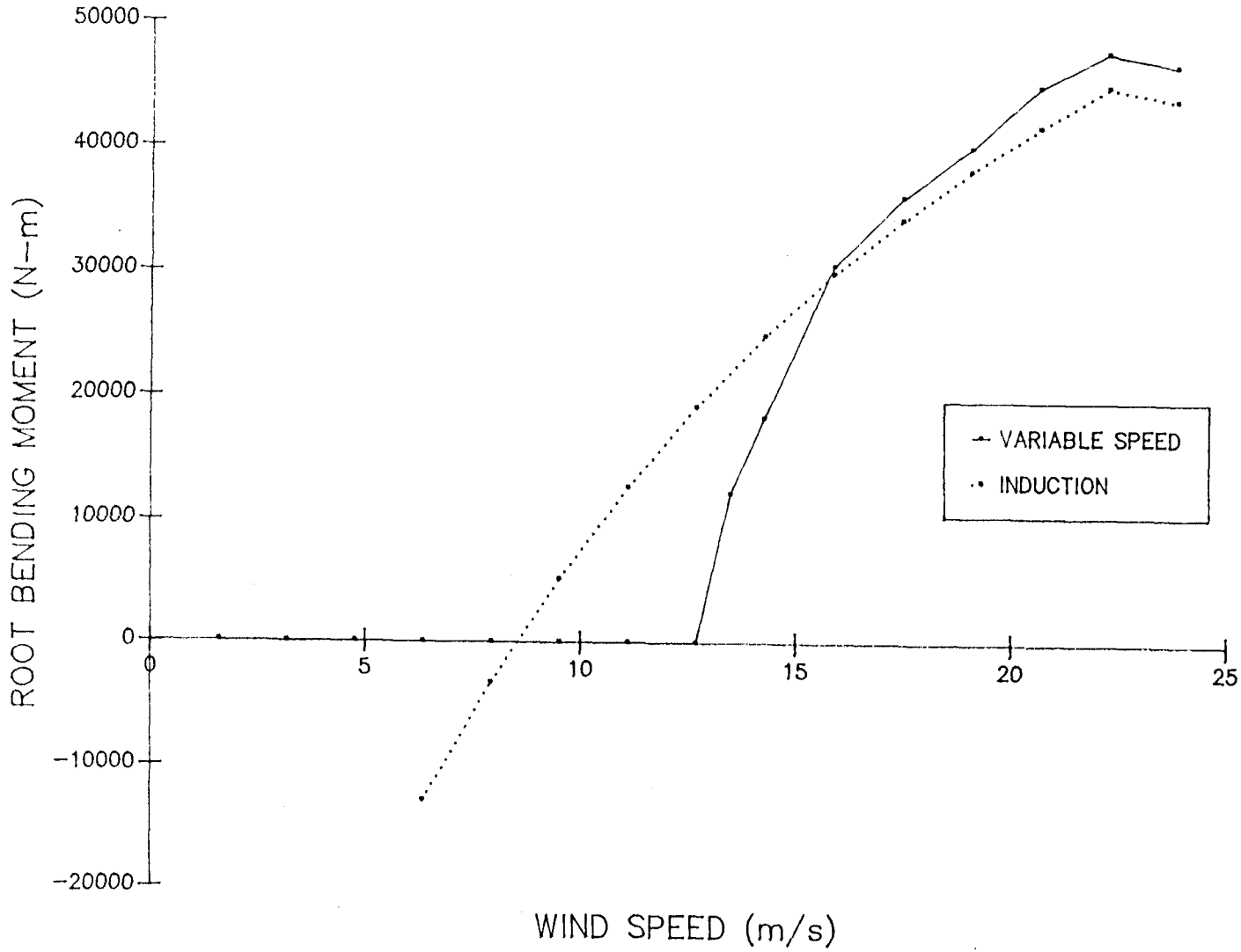

Figure 5.20 Comparison of Fixed and Variable Speed Mean Blade Root Bending Moment

Chapter 6

Summary and Conclusions

The objective of this work was to develop and validate a dynamics model of a two-bladed, teetered HAWT with a variable speed generator and study the effects of deterministic and stochastic loading in a variety of operating conditions. The stochastic loading arises from the turbine interaction with atmospheric turbulence. Optimization of single-point turbulence simulation model was necessary for determining turbulence induced loads.

6.1 Dynamics Modeling

Four degrees-of-freedom were used to model a HAWT with two flexible blades, a teetered rotor, and a variable speed generator. In addition, a fifth degree-of-freedom was added to model the drivetrain. Time independent geometric parameters included in the analysis were; rotor yaw, rotor tilt, delta-3, precone, an elastic bending axis, and a rotor undersling. Each blade deflected in a direction perpendicular to the axis of the blades smallest moment of inertia. The deflection was modeled using an assumed mode shape. The kinematics for blade points were determined and together with holonomic partial velocities and angular velocities, generalized forces were constructed. Generalized active forces were determined from gravity

loads, aerodynamic loads, and a generator torque load. Aerodynamic lift and drag were determined using a combination of momentum and blade element theory. Deterministic wind loading resulted from wind shear and tower shadow. The resulting five equations-of-motion were solved using a Gaussian matrix inverter and a Runge-Kutta started Predictor-Corrector scheme.

6.2 Validation of Model

Comparisons were made between the DRT code loads predictions and experimental and analytical loads. Elimination of some degrees-of-freedom with equation linearization allow analytical solutions to be found. Analytical solutions were found for a simple constant property blade with linear aerodynamics and for linearized teeter motion with a delta-3 angle. The DRT code accurately predicted blade displacement and teeter excursions for these two cases, respectively. The DRT code predictions of mean and cyclic loads were compared to ESI-80 data. Mean and cyclic blade root bending moment, rotor torque, and rotor thrust were adequately predicted. Cyclic teeter angle was also well predicted.

6.3 Single-Point Turbulence Simulation

A single-point turbulence model was optimized by

comparing the DRT code predictions of rotor blade bending moment induced by using various radial stations in the single-point turbulence simulation model to the bending moments induced by a three-blade-point turbulence model. Blade root bending moment was compared using power spectral densities and rainflow cycle counting. Generally, the single-point simulations show more high frequency energy content. The three-point simulation tends to average some of the turbulence over the blade transferring energy from high to low frequencies. This effect will become more pronounced as the number of turbulence points on the blade increases approaching the limit of continuous turbulence. A 80 percent radial station is the most conservative and optimal point for single-point turbulence simulation. The corresponding power spectral density of the bending moment is well preserved, although the spectra area is high for low wind speeds and low for high wind speeds. No significant variations between the three-point model and the 80 percent model power spectral densities was noted for changes in the turbulence intensity. It was recommended that rainflow cycle increments be multiplied by a factor of 1.2 when using rainflow cycle counting for fatigue analysis. This allows better representation of the high, most damaging, cycles.

This optimization was done for the ESI-80 with a rotor diameter of 25.4 meters. Larger turbines may require a larger rainflow cycle correction factor as more turbulence

will be averaged over the blade transferring energy from high to low frequencies.

6.4 Variable Speed Predictions

A number of start-up and shutdown scenarios were examined with and without turbulence. DRT code predictions of load trends were compared to ESI-80 data trends, when available. Drivetrain ringing was found to be substantial for sudden applied torques. The drivetrain ringing would definitely reduce the fatigue lifetime of turbines in a wind regime requiring many starts and stops. The ESI-80 tip brakes were able to prevent rotor overspeed, but additional braking was required to bring the rotor to a complete stop.

Rotor torque and blade root bending moment were compared using the DRT code with three different generators under normal operation. A synchronous, an induction, and a variable speed generator were modeled. The 80% single-point turbulence simulation model was used to create a turbulent wind input. The variable speed generator reduced the standard deviation of the root bending moment by approximately 30 percent compared to the synchronous and induction generators. The variable speed rotor torque standard deviation was 30 percent higher than the induction model rotor torque, however the variable speed generator torque was nearly constant. This results in a significant

increase in the fatigue life of the high speed shaft, which is more susceptible to fatigue damage than the low speed shaft.

The variable speed generator used with a control model tailored for the presently configured ESI-80 resulted in a increase of the yearly energy capture by 24% over an induction generator at a California site.

6.5 Conclusions

The five degree-of-freedom model developed in this thesis adequately predicts rotor and blade loads for a HAWT with a variable speed rotor in a variety of operating conditions. A full field turbulence simulation model supplies a turbulent wind input for examination of stochastic loads. The DRT code can be used to study the effects of turbine parameters with variable speed operation on turbine loads.

6.6 Future Work

Areas were future work is needed are as follows:

a) use the DRT code to do parametric studies of; delta-3, elastic bending axis, yaw, tilt, undersling, and mass and twist unbalances.

b) test variable speed generator control models that reduce loads and optimize power capture with the DRT code.

c) test start-up and shutdown models with the DRT code.

d) add tower dynamic degrees-of-freedom to the DRT code, including tower motion fore and aft, and tower twist.

e) add a yaw degree-of-freedom, separate from tower twist to the DRT code.

f) add a blade pitch degree-of-freedom to the DRT code.

g) develop an advanced full field turbulence simulation model.

h) add an advanced aerodynamics model to the DRT code, including, unsteady aerodynamics and dynamic stall.

References

Anderson, M.B., "The Interaction of Turbulence with a HAWT," Proc. of the British Wind Energy Assoc., March 24-26, 1982, Cavendish Lab, University of Cambridge.

Anderson, T.S., Hughes, P.S., Klein, F.F., Mutone, G.A., "Double-fed Variable Speed Generating System Testing," Fourth ASME Wind Energy Symposium, Dallas, Texas, February 17-21, 1985.

Bongers, P., Engelen, T., Dijkstra, Kock, Z., "Optimal Control of a Wind Turbine in Full Load," EWEC, Glasgow, Scotland, July 10-13, 1989.

Bramwell, A.R.S., Helicopter Dynamics, Edward Arnold Ltd., London, 1976.

Carlson, O., Tsiolis, S., and Johansson, G., "Variable Speed AC-Drive System with Pitch or Yaw Control," Wind Power, San Francisco, California, October 5-8, 1987.

Connell, J.R., "The Spectrum of Wind Speed Fluctuations Encountered by a Rotating Blade of a WEC," PNL 4083, Pacific Northwest Laboratories, Richland, Washington, 1981.

Coriante, D., Foli, U., Sesto, E., Taschini, A., Aviola, S., and Zappala, F.," GAMMA 60 1.5 MW WTG, "EWEC, Glasgow, Scotland, July 10-13, 1989.

Derdelinckx, R., Hirsh, Ch., "Dynamic Load Calculations of Horizontal Axis Wind Turbines," EWEC, Glasgow, Scotland, July 10-13, 1989.

Ernst, J., "Control of a Variable Speed WEC with a Synchronous Generator and a DC Link Convertor," EWEC, Hamberg, West Germany, Oct. 22-26, 1984.

Feitsom E.A.N., Meadm D.J., "Parametric Resonance in HAWTS," EWEC, Glasgow, Scotland, July 10-13, 1989.

Frost, W., Long, D.H., Turner, R.E., "Engineering Handbook on the Atmospheric Environment Guideline for Use in Wind Turbine Generator Development," NASA TP-1359, Dec., 1979.

Froude, R.E., Transactions, Institute of Naval Architects, Vol. 30, p. 390, 1889.

Garrad, A.P., Hassan, U., "The Dynamic Response of Wind Turbines for Fatigue Life and Extreme Load Prediction," EWEC, Rome, Italy, Oct. 7-9. 1986.

Gessow, A., Meyers, G.C., Aerodynamics of the Helicopter, Fredrick Ungar Publishing Co., New York, 1952.

Glauret, H., "On Contradiction of the Slipstream of an Airscrew," ARC Reports and Memoranda, No. 1067, 1926.

Glauret, H., "The Analysis of Experimental Results in Windmill Brake and Vortex Ring States of an Airscrew," ARC Reports and Memoranda, No. 1026, 1926.

Goldstein, S., "On the Vortex Theory of Screw Propellors," Proc. Royal Soc. A123, p. 440, 1929.

Hansen, A.C., Butterfield, C.P., Cui, X., "Yaw Loads and Motions of a Horizontal Axis Wind Turbine," European Wind Energy Conference (EWEC), Glasgow, Scotland, July 10-13, 1989.

Hartin, J.R., "Evaluation of Prediction Methodology for blade loads on a Horizontal Axis Wind Turbine," Ninth ASME Wind Energy Conference, New Orleans, Louisiana, January 14-18, 1990.

Hock, S.M., Thresher, R.W., Cohen, J.M., "Performance and Cost Projections for Advanced Wind Turbines," Ninth ASME Wind Energy Symposium, New Orleans, Louisiana, January 14-18, 1990.

Hodges, D.H., "Review of Composite Rotor Blade Modeling," AIAA J. Vol. 28, No. 3, 1990.

Hohenemser, K.H., Gaonkar, G.H., "Flapping Response of Lifting Rotor Blades to Atmospheric Turbulence," J. AIAA, Vol. 6, No. 6, 1969.

Holley, W.E., "An atmospheric Turbulence Model for Wind Turbine Dynamic Simulation: Its Verification and Implementation into the FLAP Code," Oregon State University, Unpublished OSU report, 1982.

Husse, G., Einmann, R., "Wind Power Plant WKA-60 for Helgaland - Status of the Project," EWEC, Glasgow, Scotland, July 10-13, 1989.

Husse, G., Perpeintner, R., "The Effect of Variable Rotor Speed on the Design and Operation of a WEC," EWEC, Hamberg, West Germany, Oct. 22-26, 1984.

Johnson, W., Helicopter Theory, Princeton University Press, 1983.

Kaimal, J.C., Wyngaard, J.C., Izumi, Y., Cole, O.R., "Spectral Characteristics of Surface-Layer Turbulence," Quart. J. of the Royal Meteorological Society, Vol. 113, No. 7, 1987.

Kane, T.R., Levinson, D.A., Dynamics: Theory and Applications, McGraw-Hill Book Co, New York, 1985.

Kottapalli, S.B.R., Friedman, P.P., "Coupled Rotor/Tower Aeroelastic Analysis of HAWT Blades," AIAA J., Vol. 18, No. 9, 1980.

Matsuzaka, T., Tsuchiya, K., Yamada, S., and Kitahara, H., "A Variable Speed Wind Generating System and Its Test Results," EWEC, Glasgow, Scotland, July 10-13, 1989.

McNerny, G., "The Effect of Variable Speed Operation on the Cost Projections for Advanced Wind Turbines," Ninth ASME Wind Energy Symposium, New Orleans, Louisiana, January 14-18, 1990.

Miller, R.H., "Methods for Rotor Aerodynamic and Dynamic Analysis," Prog. Aero. Sci., Vol. 22, 1985.

Morgan, C.A., Garrad, A.D., Hassan, U., "Measured and Predicted Wind Turbine Loading and Fatigue," EWEC, Glasgow, Scotland, July 10-13, 1989.

Musial, W.D., Butterfield, C.P., Handman, D., "ESI-80/EPRI Test Program," EPRI RP1996-14, December 1985.

Nordquist, P., "Investigation of Electrical Power Pulsations from a 2 megaWatt Wind Turbine Generator," EWEC, Glasgow, Scotland, July 10-13, 1989.

Ormiston, R.A., Peters, D.A., "Hingeless Helicopter Rotor Response with Non-Uniform Inflow and Elastic Bending," J. Aircraft, Vol. 9, No. 10, 1972.

Piziali, R.A., "Method for Solution of the Aeroelastic Response Problem for Rotating Wings," J. Sound Vib., Vol. 4, No. 3, 1966.

Powles, S.J.R., Anderson, M.B., "The Effect of Stochastic and Deterministic Loading on Fatigue Damage in Large HAWT," Sir Robert McAlpine & Sons, Ltd., London, U.K., 1984.

Prandtl, L., "Appendix to Scraubenpropellor mit Gerngstein Energieverlust," by Betz, A., Guttinger Nachr, 1919.

Rankine, W.J.M., Transactions, Institute of Naval Architects, Vol. 6, p. 13, 1865.

Rosenbrock, H.H., "Vibration and Stability Problems in Large Wind Turbines Having Hinged Blades," The Electric Research Association, TR C/T 113, 1955.

Schmidt, W.C., Birchenough, A.G., "Evaluating Variable Speed Generating Systems on the DOE/NASA MOD-0A Wind Turbine," Wind Power, San Francisco, California, August 27-30, 1985.

Shinozuka, M., "Simulation of Multi-Variate and Multidimensional Random Processes," J. of the Acoustical Society of America, Vol. 9, No. 1, part 2, 1971.

Sundar, R.M., Sullivan, J.P., "Performance of Wind Turbines in a Turbulent Atmosphere," Proc. of Wind Dynamics, NASA CP 2185, Purdue University, 1981.

Veers, P.S., "Modeling Stochastic Wind Loads on Vertical Axis Wind Turbines," SAND83-1909, Sandia National Lab., Sept, 1984.

Veers, P.S., "Three-Dimensional Wind Simulation," SAND88-0152, Sandia National Lab., March, 1988.

Walker, S.N., Weber, T.L., Wilson, R.E., "A Comparison of Wind Turbulence Simulation Models for Stochastic Loads Analysis for HAWT," SERI/STR-217-3463, June 1989.

Weber, T.L., "Inclusion of Nonlinear Aerodynamics in the FLAP Code," Ninth ASME Wind Energy Symposium, New Orleans, Louisiana, January 14-18, 1990.

Weber, T.L., Walker, S.N., Wilson, R.E., "User's Manual for the DRT Rotor Code," Oregon State University, SERI XG-0-19165-1, 1991.

Weyh, B., Ackva, J., "Parameter-Excited Instabilities of 1- and 2-Bladed HAWTS," EWEC, Glasgow, Scotland, July 10-13, 1989.

Wilson, R.E., Hartin, J.R., "Mode Shapes for Wind Turbine Vibration Analysis," ASME J. Solar Engr., May, 1990.

Wilson, R.E., Walker, S.N., Weber, T.L., Hartin, J.R., "A Comparison of Mean Loads and Performance Predictions with Experimental Measurements for Horizontal Axis Wind Turbines," Eighth ASME Wind Energy Symposium, Houston, Texas, Jan. 22-29, 1989.

Wilson, R.E., Walker, S.N., "Performance Analysis of HAWTS," Oregon State University, Corvallis, Oregon, September 1984.

Winkelaar, D., "Fast Three-Dimensional Wind Simulation and the Prediction of Stochastic Blade Loads," Tenth ASME WES, Houston, TX, Jan. 20-23, 1991.

Wright, A.D., Buhl, M.L., Thresher, R.W., "FLAP Code Development and Validation," SERI/TR-217-3125, January 1988.

Wright, A.D., Weber, T.L., Thresher, R.W., Butterfield, C.P., "Prediction of Stochastic Blade for Three-Bladed, Rigid-Hub Rotors," Ninth ASME Wind Energy Symposium, New Orleans, Louisiana, January 14-18, 1990.

APPENDIX

Appendix A

ESI-80

The ESI-80 was a commercially available 300 kW horizontal axis wind turbine, built by the now defunct Energy Sciences, Incorporated. Figure A.1 show a diagram of the ESI-80.

The rotor has two wood-epoxy blades with a diameter of 24.38 meters. The 300 kW induction generator was driven by the rotor at 60 rpm through a gearbox with a step-up ratio of 30. The ESI-80 has a teetered rotor with a undersling length of approximately .25 meters. Hydraulic dampers dampen the teeter motion after two degrees of free travel. Teeter stops (stiff springs) stop the teeter motion at seven degrees. The blades have a precone angle of 7 degrees and the blades are at a fixed pitch. Table A.1 shows blade properties; twist, chord, thickness, weight, and stiffness as a function of percent radius. The ESI-80 has a NASA LS(1)-04XX series airfoil. Wind tunnel lift and drag characteristics used in this study were obtained from three sources [1-3]. The rotor has electro-magnetically released airbrakes located on the tips of the blades for turbine over speed protection. A mechanical caliper brake is used to stop the rotor. The turbine is supported by an 24.4 meter open truss tower. The turbine operates downwind with a free yaw system. Table A.2 lists important turbine characteristics.

The data used for comparison in this study was obtained

from a combined Electrical Power Research Institute and Energy Sciences, Inc. test program [4]. All data used for comparisons were digitized from this report. The test turbine was located at Altamont Pass near Tracy, California. Reported loads include; blade bending moment, rotor thrust, rotor torque, teeter characteristics, and electrical performance. Both mean and cyclic loads were recorded.

A.1 References

1. Satron, D., Snyder, M.H., "Two-Dimensional Tests of GA(W)-1 and GA(W)-2 Airfoils at Angles of Attack from 0 to 360 Degrees," Wichita State University, January, 1979.

2. McGhee, R.J., Beasly, W.D., "Effects of Thickness on the Aerodynamic Characteristics of an Initial Low-Speed Family of Airfoils for General Aviation Applications," NASA TM X-72843, January, 1979.

3. Miley, S.J., "A Catalog of Low Reynolds Number Airfoil Data for Wind Turbine Applications," RFP-3387, Texas A & M University, Feb., 1982.

4. Butterfield, C.P., Musial, W.D., "ESI-80/EPRI Test Program," 6591 Sierra Lane, Suite A, Dublin, California, December, 1985.

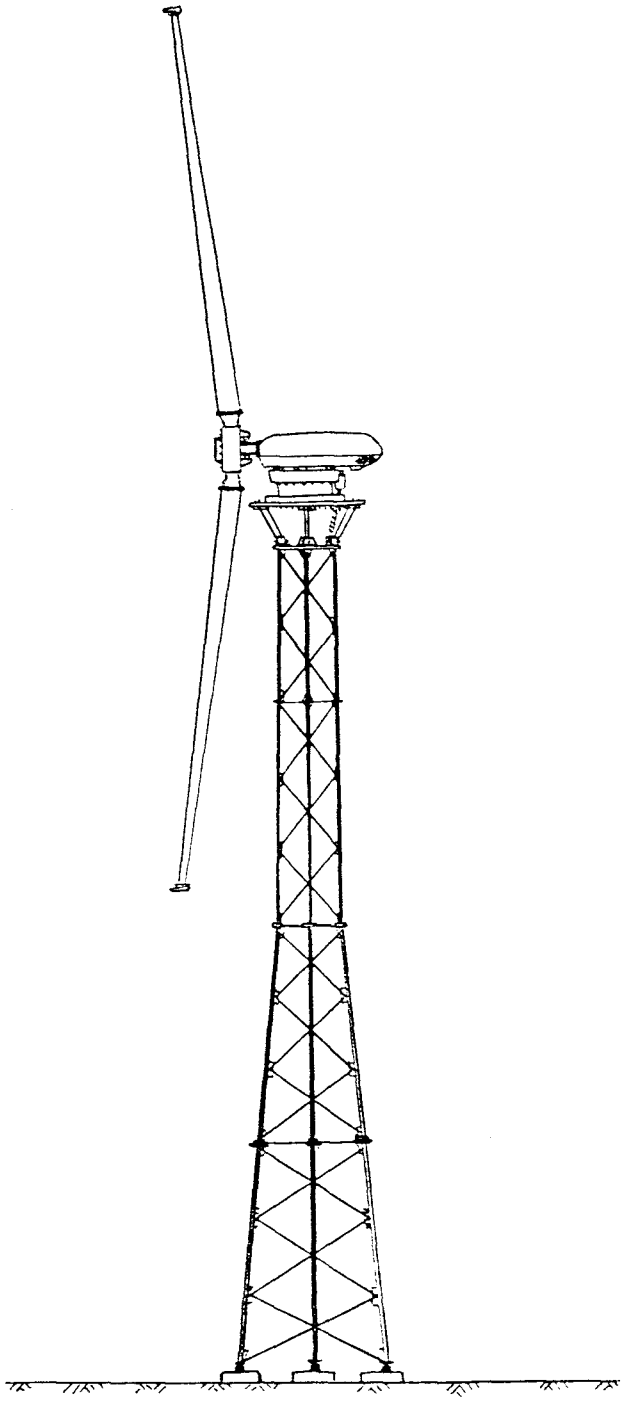

Figure A.1 ESI-80

Table A.1 Blade Properties

Percent Radius	Chord (m)	Thickness (% chord)	Twist (degrees)	Weight (kg/m)	Stiffness (N/m)
.075	.635	.5	2.0	63.3	13316800
.1875	.762	.4125	1.845	55.8	10767500
.3	.8891	.325	1.69	44.9	6818700
.375	.8372	.318	1.503	39.7	4735500
.5	.751	.2875	1.19	29.6	1406300
.625	.6648	.2638	.557	19.6	861000
.75	.5787	.237	-.076	14.0	660100
.875	.4925	.2033	-.905	10.6	344400
1.00	.4063	.17	-2.0	8.95	287000

Table A.2 Turbine Characteristics

Number of Blades	-	2
Rotor Radius	-	12.192 m
Hub Height	-	24.4 m
Hub Radius	-	.92 m
Rotor Speed	-	60 rpm
Teeter Stop	-	7 degrees
Teeter Dampers	-	2 degrees
Precone	-	7 degrees
Tip Mass	-	19.1 kg
Tower Width	-	.7 m
Delta-3	-	0 degrees
Rotor Tilt	-	0 degrees
Undersling	-	0.25 m
Elastic Axis	-	0 degrees
Hub Mass	-	700 kg
Gearbox Efficiency	-	.985
Generator Efficiency	-	.94
Generator Inertia	-	4.89 kg/m^2